Additive Manufacturing of Graded and Anisotropic Materials for Applications at Microwave Frequencies



Yingwei Wu

St Cross College

Michaelmas Term 2020

Supervisor: Prof Patrick S. Grant

A thesis submitted for the degree of Doctor of Philosophy at the University of Oxford

Abstract

Transformation optics (TO) allows the design of new optical devices for the novel manipulation of electromagnetic (EM) waves based on the spatial variation of relative permittivity and permeability, including at microwave frequencies. However, the practical manufacturing methods to realize these designs are limited. This thesis focuses on the investigation of additive manufacturing (AM) to the manufacture of devices that operate at microwave frequencies and involve spatial variations of dielectric permittivity within the device.

Devices were manufactured using fused filament fabrication (FFF) and required the development of a bespoke relatively high dielectric permittivity filament that comprised barium titanate ($BaTiO_3$) particulates dispersed in acrylonitrile butadiene styrene (ABS). The filament was optimized for printing by additions of a surfactant and a plasticiser to maximise the $BaTiO_3$ fraction while maintaining flexibility and consistency to ensure long hours of uninterrupted printing. The optimized filament contained 32 vol% $BaTiO_3$, 1 wt% surfactant and 5 wt% plasticiser, and had a relative dielectric permittivity of ~ 11.

Demonstrator microwave devices were printed using the optimized filament and other commercial polymeric filaments typically with relative dielectric permittivity ~ 3. The device designs involved spatial variations in the local, place-to-place dielectric

permittivity that was achieved by mixing filament types during printing on a sub-wavelength scale. A quarter wave plate (QWP) was printed containing alternating stripes of $BaTiO_3$/ABS and ABS, which successfully converted a linearly polarized wave into a circularly polarized wave at frequencies of 12 to 18 GHz. Three different spiral phase plates (SPPs) were also fabricated that were designed using numerical simulations. Each SPP was designed to provide the same transformation of an incident microwave at 15 GHz, but achieved through different spatial variations of permittivity. The printed SPPs successfully converted a plane wave into a helical wave carrying orbital angular momentum, and the advantages of certain design features were revealed. Multiplexing and demultiplexing were also successfully demonstrated experimentally using both two opposite mode and two same mode SPPs.

Lastly, to further explore the flexibility and degrees of freedom provided by AM of devices working at microwave frequencies, active device tuning was realized by printing of dielectric origami structures. Tuning was achieved through mechanical actuation and transformation of the dielectric element configurations. A suspended patch antenna with a resonant frequency of 1 GHz showed a maximum frequency shift of 0.45 GHz on actuation. Numerical simulations were performed consistent with experiments and suggested further potential for antenna tuning. The device demonstrations showed the potential of AM for realising spatially varying dielectric properties and the prospect for compact and broadband microwave devices.

Acknowledgements

Firstly, I would like to express my sincerest gratitude to my supervisor Prof. Patrick S. Grant for his patience, guidance, and support throughout my study. It has been quite a tough and rewarding journey since the DPhil program started. Thanks to Prof. Grant, who has given me the freedom to explore research directions and supported me to go to conferences and attend workshops, I had the opportunity to learn and grow. I am deeply grateful to his generous help throughout my DPhil.

I would also like to thank Prof. Dmitry Isakov for his invaluable guidance and help. It has been a pleasure to work with him and I have learnt so much from him. I would like to thank Dr. Ben Allen for helping me to understand the applications of microwave devices. I would like to thank Dr. Andrea Vallecchi for insightful discussions and his aid in antenna fabrication.

I acknowledge China Oxford Scholarship Fund (COSF) and Kennametal for financial support during my study. Many thanks also goes to Dr. Enzo Loitti, Dr. Lukas Fieber, Dr. Junfu Bu, Dr. Ann Huang, Dr. Yige Sun, Dr. Shikang Feng, Dr. Jack Evans, Ms. Zhouran Zhang, thank you for all the fruitful discussions and help. I would also like to thank Ms. Julie Young and other colleagues in the office for making the Processing of Advanced Materials Research Group a big family. Many thanks to Mr. Robin Vincent for his help on machining of samples, Dr. Andrew Liu

for his help with X-ray tomography, and Dr. Colin Johnson and the OMCS Group for training and access to various characterization equipment.

I would also like to thank Dr. Yunke Wang, Ms. Morine Liang, and my friends at Oxford, who have showed me another side of life apart from research. Thank you for your company and making my life here happy and wonderful.

Lastly, my deepest gratitude goes to my parents and my brother, who have supported me all the time, and never put extra pressure on me. Their unconditional love gives me the freedom to pursue my study without burden.

Contents

1 Introduction **17**

2 Literature Review **27**

2.1 Transformation Optics (TO) Inspired Materials 27

2.1.1 Transformation optics theory and key parameters 28

2.1.2 Graded and anisotropic composite materials 31

2.1.3 Characterization techniques 36

2.1.4 Summary 40

2.2 Manufacturing Methods 41

2.2.1 Conventional methods 42

2.2.2 Additive manufacturing 47

2.2.3 Summary 65

3 Filament Optimization **79**

3.1 Introduction 80

3.2 Methods 82

3.3 Results and Discussion 85

3.3.1 Effect of surfactant 85

3.3.2 Effect of plasticiser 90
3.3.3 Demonstration 96
3.4 Conclusions 98

4 Printed Device Demonstration - Quarter Wave Plate 104
4.1 Introduction 105
4.2 Methods 107
4.3 Results and Discussion 111
4.3.1 Polarization analysis 111
4.4 Conclusions 115

5 Printed Device Demonstration - Spiral Phase Plate 119
5.1 Introduction 120
5.2 Methods 122
5.3 Results and Discussion 125
5.3.1 Spiral phase plate design and fabrication 125
5.3.2 Phase and amplitude analysis 127
5.3.3 Reducing OAM beam divergence 130
5.3.4 Multiplexing and de-multiplexing with spiral phase plates . . . 131
5.4 Conclusions 133

6 Active Device Tuning with Origami Structures 138
6.1 Introduction 139
6.2 Methods 141
6.3 Results and Discussion 147
6.3.1 Materials characterization 147

6.3.2 $BaTiO_3$/ABS dielectric origami 148
6.3.3 $CaTiO_3$/ABS dielectric origami 150
6.4 Conclusions 152

7 Conclusions **157**

8 Future Work **159**

List of Figures

1.1 (a) A EM wave (in red) travelling free space through a Cartesian coordinate grid, and (b) distorted coordinate system due to a local change in EM properties leading to a curved wave path [4]. 19

1.2 (a) A two dimensional cross-section of ray trajectories in the cloak region with R1 < r < R2, with R2 >> λ; the rays arrive from the left and will appear on the far side undeviated from the original source, and (b) a 3D view of the same arrangement [4]. 20

2.1 Loss tangent vector diagram. 30

2.2 Different characterization techniques with their working frequencies and loss [38]. 37

2.3 Schematic diagram of single screw extruder [46]. 44

2.4 Schematic of the fused filament fabrication (FFF) additive manufacturing [69]. 50

2.5 (a) A graded-index lens produced by FFF with PLA for transforming spherical waves emanating from the focal point into plane waves. The lens comprised of 6 × 10mm wide discrete dielectric concentric rings with lowest permittivity of 1.3 in the outmost ring to highest permittivity of 2.72 in the center ring [87], and (b) a polycarbonate-ABS lattice produced by FFF with fill fraction of 30%. The lattice composed of 22 × 22 × 22 cubic unit cells with same lattice spacing, but the orientation of the unit cell being spatially varied and the radius of the curve varying by more than × 20 across the device to allow beam bending of 90°[16]. 55

2.6 (a) A gradient refractive index flat lens made by FFF of BTO/ABS and ABS. The top two images show the variation in BTO/ABS filament fraction with position in the lens, from highest fraction in the middle to low fraction on the sides, giving highest permittivity in the middle, gradually reducing to low permittivity at the edges. The lower graph shows the experimental measurements of the spatial distribution of relative permittivity across the lens obtained using a SPDR technique along with a comparison of the measured (solid line) and the ideal theoretical (dotted line) radial variation in local permittivity [17], and (b) PZT/epoxy composite used for making a transducer by FFF. The composite comprised of alternating parallel plates of ceramic (in grey) and polymer (in white). The width of the ceramic plate was dictated by the nozzle diameter and spacing between the parallel plates was determined by the desired volume fraction of the ceramics [88]. 57

2.7 Schematic of polyjet printing process [90]. 59

2.8 (a) A Luneburg lens made by polyjet. The lens (length of 24 cm) was comprised of different sized polymer cubes (5 mm) to manipulate the local dielectric permittivity distribution. Thin rods were used to connect all the cubes and support the whole structure [91], and (b) a metallized patch antenna made by polyjet. The dielectric substrate was sandwiched between a metallized ground plane at the bottom and a metallized radiating patch on top. A coaxial cable was attached from the back side and the center conductor was affixed to the top metal layer using Ag epoxy [92]. 61

2.9 Schematic of stereolithography (SLA) printing process [77]. 62

2.10 (a) A waveguide fabricated by SLA and then Cu-plated, assembled from two split blocks [77], with total length of 60 mm, and (b) a horn antenna fabricated by SLA and then metallized with conductive Ag ink. The dimensions are $40.2 \times 29.3 \times 51$ mm [94]. 64

3.1 Stages of filament fabrication process: (a) $BaTiO_3$ powder, ABS pellets and acetone; (b) mixing and stirring on a stir plate to form a solution; (c) drying of the solution on a tray covered with aluminium foil; (d) single screw extrusion to fabricate the composite filament, and (e) the extruded filament on a spool. 83

3.2 In-house built bending test rig. The filament was clamped into two holders with the left one stationary and the right one moving towards the left at constant velocity. 85

3.3 Electron micrographs of the cross-section of 30 vol% $BaTiO_3$/ABS filaments (column 1 and 2) and 3D-printed samples using the corresponding filament (right column) (a-c) $BaTiO_3$/ABS with 0 wt% surfactant; (d-f) 0.5 wt% surfactant; (g-i) 1.0 wt% surfactant; and (j-l) 1.5 wt% surfactant. 89

3.4 Electron micrographs of the cross-section of fabricated filaments (a-b) Sample 5, and (c-d) Sample 6, with 5 and 10 wt% dibutyl phthalate plasticizer respectively. 91

3.5 Optical images of the surface of the $BaTiO_3$/ABS composite filaments (a) Filament 1 (roughness $Ra = 4.26$ μm); (b) Filament 2 ($Ra = 1.49$ μm); (c) Filament 3 ($Ra = 0.72$ μm); (d) Filament 4 ($Ra = 4.01$ μm), and (e) Filament 5 ($Ra = 0.57$ μm). 92

3.6 Differential scanning calorimetry measurements of heating (red curves) and cooling (blue curves) for ABS filament, Sample 3 (1 wt% surfactant), Sample 5 (1 wt% surfactant, 5 wt% plasticizer) and Sample 6 (1 wt% surfactant, 10 wt% plasticizer). 93

3.7 Typical bend test behavior of ABS only and $BaTiO_3$/ABS composite filaments. The composite filament composed of 32 vol% $BaTiO_3$/ABS with 1 wt% surfactant and 5 wt% plasticiser (filament 5) showed the same flexibility as ABS only (shown as the dotted line). 95

3.8 Measured real part of the relative dielectric permittivity as a function of frequency for 3D-printed coupons from filament 5 (solid red) and 3 (dashed black). 96

3.9 X-ray tomography image of the 3D-printed $15 \times 15 \times 15$ mm^3 cube using optimized composite filament 5 (a) Full 3D reconstruction; (b) typical xy-plane slice, and (c) typical xz-plane slice. The images show no resolvable voids or interlayer porosity. 97

3.10 Demonstration examples of several 3D-printed microwave devices for generation of orbital angular momentum. 98

4.1 Schematic diagram of three types of polarization by resolving the electric field (E) into two orthogonal components Ex and Ey (a) example of a linearly polarized wave when the phase difference is 180°; (b) example of a circularly polarized wave with phase difference of 90 °, and (c) example of an elliptically polarized wave when the phase difference is 90°and the amplitude of Ex and Ey is different. 106

4.2 The design approach for a microwave QWP. (a) The effective relative dielectric permittivity of the upper ($\epsilon_{\max}$,) and lower ($\epsilon_{\min}$) Wiener bounds as a function of volume fraction f of a two-phase composite with ϵ_{l}=2.65 and ϵ_{h}=10.8 corresponding to ABS and $BaTiO_3$/ABS filaments; (b) the difference between the upper and lower Wiener bounds $\Delta\epsilon = \epsilon_{\max} - \epsilon_{\min}$ and the corresponding derivative $\Delta\epsilon(f)$ that determines the optimum volume fraction f_0, shown as a dashed vertical line, and (c) CAD model of the QWP composed of two materials and designed with regards to the conditions shown in (b) and Equation 4.4.109

4.3 Printed QWP with alternating stripes of ABS (white) and $BaTiO_3$/ABS (yellow) attached to a 3D printed pyramidal microwave horn. 110

4.4 Schematic diagram showing how a linearly polarized wave with a linear E field enters the QWP placed at a 45° rotation, resulting in a circularly polarized wave with E field transformed into Ex and Ey components of equal amplitude. 111

4.5 (a) Simulated near-field x and y components of the electric field E in the direction of radiation for pyramidal horn with E oriented along y-axis and QWP with its "slow" axis also parallel to y; (b) The same components after the rotation of the QWP at 45° to the polarization of the horn antenna; (c) Projection of the far-field $E_y - E_x$ difference on a plane 0.8×0.8 m^2 at a distance of 100λ from the horn aperture with the QWP oriented with its "slow" axis parallel to the radiation polarisation E_y, and (d) oriented at 45°. Note that the intensity contours in the colour legend have different scales. 112

4.6 (a) Schematic of the experimental setup showing two pyramidal horns and the QWP; (b) Measured power gain difference and phase difference; (c) between transmitted E_y (P$\|$A) and E_x (P$\perp$A) components with QWP oriented at 45° to the principal axes, and (d) Measured transmittance (T) (solid black curve) as a function of the QWP rotation (θ) between two ports oriented perpendicularly to each other (P$\perp$A). 113

5.1 Photo of the 90 mm diameter, 10 mm thick (maximum) 3D printed dielectric lens. 123

5.2 (a) Schematic of the experimental set-up for the characterization of phase and amplitude for SPPs, and (b) schematic of the experimental set-up for multiplexing and demultiplexing. 124
5.3 Photographs of the 3D-printed SPPs from left to right: SPP with staircase structure, flat SPP with gradient refractive index and a SPP of varying thickness. 126
5.4 (a)The CAD models, and (b) a photograph of the mode $l = +2$ 3D-printed dielectric spiral phase plate. 126
5.5 X-ray tomographs of the 3D-printed dielectric spiral phase plates (a) SPP with a stairwise structure, and (b) flat SPP with gradient refractive index. 127
5.6 Experimental measurements from the printed SPPs with mode $l = 1$ in the xy-plane over an area of 700×700 mm^2 perpendicular to the wave propagation direction at 15 GHz: (a-b) staircase SPP phase profile and amplitude profile; (c-d) flat SPP phase profile and amplitude profile, and (e-f) varying thickness SPP phase profile and amplitude profile. 129
5.7 Experimental measurements from the printed staircase SPP design with mode $l = 2$, in the xy-plane cover an area of 700×700 mm^2 perpendicular to the wave propagation direction at 15 GHz: (a) phase profile, and (b) amplitude profile. 130

5.8 Experimental measurements from the printed SPPs with mode $l = 1$ in the xy-plane over an area of 700×700 mm^2 perpendicular to the wave propagation direction at 15 GHz with a printed lens at the transmission horn for collimation: (a-b) staircase SPP phase profile and amplitude profile; (c-d) flat SPP phase profile and amplitude profile, and (e-f) varying thickness SPP phase profile and amplitude profile. 131

5.9 Experimental measurements of phase and amplitude profiles from the printed SPPs in the xy-plane over an area of 700×700 mm^2 perpendicular to the wave propagation direction in the frequency range 12 o 18 GHz (a) de-multiplexing with mode $l = 0$, and (b) multiplexing with mode $l = 2$ 133

6.1 (a) The transformation of an origami unit cell from configuration 1 to 2 and 3, with arrows showing the direction of the applied force along y axis; (b) printed $BaTiO_3$/ABS DO in the fully compressed state, and (c) in the expanded state. 142

6.2 (a) CAD design of the SLA printed flexible lattice for DO with a groove on the left an right sides for fixation; (b) higher magnification view of the unit cells of triangle structures within the flexible lattice, and (c) a photograph of the printed flexible lattice. 143

6.3 (a) Disc of $CaTiO_3$/ABS composite (diameter of 80 mm) produced by the field assisted sintering technique, and (b) triangular dielectric elements of short side length 8 mm obtained by waterjet cutting. . . 144

6.4 The ABS-60 vol% $CaTiO_3$ DO (a) fully compressed, and (b) expanded by hand. 144
6.5 (a) Schematic and (b) cross-sectional view of the suspended patch antenna with an 8 mm air gap between the ground plane and the patch, into which the DO may be placed. 145
6.6 Resonant frequency of a suspended patch in Figure 6.5 when a dielectric layer of variable permittivity and thickness of 7 mm is inserted into the air gap, as calculated by Dr. Vallecchi using the approach described in [24]. 146
6.7 Mechanical actuation arrangement for the DO. Printed Onyx fixtures are shown in black. 147
6.8 SEM images of (a) 32 vol% $BaTiO_3$ dispersed within ABS in filament form for FFF, and (b) 60 vol% $CaTiO_3$ dispersed within ABS in circular coupon form after production using FAST. 148
6.9 Modulus of the reflection coefficient S_{11} from a suspended patch antenna resonating at 1 GHz and with two configurations of DO placed below the antenna over a Cu ground plane. Dotted lines represent simulations and solid lines experiment. 149
6.10 Measured resonant frequency of a patch antenna against the extension distance (opening) of the ABS-60vol% $CaTiO_3$ DO (blue circles) and the corresponding estimated effective permittivity of the DO (red diamonds) from simulation in Figure 6.6. 151

Chapter 1

Introduction

This thesis investigates additive manufacturing (AM), also known as 3D printing (3DP), as a means to manufacture optical devices that operate at microwave frequencies for the manipulation of electromagnetic (EM) wave propagation. Microwave frequency applications are found in wireless communication systems such as resonators, filters, and antennas [1]. A key aspect of the research is the desire to have convenient materials and manufacturing methods to implement transformation optics (TO) theory in the design of microwave devices, which requires gradient and/or anisotropic EM properties of the component materials. The ability to change the path of an EM wave may enable applications such as cloaking devices, field concentrators, polarization rotators, beam splitters, beam collimators and flat lenses [2][3]. However, the challenge associated with the realization of TO based designs comes from the difficulty in achieving the required wide range or extreme values of permittivity and permeability (and thus refractive index) in practice, and the associated manufacturing processes. In particular, this thesis investigates how to achieve a spa-

tial variation of permittivity by developing appropriate materials and manufacturing processes.

TO is a mathematical tool that is used to design the properties of artificial materials to achieve the manipulation of the emission, propagation and absorption of EM waves, under the form-invariant property of Maxwell equations by using a coordinate transformation [4][5]. When an EM wave travels in a Cartesian coordinate system, it travels between two points along the path that requires the least time according to Fermat's principle [6], and the path length is determined by the refractive index n of the media. This principle results in a straight line path in a uniform grid, as shown in Figure 1.1(a). In Figure 1.1(b), if the coordinates are composed of materials with different refractive indexes, the coordinates appear distorted to the propagating wave. Consequently, the wave will travel in the same distorted manner, and the shortest optical path will now be curved. Many optical phenomena, such as refraction of a straw at the interface of air and water, and the mirage effect in a desert due to air density (refractive index) variation, can be explained by this principle.

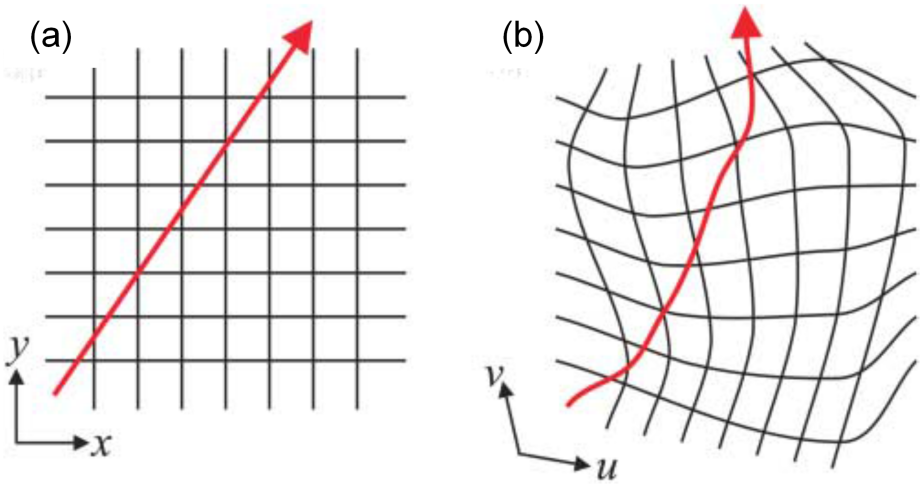


Figure 1.1: (a) A EM wave (in red) travelling free space through a Cartesian coordinate grid, and (b) distorted coordinate system due to a local change in EM properties leading to a curved wave path [4].

The refractive index n is related to permittivity ε_{r} and permeability μ_{r} by :

$$n^2 = \varepsilon_{\mathrm{r}}\mu_{\mathrm{r}} \tag{1.1}$$

The ability to tailor local permittivity and permeability and the refractive index may enable the realization of various optical effects and devices. The most well-known but difficult example is the so-called invisibility cloak, an example of which is shown in Figure 1.2 [4]. An arbitrary object is placed in space such that when EM waves are incident on the object, EM waves are guided around the object and return to their original trajectory. From the observer's point of view (which has to be at an exact position), the object appears to be concealed or invisible.

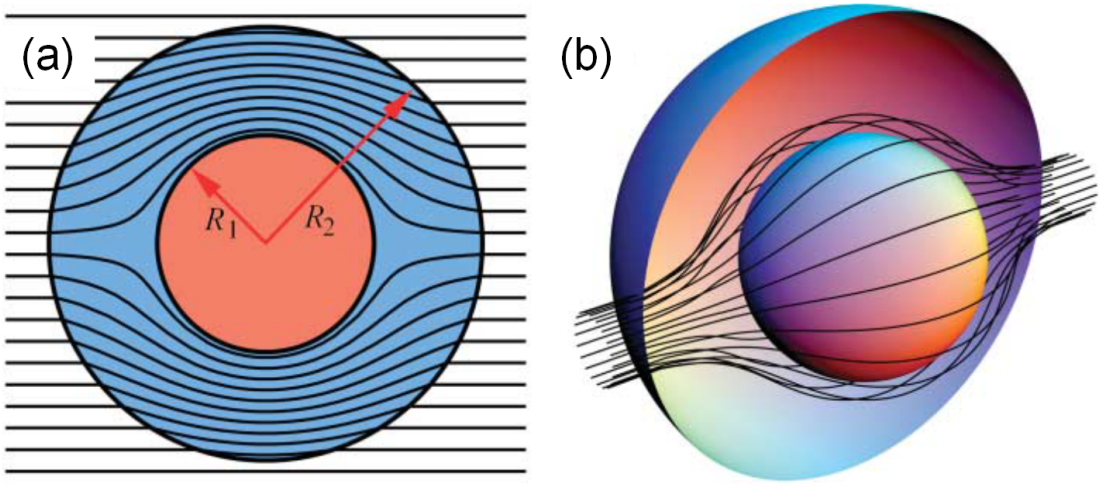


Figure 1.2: (a) A two dimensional cross-section of ray trajectories in the cloak region with R1 < r < R2, with R2 >> λ; the rays arrive from the left and will appear on the far side undeviated from the original source, and (b) a 3D view of the same arrangement [4].

The physical realization of TO inspired designs faces two challenges. The **first** challenge relates to the materials. For the theoretical designs to function, the materials need to have a refractive index that can vary from point to point, which requires the materials to have a spatially varying permittivity and/or permeability, which is generally unachievable in a single material system. The **second** challenge lies in manufacturing, since the spatial or geometric patterns required by the TO design are difficult to achieve using current manufacturing processes.

A common way to change the permittivity and/or permeability of materials is to embed metallic resonant structures usually in repeating patterns or arrays of sub-wavelength spacing, to form a so-called meta-material. Meta-materials are a class of artificial material that exhibit anomalous EM properties and cannot be found in nature [7]. Their engineered sub-wavelength structure is designed to exhibit strong resonance coupling with the electric and magnetic components of an incident EM

wave, typically constituted by a regular spatial arrangement of inclusions within a host material. Composition, alignment (periodicity), density and geometry of the inclusion as well as the constitutive parameters of the host material determine the macroscopic response of the meta-material [8][9]. Metals or simple metallic patterns or shapes are commonly used to act as the inclusions. However, due to their strong dissipation, loss of energy, narrow bandwidth, and difficulties in implementation, the application of meta-materials into practical engineering structures has been relatively limited, although some startling effects have been realized in the laboratory, such as negative refractive index [7].

An alternative approach to affect changes in EM properties is to use an all dielectric material, which offers wider bandwidth, less loss and more flexibility for practical implementation, although with less dramatic effects on EM wave propagation. The focus of this thesis is to investigate the design of materials for all-dielectric meta-materials and corresponding manufacture methods for simple demonstrator devices that operate at microwave frequencies.

Composite materials [10], which are controllably heterogeneous and anisotropic, are chosen as the main focus to affect permittivity variations. AM is chosen as a robust, cost effective and flexible manufacturing method to realize the complex 2D or 3D permittivity patterns in a layer-by-layer fashion [11]. Compared with conventional manufacturing processes for bulk composites, such as extrusion, casting, etc [12], AM opens up the possibility to process multiple materials or functionally graded materials [13] into a final 3D shape in a single operation. AM of particulate composites (rather than the more common long fiber reinforced composites used widely in structural applications) is relatively immature, but a fast moving field. With suitable AM capability and appropriate materials choices, it may be possible

to verify novel designs based on TO in which microwave propagation is controlled from point to point, with resolution, in the mm to cm range.

The thesis explores the manufacture of composite materials with graded and anisotropic properties by AM for applications in microwave frequencies (100 MHz to 20 GHz), and to tailor EM wave propagation from point to point, at the mm-scale. Polymer/ceramic composites are chosen for the AM fused filament fabrication (FFF) method. Polymer/ceramic composites have the advantages of low cost and simple manufacturing processes. The majority polymer matrix choice is based on the compatibility of the polymer to the AM process as well as its intrinsic dielectric properties. Ideally, the polymer should be extrudable (printable) at a temperature below 250°C due to the heating limitation of non-specialist 3D printers. The polymer should also exhibit a glass transition temperature and be softened by elevated temperature sufficiently to be extruded through a small nozzle (diameter typically 0.4 to 1.5 mm). High dielectric permittivity composite particles (or fillers) are embedded in the polymeric matrix to give some control over dielectric properties. By varying the type of filler, its particle size, and its volume fraction, a range of permittivities are available in principle. In this work, and in the wider literature, ferroelectric ceramic barium titanate $BaTiO_3$, abbreviated as BTO, is often chosen as the ceramic filler due to a high intrinsic dielectric permittivity (several thousand), depending on the grain size and temperature [14], widespread availability and detailed literature. Factors that affect the dielectric properties of BTO include exact composition, particle size, morphology and frequency [15].

The composite filament used here is optimized for the highest dielectric permittivity while retaining mechanical robustness and flexibility to sustain many hours of reliable printing. Further, with two or more types of filament and a multi-head FFF

printer, and by changing the local ratio of the high dielectric permittivity composite filament to the low dielectric permittivity polymer filament, changes in the local permittivity across a range bounded by the upper and lower permittivities can be realised.

Numerical simulations e.g. COMSOL Multiphysics RF Module and CST Microwave Studio, are used to guide the design of the optical devices based on the properties of available filaments and the constraint of current AM capability. Without a guiding predictive capability, the design space for AM dielectric devices is too large for trial and error experimentation. Simulations are essential to predict microwave propagation in devices, which can be compared with experimental data; without simulated propagation, complex microwave reflection and transmission experimental data cannot be easily interpreted.

A rapidly emerging sub-theme within meta-materials is that of a tunable material whose resonant or other response to EM propagation can be adjusted at will by external stimulation, such as temperature or mechanical force. AM approaches may offer new routes towards tunable meta-material and devices, and they may add a further degree of freedom in the quest to control EM wave propagation.

In summary, the thesis comprises three themes. The first is the study of the properties of composite filaments suitable for the FFF version of AM, ensuring desired dielectric properties with reliable printing as the foundation for AM of microwave devices. The second theme is the design, simulation and printing of simple optical devices based on the practical materials and AM capability available. The final theme is to explore active or tunable material implementations.

The principle scientific and engineering contributions are:

1. The development of a FFF filament of permittivity of around 11. Although high

dielectric permittivity filaments had been achieved previously, they tended to be unreliable. The use of surfactants and plasticizers increased the dispersion of fibers and mechanical properties to enable a robust filament for many hours of printing.

2. The demonstration of printed quarter wave plate (QWP) with dual filaments: acrylonitrile butadiene styrene (ABS) and $BaTiO_3$/ABS composite. The printed QWP was capable of converting polarization of EM wave, and exhibited broadband features.

3. The demonstration of different designs of printed spiral phase plates (SPPs) with mode 1 and 2. Those printed phase plates were capable of generating waves carrying orbital angular momentum (OAM), which can be potentially applied in communication systems to increase the band efficiency.

4. The demonstration of tuning of a suspended patch antenna using printed dielectric origami structures, with a tuning range of up to 10%. Tuning was achieved through mechanical actuation to cause changes in local permittivity.

Bibliography

[1] Y. H. Jung, J. Lee, Y. Qiu, N. Cho, S. J. Cho, H. Zhang, S. Lee, T. J. Kim, S. Gong, and Z. Ma, Stretchable twisted-pair transmission lines for microwave frequency wearable electronics, Advanced Functional Materials, vol. 26, no. 26, pp. 4635–4642, 2016.

[2] D. H. Kwon and D. H. Werner, Transformation electromagnetics: An overview

of the theory and applications, IEEE Antennas and Propagation Magazine, vol. 52, no. 1, pp. 24–46, 2010.

[3] Y. Yang, B. Zhang, E. Li, and H. Chen, Towards omnidirectional, large scale, full polarization, and broadband practical invisibility cloaks: challenges and progress, EPJ Applied Metamaterials, vol.1, p.7, 2014.

[4] J. B. Pendry, Controlling electromagnetic fields, Science, vol.312, no.5781, pp.1780–1782, 2006.

[5] J. B. Pendry, A. Aubry, D. R. Smith, and S. A. Maier, Transformation optics and subwavelength control of light, Science, vol.337, no.6094, pp.549–552, 2012.

[6] M. Born and E. Wolf, Principles of Optics, sixth edition, pp. 1 – 70, 1980.

[7] H. Chen, C. T. Chan, and P. Sheng, Transformation optics and metamaterials, Nature Materials, vol. 9, no. 5, pp. 387–396, 2010.

[8] R. C. Rumpf, J. J. Pazos, J. L. Digaum, and S. M. Kuebler, Spatially variant periodic structures in electromagnetics, Philosophical transactions Series A, Mathematical, physical, and engineering sciences, vol.373, no.2049, pp.20, 2015.

[9] A. Sihvola, Electromagnetic mixing formulas and applications, Electromagnetics and Radar Series, 1999.

[10] D. Gay and S. V. Hoa, Composite materials: design and applications, CRC Press, 2003.

[11] T. Wohlers, W. Associates, R. Campbell, and T. Caffrey, 3D Printing and Additive Manufacturing State of the Industry : Annual Worldwide Progress Report, Wohlers Associates, 2016.

[12] P. S. Grant, F. Castles, Q. Lei, Y. Wang, J. M. Janurudin, D. Isakov, S. Speller, C. Dancer, and C. R. Grovenor, Manufacture of electrical and magnetic graded and anisotropic materials for novel manipulations of microwaves, Philosophical Transactions A, vol.373, no.2049, p.20140353, 2015.

[13] R. M. Mahamood, E. T. A. Member, M. Shukla, and S. Pityana, Functionally Graded Material : An Overview, World Congress on Engineering, vol. III, pp.2–6, 2012.

[14] K. Kinoshita, Grain-size effects on dielectric properties in barium titanate ceramics, Journal of Applied Physics, vol. 47, no.1, p.371, 1976.

[15] M. T. Sebastian and H. Jantunen, Polymer-ceramic composites of 0-3 connectivity for circuits in electronics: A review, International Journal of Applied Ceramic Technology, vol.7, no.4, pp.415–434, 2010.

Chapter 2

Literature Review

2.1 Transformation Optics (TO) Inspired Materials

The theory and key parameters related to the concept of TO are discussed in this section, followed by a discussion of various materials choices with properties (e.g. high dielectric permittivity and anisotropy) required by TO, with a focus on composite materials. Lastly, characterization techniques are reviewed as they are critical to to assess the EM properties of different materials and devices and for comparison with simulation results.

2.1.1 Transformation optics theory and key parameters

TO is a mathematical tool that is used to link a change in local material properties with a change in physical coordinates. Consider light propagation through a small distance Δx in a material with refractive index n. The wave phase change in that distance is given by $(w/c)n\Delta x$, where w is the angular frequency and c is the speed of light. The phase change can be rewritten as $(w/c)\Delta x^{'}$, where $\Delta x^{'} = n\Delta x$. Assume n is a function of position in the coordinate system, then the change in local transformation can occur everywhere. As described in the introduction, this correspondence between n and the coordinate system is used for designing materials for TO inspired applications such as cloaking devices [1] .

TO employs spatial-coordinate transformations operating on Maxwell's equations, where the compression or dilation of space in 2D or 3D coordinate systems are interpreted as appropriate scalings of the material permittivity tensor $\boldsymbol{\varepsilon}$ and permeability tensor $\boldsymbol{\mu}$. It relies on two key observations: 1- The invariance of Maxwell's equations under any coordinate transformation; and 2 - The interpretation of the electric permittivity and magnetic permeability in the transformed coordinate system as a set of transformed materials properties in the original coordinate systems [1–3].

$$\nabla \times H = \varepsilon \frac{\partial E}{\partial t} \tag{2.1}$$

$$\nabla \times E = -\mu \frac{\partial H}{\partial t} \tag{2.2}$$

where $\boldsymbol{E}$ and $\boldsymbol{H}$ are the electric and magnetic field respectively [4–7]. If a

coordinate transformation $x' = x'(x)$ is applied, then the equations maintain the same form in the transformed coordinate system:

$$\nabla \times H' = \varepsilon' \frac{\partial E'}{\partial t} \tag{2.3}$$

$$\nabla \times E' = -\mu' \frac{\partial H'}{\partial t} \tag{2.4}$$

The permittivity tensor $\boldsymbol{\varepsilon'}$ and permeability tensor $\boldsymbol{\mu'}$ in the transformed coordinate system are related to the original $\boldsymbol{\varepsilon}$ and $\boldsymbol{\mu}$ by the Jacobian Transformation matrix between the virtual space and the original space [8].

Thus, permittivity $\boldsymbol{\varepsilon}$ and permeability $\boldsymbol{\mu}$ can be used to control EM wave propagation. In this thesis, non-magnetic materials are only considered and so permeability is fixed as $\mu_r = 1$. The permittivity tensor $\boldsymbol{\varepsilon}$ of an isotropic material can be reduced to scalar ε because the permittivity value is constant within the material and the focus of this thesis is how to select and manufacture materials with suitable permittivity.

Relative permittivity ε_r, also often called the dielectric constant, describes the interaction of material with an electric field, which is determined by the ability of a material to polarize in response to the electric field. ε is the absolute permittivity of the material and ε_0 is the permittivity of vacuum:

$$\varepsilon_{\mathrm{r}} = \frac{\varepsilon}{\varepsilon_0} \tag{2.5}$$

In theory, higher permittivity can lead to device miniaturization, which is of importance in modern electronics applications where space in devices is always highly

constrained. For example, a height reduction of 25% was achieved in a double-layered antenna with a $\varepsilon_{\mathrm{r}} = 80$ material compared with a $\varepsilon_{\mathrm{r}} = 30$ material [9]. In practice, it is challenging to achieve high permittivity (> 100) in microwave devices, partly due to limitation in fabrication processes (which will be discussed in Chapter 3).

Permittivity is a complex quantity comprising real $\varepsilon'_{\mathrm{r}}$ and imaginary $\varepsilon''_{\mathrm{r}}$ parts. The quality factor Q and loss are used as key parameters in the characterization of devices operating at microwave frequencies. The quality factor is inversely proportional to loss. The loss of the material, termed $\tan\delta$ is the ratio of the imaginary part to the real part:

$$\tan\delta = \frac{\varepsilon''_r}{\varepsilon'_r} = \frac{1}{Q} \tag{2.6}$$

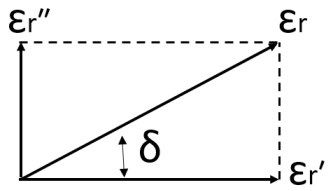


Figure 2.1: Loss tangent vector diagram.

High Q ($Q \times f > 40,000$ GHz) and low loss (< 0.01), together with temperature stability, are key material priorities for retaining maximum signal intensity as well as frequency resolution in high-speed digital electronic devices [6, 10].

2.1.2 Graded and anisotropic composite materials

TO-based designs usually require gradient and/or anisotropic properties of materials that lead to artificial materials at the operating frequency being assembled from sub-materials carefully arranged at the sub-wavelength scale. In order to create local variance in permittivity, it is necessary to spatially vary, or functionally grade, different attributes of the device, such as the lattice spacing in a resonating device, orientation of the unit cells, material composition and fill fraction [11]. Various ways have been used to achieve a change in local permittivity, such as the incorporation of an array of metal rods that resonate to achieve negative permittivity [12], split ring resonators (SRR) to achieve negative permeability [13, 14], the combination of both [15], air holes as a second media to change the density of the bulk material [16–18], and high dielectric constant ceramics to increase the effective permittivity [17].

Composite materials compromise of a filler (typically a ceramic in this field) dispersed within a majority polymer matrix. By integrating ceramics and polymers, polymer based dielectric composites have attracted significant research and development attention as they can offer an attractive compromise in properties, including useful flexibility, low temperature processing, chemical resistance, and tailored dielectric properties [19].

Ceramics are the most important dielectric materials, offering intrinsic high dielectric constants (> 1000) and excellent thermal stability, but suffer from brittleness, high density and difficult fabrication requirements (such as sintering temperatures > 1200 °C for BTO [20]). Table 2.1 shows some of the commonly used ceramic dielectrics and their permittivities. Amongst the high dielectric constant ceramics,

BTO is one of the most widely studied.

Table 2.1: Dielectric ceramics and their relative permittivities at room temperature at 4 GHz [21].

Material	Relative permittivity
Al_2O_3	9.5
$MgTiO_3$	16
$BaTi_4O_9$	38
$BaZrO_3$	40
TiO_2	90
$CaTiO_3$	150
$SrTiO_3$	200
$BaTiO_3$	1500

Polymers have the advantage of mechanical flexibility, low processing temperature, relatively low cost, but suffer from low intrinsic dielectric constant (< 10). Some of the commonly used polymers for dielectric composites are listed in Table 2.2 [22]. Amongst those, ABS is one of the most widely used for 3D printing because it is low cost, safe and flexible and can be be dissolved readily in most solvents.

Table 2.2: Commonly used polymers and their dielectric constants at room temperature [23].

Material	Dielectric constant
PTFE [Poly(tetrafluoroethylene)]	2.1 @11 GHz
PP (Polypropylene)	2.2 @1 GHz
PE (Polyethylene)	2.25 @ 10 GHz
PS (Polystyrene)	2.54 @ 10 GHz
ABS (Acrylonitrile-butadiene-styrene)	2.6 @ 10 GHz
PC (Polycarbonate)	2.89 @ 1 GHz
PVDF (Polyvinylidene fluoride)	8.4 @ 1 KHz

High permittivity > 1000 ceramics are divided into two groups. The first group are intrinsic, spontaneous ionic polarization ferroelectric materials such as $PbTiO_3$ and BTO [24], with high permittivity arising from polar symmetry in their crystallography structure. The other principal class are those that can show extrinsic polarization in the boundary region between grains or inside grains, such as $CaCu_3Ti_4O_{12}$ [25].

A limitation of the ceramic filler approach is that while effective permittivity increases with increasing ceramics particle fraction, the useful composite mechanical properties deteriorate, becoming increasingly inflexible and brittle.

Dielectric composites include $CaCu_3Ti_4O_{12}$ in polyimide ($\varepsilon'_r = 3.2$) to give an effective dielectric permittivity of 49 and 12 at 40 and 20 vol% respectively [26]. Hot pressed lead zirconate titanate $PbZr_{0.52}Ti_{0.48}O_3$ (PZT at 70 vol%) in a PVDF matrix had a dielectric constant of 82.6 [27]. Higher loadings of ceramic filler can result in even higher dielectric constant (approximately 100), but degraded mechanical prop-

erties due to local strain inhomogeniety from the agglomeration of ceramic particles [28].

Conductive fillers such as carbon nanotubes, Ni and Ag particulates have been dispersed in a polymer matrix to achieve a high dielectric constant (> 100) due to percolation effects [29]. According to percolation theory, just before the dielectric breakdown of the polymer and at a critical volume fraction of filler, the conductive material forms a micro-capacitor network that dramatically increases the effective dielectric permittivity [29], while some useful mechanical flexibility of the composite might be preserved. Examples include PVDF containing aligned Zn flakes (0.03 to 0.21 vol%) fabricated by hot pressing into cubes (8 mm) with a dielectric constant of up to 176 [30]. However, the disadvantage of conductive fillers is very high loss (on the order of 0.2 or even > 2 [31]), and it is difficult to control the threshold fraction. For example, the dielectric constant increased from 200 to 2000 when the filler concentration increased from 11.03 to 11.43 vol%, and then reduced to nearly zero at 11.52 vol% [32].

The accurate prediction of effective permittivity in a composite is of importance in designing devices. Many analytical expressions and mathematical models have been developed to best-fit or predict the dielectric permittivity of composites. Factors that effect the dielectric permittivity include: filler volume fraction [32], dielectric constant of each component, filler morphology [33, 34], the nature of the interface between the ceramic and polymer [35], porosity, and environmental factors such as humidity and temperature. Some of the most popular formulas include the Clausius-Mossotti, the Maxwell-Garnett, the Bruggeman, and Lichtenecker logarithmic. Their formulas, limitations and applications are reviewed in [36]. In general, it remains difficult to predict composite properties from first principles and all the

most widely used analytical expressions, or more complex numerical models, tend to have at least one free fitting parameter. Sometimes these parameters can be related to physical attributes of the polymer (e.g. filler morphology), but these are not always convincing; fitting parameters have no obvious relationship to the composite character.

2.1.3 Characterization techniques

Accurate and appropriate (e.g. frequency specific) measurement of the dielectric properties of materials are important to the efficient design of devices based on local permittivity variations. Property determination of devices (rather than individual material samples or coupons) depends on so-called free space measurements (2D, 3D) of reflected and transmitted microwaves, and measurements are typically obtained in an anechoic chamber to minimise external reflections, where intensity, modulation, gain and directivity can be quantified. These techniques are in the domain of microwave engineering and are not discussed in detail here.

Various measuring techniques are available for characterization of material dielectric properties at the coupon scale, including non-resonant methods such as the coaxial probe, transmission line, parallel plate, and resonant methods such as a resonant cavity [37]. Depending on the frequency range and loss of the material, different measurements are chosen for characterization as shown in Figure 2.2.

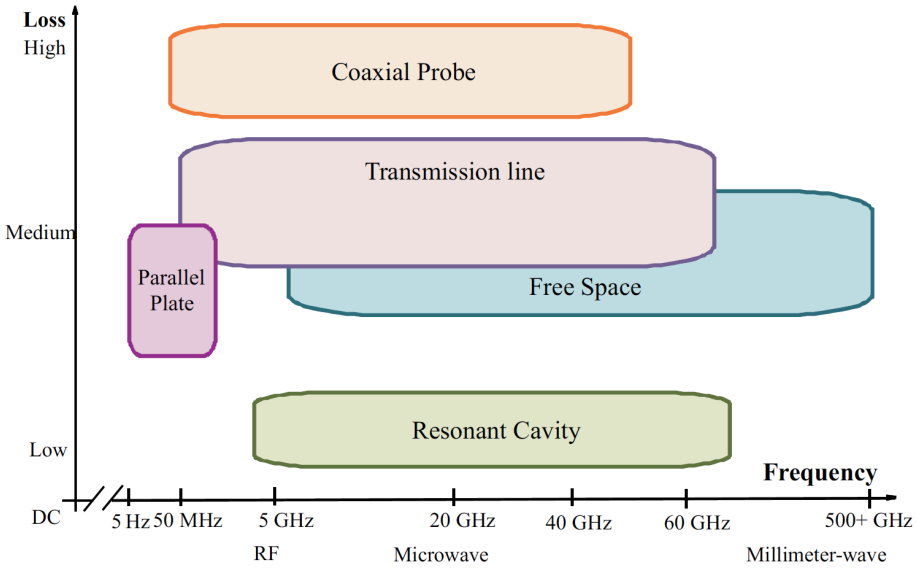


Figure 2.2: Different characterization techniques with their working frequencies and loss [38].

In the resonant method [38], when a sample is introduced into a resonant cavity, the dielectric properties of the sample can be derived from the change of the resonant frequency and the quality factor (Q) of the cavity. The quality factor is calculated from:

$$Q = \frac{f_0}{\Delta f} \tag{2.7}$$

Where f_0 is the resonant frequency and Δf is the frequency difference between 3 dB points. The resonant method is ideal for low loss dielectrics, usually with less than 1% uncertainty for the real part of permittivity, but is often limited to a narrow frequency band and puts demanding requirements on sample machining to a specific thickness, shape and tolerance. The procedure is as follows: measure the empty cavity resonant frequency and Q; insert the material and measure the loaded resonant frequency and Q; re-insert the material and measure again at various sample rotations; run software developed from theoretical models [39] to compute

permittivity from Q and f_0.

Non-resonant methods are used to calculate the dielectric properties across a broad frequency range, but tend to be considered relatively inaccurate for the measurement of low loss ($\tan\delta < 0.01$) materials.

In the transmission line measurement technique, a sample is placed in a section of a waveguide or coaxial line and a vector network analyzer (VNA) is used for measurement of reflection and transmission complex scattering parameters. The measurement of the reflected signal (S11) and transmitted signal (S21) are obtained from the VNA, which are used to calculate the complex permittivity and permeability of materials by one of three widely used conversion methods [38]: Nicholson-Ross-Weir (NRW) [40], National Institute of Standards and Technology (NIST) iterative [41], and short circuit line (SCL) [42]. Calibration must be performed prior to measurements, and samples should be machined for a tight fit into the waveguide to maximise accuracy.

In the coaxial probe method, the probe is pressed against a specimen (or immersed into liquid of interest) and the reflection coefficient is measured to determine the permittivity. This method requires no sample machining but only permittivity is available from the reflection coefficient.

In a free space method, measurements can even be taken under high temperature or in a controlled or hostile environment. Two antennas connected to VNA are placed facing each other and the usually flat sample is placed in between. The reflection and transmission coefficients are again used to calculate the permittivity and permeability of the sample. Table 2.3 summarizes the frequency range and sample requirement of each method and the measurement output [38].

Table 2.3: Various characterization methods with their operating frequency ranges and required sample state [38].

Method	Measurements output	Frequency range	Sample state
Coaxial probe	ε_r	Broadband	Liquid or semi-solid
Transmission line	ε_r, μ_r	Broadband	Solid
Free space	ε_r, μ_r	Broadband	Solid
Resonant cavity	ε_r	Single frequency	Solid

In this thesis, the resonant cavity method and transmission line method are used for characterizing printed coupons and their dielectric permittivity and loss in frequency range 12 to 18 GHz; the free space method is used to characterize the performance of printed devices by measuring the attenuation and phase shift of reflected and transmitted signals.

2.1.4 Summary

TO provides a design framework to manipulate EM waves by using local, spatially varying changes in permittivity and permeability to effect changes in the space coordinate, making the control of wave propagation possible in principle. The main limitation with the realization of TO inspired designs lies in the realization of such transformation media (with extreme or anisotropic permittivity and permeability values not available in natural materials) and their associated manufacturing technology. The development of meta-materials (resonant) or composite materials (non-resonant) with engineered structures or composition to provide tailored materials properties to enable desire functionalities not previously realizable.

2.2 Manufacturing Methods

Methods to manufacture all dielectric composite materials with spatially varying permittivities are discussed in this section including conventional methods such as spray deposition, extrusion, casting, etc., along with AM methods such as fused filament fabrication (FFF), also known as fused deposition modelling (FDM), polyjet, and stereolithography (SLA). Examples of various printed devices such as lenses, antennas, waveguides and others working at microwave frequencies are described.

2.2.1 Conventional methods

Spray deposition of polymer composites

Spray deposition may be an economical processing method for composite coatings, where a suspension of polymer and filler particles is atomized into droplets by a compressed gas to form a spray that then deposits onto a flat or rotating drum substrate [43]. The surface of the substrate can be flat or curved, and may support a flexible foil or polymer substrate. Depending on the polymer, an ultraviolet (UV) source can be used to polymerize a liquid monomer containing suspended particles, as it deposits and forms directly into a polymer coating [44]. Monomer based suspensions, aqueous or other solvent dispersions of fine particulates of thermo-polymers and fillers can also be spray deposited into coatings. In those cases, post spray thermal treatments are required to remelt the polymer, which wets the substrate and the particles, and re-solidifies into an ideally uniform composite coating. However, for devices that require in-plane spatial variations in properties, spraying struggles to achieve sufficient spatial control; moreover surface roughness can often be unacceptably high if there is some filler agglomeration [45]. For microwave devices, thicknesses typically on the order of millimeters or more are required due to the working wavelength of microwave frequencies (GHz), which is difficult for spray deposition, and it is thus restricted to applications such as a highly microwave absorbing surfaces in which lossy materials e.g. carbon nanotubes are embedded in a polymer coating.

Extrusion

Extrusion is widely used in the manufacture of thermoplastic polymers. The extrusion process starts with particulates or beads of materials that are transported from a hopper to a feed zone, compression zone, and then melting zone as shown in Figure 2.3 [46]. After the material is heated above its glass transition temperature T_g in the melting zone, it is pushed through a small orifice in a metallic die at the end of the barrel. The product formed has constant xy cross section and a length in the z direction of many meters. Extrusion is mainly used to produce homogeneous ceramic/polymer composite blends [47, 48]. Since no solvent is introduced during the process, minimal contamination or post processing is required.

Due to the wide range of material choices of ceramic polymer composites, extrusion can also be used to make filaments [49, 50] for AM process such as FFF. Operational variables including screw speed, pressure, and temperature that must be controlled for consistent filament diameter, and to account for swelling of the filament from the die due to elastic/plastic recovery [51]. Air voids may form at high filler fraction due to unwanted particle agglomeration, impairing polymer mixing, which are detrimental to subsequent mechanical properties, especially bend ductility. One way to reduce this tendency may be to increase the screw speed so that shear forces are generated or to increase the extrusion melting temperature [45]. However, high temperature (e.g. 170°C for a BTO/ABS composite) poses the risk of polymer degradation. Plasticizers and surfactants maybe used to modify the T_g of the polymer matrix to allow a lower extrusion temperature and a more uniform dispersion of ceramics fillers. The extruded filament geometry itself offers little practical direct use as a device material, and requires further processing into a wider range of shapes

and integration with other materials.

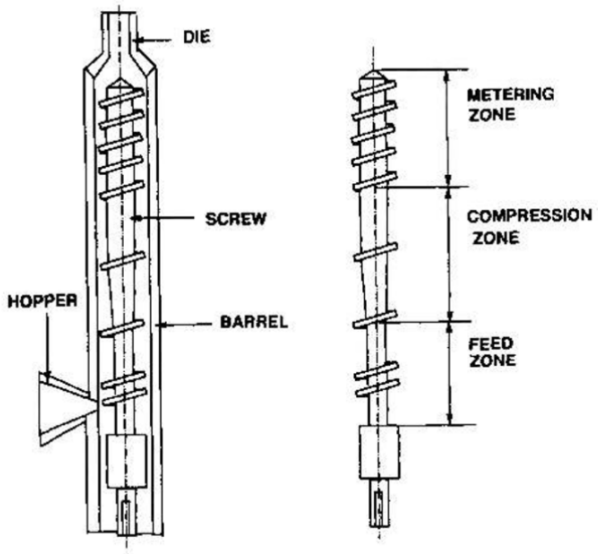


Figure 2.3: Schematic diagram of single screw extruder [46].

Casting

Casting is a cheap fabrication technology when high volume manufacturing is required [52]. A mold with desired shape is firstly prepared. Afterwards, liquid composite material is introduced to the mold. Then solidification or polymerization of the material takes place to form the final object with pre-designed geometry. Casting can produce complex shaped materials in three dimensions. Multiple materials can be processed to produce hybrid composites.

Examples in microwave applications can be seen in [53, 54]. A set of molds consisting of a 20 mm thick PTFE base with a 2 mm radius hole drilled in the middle with radii from 2 to 80 mm were fabricated for casting epoxy mixed with BTO powder with 0 to 42 vol% to make a beam-splitter lens with ε_r' ranging radially from 1.5 (edge) to 4.1 (centre), operating at 18 GHz. Although experimental results showed encouraging control over permittivity to achieve the intended beam splitting, improvements in the fabrication steps such as post manufacturing annealing (to relieve residual stress and warping) and reduction in any air gap between the mold rings, was required to improve permittivity control, the quality of the beam splitting operation, and to reduce manufacturing time. In addition, the cost of molds can be high and there are limitations on geometry of the structures arising from machining constraints and the inherent geometrical complexity of this multi-step casting approach [48].

Other methods

Less common methods for fabricating polymer-ceramic composites include ball milling for embedded capacitors for RF applications [55], and microwave curing of carbon nano-tube/epoxy composites [56]. Compression molding can also be employed to make all dielectric composite materials with comparable mechanical properties to 3D printing methods. For example, polypropylene (PP) with 30 wt% reinforced glass fiber was compress molded into 2 mm thick plates using a hot plate hydraulic press (at 230°C, 10 ton) and a plate mold [57]. Printed samples were 30% weaker than compression molding due to voids from poor adhesion between printed layers. However, by optimizing the print parameters (print orientation: parallel to the direction of the force applied; layer thickness: 3.5 mm to minimize the number of interfaces between filaments; infill percentage: 100%) the tensile properties of glass fiber reinforced printed samples was enhanced to approach those of PP-based compress molded samples. A disadvantage of compression molding is the cost of the mold and the inflexibility of design geometry, and multi-steps needed for graded and anisotropic materials.

2.2.2 Additive manufacturing

There are many AM methods for producing 3D objects at a scale suitable for potential microwave applications e.g. mms to cms. These include fused filament fabrication (FFF), polyjet and stereolithography (SLA) [58], and comprehensive reviews of their general capabilities can be found in [59–62]. AM also offers the possibility for relatively high spatial control in all directions; it may also offer more design flexibility in terms of materials choices and spatial control compared with conventional manufacturing methods, allowing for more dramatic 3D variations in local permittivity. Using materials mainly composed of polymers in AM has advantages including ease of processing, and low cost. AM techniques have been widely investigated using polymer materials such as ABS and PLA. Adding high dielectric fillers to polymers to produce printable composites with $\varepsilon_r > 10$, as previously described, provides potential advantages such as high material utilization, improved design flexibility and minimization of device physical size with the help of high dielectric constant materials compared to all polymer-based materials, typically with $\varepsilon_r < 3$ [63].

Fused filament fabrication

FFF is one of most widely used and early adopted AM processes (after stereolithography), and FFF machines are relatively inexpensive, robust and easy to use, although materials are almost exclusively restricted to polymer [64]. A FFF printer (and most others) typically takes "surface geometry" design files, denoted STL generated by the user using computer aided design (CAD) software. The STL file is encoded to a form understood by the FFF printer (G-code), which then executes the code and moves the print heads, and/or print substrate, and other actuators, according to the sequence and timing, and other parameters, described by the G-code. The STL file represents the 3D design as a stack of 2D layers of thickness on the order of 0.1 mm depending on 3D print parameters and techniques.

For FFF, the feedstock material is in the form of a filament that is fed into the print-head via a pinch roller mechanism through a guide tube (around 3 mm in diameter) and into a resistance heater (operating at up to 250°C) where the feedstock filament is heated above its glass-transition (T_g) temperature. The continuous feeding of solid filament acts as a piston to push the melt through the print nozzle orifice, usually with a diameter in the range 0.15 mm to 0.8 mm. A gantry typically moves the print-head in the xy-plane as material is deposited, starting with the object perimeter and then "filling in" on a heated build platform (around 110°C for ABS). The extruded material adheres to the substrate and then pre-deposited layers to form 2D patterns according to the STL file. The print bed lowers one thickness layer (typically 0.2 mm) in the z direction and another layer of material is then deposited. The printing process is then repeated until all the layers are deposited.

A schematic of FFF is shown in Figure 2.4 indicating that with a single filament

material, no overhangs or re-entrant shapes are possible, and temporary support structures must be used. Removal of support structures is usually manual and adds significant time and cost, and often leaves a degraded surface finish [57]. Internal re-entrants can only be achieved using a soluble second filament material e.g. ABS for primary structure, and water soluble PLA for the sacrificial support structure [65].

Typically, the filament is made of an amorphous thermoplastic and has a diameter of 1.75 mm to 3 mm. Polymer based composites with functional fillers are also used. For example, carbon fiber was used to increase the filament tensile strength of ABS/40 vol% Cu composite filaments [66]. In addition, conductive chains (percolation) formed of 20 vol% Cu particles so that thermal conductivity improved by an order of magnitude [66]. Similarly, 10 wt% single-walled carbon nanotubes were added to ABS to make filament for FFF with a 60% increase in tensile strength in the printed composite samples [67].

The addition of functional fillers to improve filament functional properties usually occurs at the expense of ductility due to increased resistance to chain mobility in the polymer and strain localization around the particles, especially around agglomerates. FFF process optimization and filament additives (e.g. plasticizers and surfactants) may provide a possible way to minimize filler agglomeration effects to achieve satisfactory melting behaviour and filament integrity, as well as functional properties. Successful demonstrations include TiO_2 added to ABS and PC blends functionalized with a silane agent to improve dispersion of the ceramics particles [68].

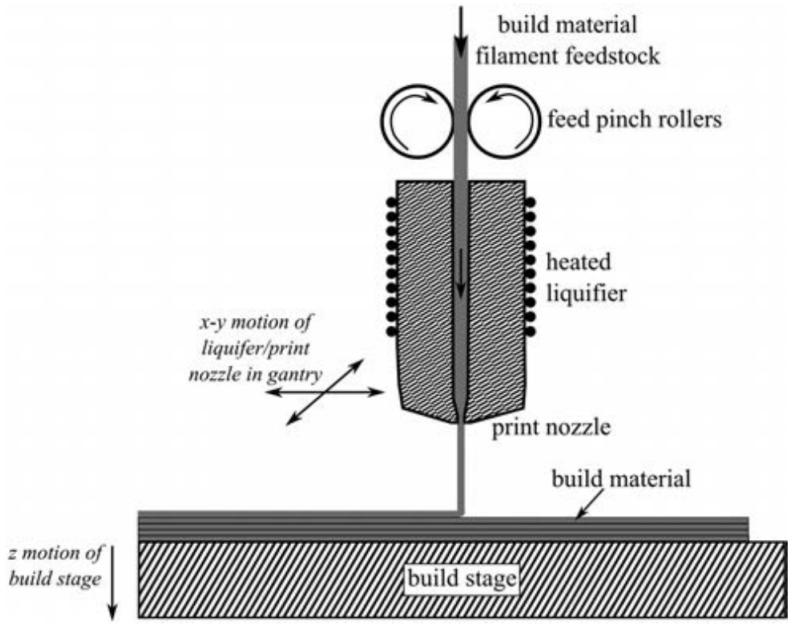


Figure 2.4: Schematic of the fused filament fabrication (FFF) additive manufacturing [69].

Key elements of the FFF process include the pinch roller feed mechanism, the heater (liquefier), print-head geometry, gantry, build platform and build environment [69]. Process variables include heating temperature (up to 250°C), bed temperature (approximately 110 °C for most commercial thermoplastics filaments, e.g. ABS), filament diameter, extrusion speed (typically 40 mm/s), feed rate (typically 40 mm/s), retraction speed (typically 20 mm/s), etc.

Most of the research on process parameters has been directed toward optimization surface roughness and dimensional accuracy for FFF of ABS [70]. The Taguchi technique and analysis of variance [71] have been used to determine the optimum surface finish and dimensional accuracy of a printed part with respect to process parameters such as layer thickness (0.178 mm, 0.254 mm and 0.33 mm), width (deposited filament beads width, 0.3048 mm, 0.5132 mm, and 0.7258 mm), raster angle

(angle between two consecutive layers, 0, 30 and 45°) and air gap (space between the deposited FFF beads, -0.001 mm, 0 mm and 0.001 mm) [72]. For example, the surface roughness was improved by using a smaller layer thickness. Air gaps had more effect on dimensional accuracy and little effect on surface roughness. A similar methodology was used to study the influence of part orientation, deposited filament bead width, layer thickness, air gap and raster angle on dimensional accuracy, with a layer thickness of 0.178 mm, part orientation of 0°, raster angle of 0°, deposited filament bead width of 0.456 mm and air gap of 0.008 mm giving the optimum accuracy of printed parts to a CAD model [73]. Further optimization details and other optimization methodologies (full factorial, fuzzy logic, and other statistical design techniques) and future prospects (other FFF materials such as PC, PC-ABS, etc) are given elsewhere [70].

Due to its relatively easy operation and relatively low cost, FFF is extensively used as a rapid prototype tool in applications ranging from medical treatment [74], mould design [49], and manifolds in automobile engineering [75]. Like other AM approaches, FFF can create complex and light-weight structures that are difficult to fabricate through conventional machining processes. Thus, they may cut down material cost, machining cost and save energy. For example, a FFF printed 13g wide-band radio antenna was 10 times lighter than a standard metal antenna [76]. Similar concepts include a printed waveguide with a 21% weight reduction over a conventionally fabricated component [77].

FFF can also use different polymer composites with a minority fraction of ceramic or metallic filler as feedstock filament with engineered properties or functionality. A highly conductive polymer composite filament with permittivity as high as 14.4 made of a polyester matrix and Cu was shown have a conductivity similar to

Cu [78]. Alternatively, a printed magnetic composite composed of polyethylene and Ni-Fe alloy (average particle diameter of 5 μm) successfully adhered to a magnet [79].

Common problems in FFF

1. Nozzle clogging

Blockage of the print nozzle is common due to absorption of moisture on the filament feedstock, which leads to problems such as morphological changes in the material, formation of air/stream bubbles and bulges on the surface of the printed material, ultimately clogging the print nozzle. Humidity and moisture also effect the diameter (typically 1.75mm) of the ABS filament ($\pm$ 4%) leading to increased nozzle clogging [80]. The effect of T_g was also investigated and showed there was a decrease in T_g due to moisture absorption and a higher operating temperature required to ensure the viscosity and flow behavior of the ABS remained within the operating window of the print-head. Optimally, the printing environment should be near to dry room conditions and the filament kept dry by storing in a desiccator.

2. Low resolution

Another disadvantage of FFF comes from its limited resolution (typically 0.25 mm) [59]. In general, the size of the nozzle orifice determines the feature resolution that can be achieved in the final printed part, and the surface roughness. In practice, diameters below 0.15 mm are impractical. Attempts to decrease the exit orifice diameter are limited by the increase in extrusion pressure required, the reduction in material extrusion rate, increase in extrusion speed (at a constant extrusion rate), and surface tension.

Other routes to improve surface roughness and resolution include chemical and mechanical smoothing, as well as surface coatings [69]. Chemical smoothing systems

use vapours which condense on the surface and partially melt small ridges. For example, acetone heated to 57°C was used to smooth the surface of ABS printed parts with a layer thickness of 0.254 mm. Roughness was significantly reduced from an average of 2960 nm to 37 nm. In addition, the mechanical properties of ABS printed parts improved slightly because the voids between layers were preferentially filled on drying with re-precipitated material dissolved into the acetone [81]. However, multi μm resolution achievable by FFF is generally sufficient for devices working at microwave frequencies.

3. Warping and residual stresses

The surface of the heated platform is of critical importance as the first deposited filament must adhere to the surface, but not so well that the part becomes too difficult to remove. Thermal gradients will also always exist in forming parts, which can lead to warping and distortion due to differential rates of thermal expansion/contraction. The extruded material cools quickly from the melting temperature (around 240°C) to the print platform temperature (around 100°C), resulting in shrinkage that can lead to residual stress if the shrinkage is anisotropic (as is usually the case), which might lead to inter and intra-layer deformation in the form of cracking, or delamination.

Potential solutions have been suggested, for example, the scan speed [82]. Simulations have shown that scan speed and tool path likely had the most significant effect on distortion, followed by the layer thickness. An algorithm was proposed to match the tool path with the scan speed to minimize residual stress and to eliminate voids, as well as correcting for overfill and under-fill defects [83]. However, FFF machines generally lack any real time control and simulation tools for off-line optimization are not widely available or of generic capability.

Applications of printed devices at microwave frequencies

1. FFF of polymers

Many demonstrator devices for use in the microwave domain have been realized by FFF [84–87]. However, the materials used tend to have permittivities that lie between air ($\varepsilon_r = 1$) and FFF thermoplastics ($\varepsilon_r' = 2.45$ to 3, $\tan\delta = 10^{-3}$). By controlling the local air fraction using designed lattice or void structures, sometimes referred to as log-pile designs, sub-wavelength (limited) variations in local permittivity can be achieved. A flat, graded-index lens shown in Figure 2.5(a) was fabricated with six 10 mm wide discrete concentric rings using polylactic acid ($\varepsilon_r = 2.72$) and a lattice structure to transform spherical waves into plane waves [87]. The effective permittivity was controlled by the local fraction of air with a permittivity of 1.3 in the outermost ring and 2.72 in the center ring. The lens weighed 130 g and the material cost was less than $10, which was lower than a traditionally fabricated lens with similar performance.

Local changes in permittivity can also be achieved by changing the orientation of the unit cells. A polycarbonate-ABS blend with $\varepsilon_r = 2.45$ was used to fabricate a self-supporting lattice that produced beam collimation at 15 GHz shown in Figure 2.5(b), using a spatially varying permittivity [16]. Manipulation of the incident EM wave was achieved by varying the orientation of the cubic unit cells from place to place in the printed lattice. Experimental data showed that the lattice induced a microwave beam to bend 90°without significant scattering, and was the first influential example that exploited spatial variation of the orientation of unit cells in a lattice. However, due to the low permittivity contrast ($\Delta\varepsilon_r = 1.45$) available between different regions, the device (40 cm in length) took two weeks to print.

Although FFF of polymers can create complex structures and light-weight devices, availability of high permittivity filament (> 10) is limited. Filling the voids or

voxels of printed structure with high permittivity powders (e.g. TiO_2 with ε_r' of 40) may enable a wider range of permittivity, leading to device miniaturization but has yet to be demonstrated reliably and with controllable permittivities [78] .

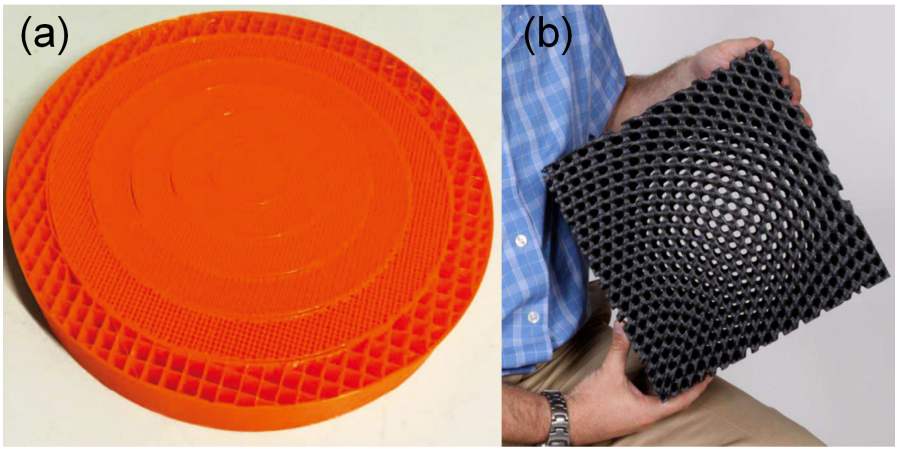


Figure 2.5: (a) A graded-index lens produced by FFF with PLA for transforming spherical waves emanating from the focal point into plane waves. The lens comprised of 6 × 10mm wide discrete dielectric concentric rings with lowest permittivity of 1.3 in the outmost ring to highest permittivity of 2.72 in the center ring [87], and (b) a polycarbonate-ABS lattice produced by FFF with fill fraction of 30%. The lattice composed of $22\times22\times22$ cubic unit cells with same lattice spacing, but the orientation of the unit cell being spatially varied and the radius of the curve varying by more than × 20 across the device to allow beam bending of 90°[16].

2. FFF of polymers with functional fillers

A gradient refractive index lens for a directive antenna [17] and a functional medical imaging transducer [88] were fabricated with 30 vol% of BTO in ABS, and 30 vol% of lead zirconate titanate (PZT) ceramic filament in a hard epoxy, respectively. A sub-wavelength variation in spacing between a BTO/ABS filament and a ABS only filament is shown in Figure 2.6(a) to achieve a progressive increase in local permittivity from the edge to the center of the lens for the control of phase velocity. A similar technique was used in Figure 2.6(b) with alternating layers of PZT and

epoxy. With the addition of the resulting printed gradient index lens, a shorted horn with length of 2λ was shown to have the same directivity as a horn with an optimized length of 6λ but without a lens, where antenna size was denoted as relative to operation wavelength [89].

A polyethylene ($\varepsilon_r = 2.3$) matrix filled with 81Ni-Fe alloy filler was fabricated into a filament of 3 mm diameter for FFF printing of a microwave absorbing material for applications at 3 GHz [79]. Various volume fractions of 20, 30 and 40 were studied with $\varepsilon_r = 4.6$, 6.3 and 9.2 respectively and the printed composite also showed static magnetisation. A similar concept was utilized in [78] using Cu filler to make a conductive filament, with high electrical conductivity suitable for microwave resonator meta-material applications.

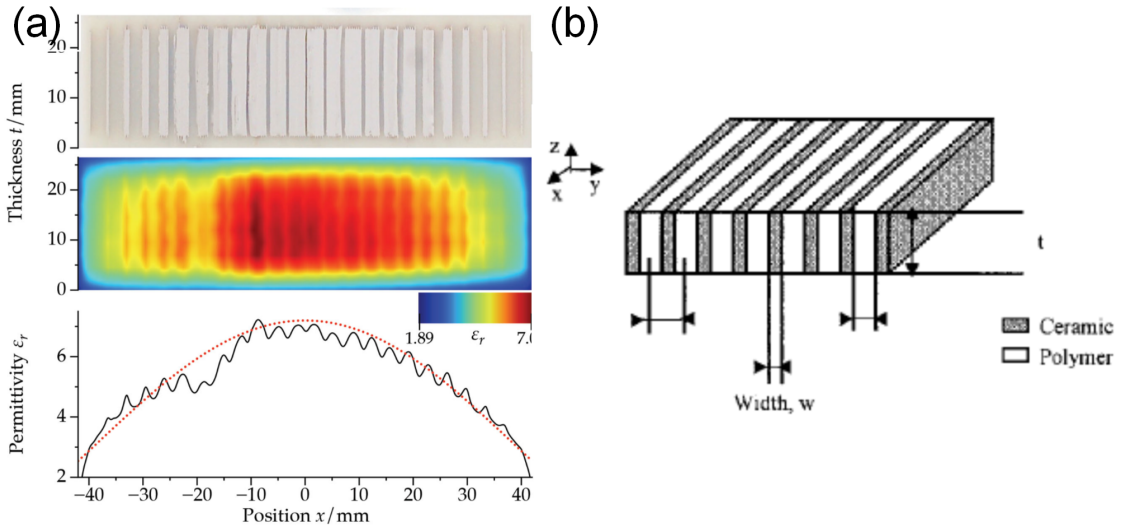


Figure 2.6: (a) A gradient refractive index flat lens made by FFF of BTO/ABS and ABS. The top two images show the variation in BTO/ABS filament fraction with position in the lens, from highest fraction in the middle to low fraction on the sides, giving highest permittivity in the middle, gradually reducing to low permittivity at the edges. The lower graph shows the experimental measurements of the spatial distribution of relative permittivity across the lens obtained using a SPDR technique along with a comparison of the measured (solid line) and the ideal theoretical (dotted line) radial variation in local permittivity [17], and (b) PZT/epoxy composite used for making a transducer by FFF. The composite comprised of alternating parallel plates of ceramic (in grey) and polymer (in white). The width of the ceramic plate was dictated by the nozzle diameter and spacing between the parallel plates was determined by the desired volume fraction of the ceramics [88].

3. Combining FFF with other techniques

FFF can be combined with other conventional or AM techniques to fabricate devices. In [76], Ni and Cu were chemically deposited at thicknesses of 0.23 μm and 2.76 μm on a FFF ABS printed broadband radio antenna working at 14 to 18 GHz. Good bonding between the metals and ABS was confirmed by dynamometric test and the printed antenna was 10 times lighter than a similar metal prototype, with no significant difference for radio performance in an anechoic chamber (gain similarity of 95% for the H-plane and 97% for the E-plane).

Ag ink was chemically deposited for the surface metallization and to cut down the cost associated with Ag. A fully printed meshed ground coplanar waveguide was fabricated using a substrate of ABS ($\varepsilon_r = 2.37$ at 4.36 GHz) with acceptable performance of 9.3% increase in attenuation constant compared with a reference line [86]. However, the conductivity of the Ag ink was one tenth of bulk Ag, and would normally be annealed at 550 °C, but this would fully decompose and vaporise the ABS.

To avoid high temperature metal-based ink annealing processes, a metal wire mesh approach was also been used to impart electrical conductivity [84, 85]. A 90mm long multilayer micro-strip line operating at 10 GHz was made with ABS ($\varepsilon_r = 2.7$, $tan\delta = 0.01$) as the substrate by FFF and then a Cu mesh was embedded. The measured reflection coefficients were smaller than -7dB for all the frequencies and consistent with simulations. With optimized print parameters and lower loss FFF polymers, the reflection coefficient might be further reduced. A patch antenna was fabricated in the same way but with polyethylene as the substrate ($\varepsilon_r = 2.4$) and a Cu mesh. Again, there was good agreement between experimental data and simulations for reflection coefficient and far field radiation patterns, but at a lower fabrication cost than the conventional methods.

Polyjet

In the polyjet process, a photo-curable polymer is jetted from an inkjet head that moves in the xy-plane, onto a platform that moves in the z direction. After the polymer is deposited, it is cured by ultraviolet light as shown in Figure 2.7. A gel-type polymer, which is dissolvable in water, can be used for supporting overhang features where needed. Like FFF, polyjet operates directly from STL files. Typical layer thickness is approximately 16 μm compared with 25 μm or much larger for FFF. Polyjet is most commonly used to fabricate light-weight structures in the automotive and aerospace industry, for architectural modelling, medical applications and for art sculptures [59].

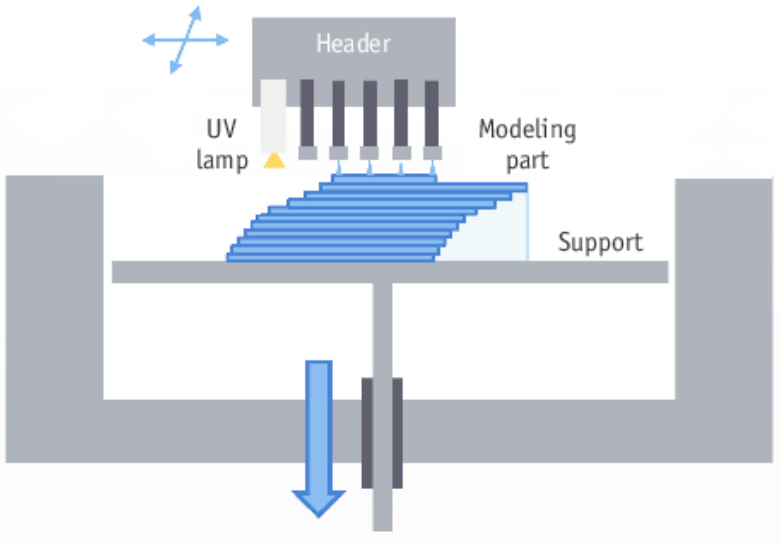


Figure 2.7: Schematic of polyjet printing process [90].

Examples of polyjet for fabricating devices operating at microwave frequency include a broadband (8 to 12 GHz) graded refractive index lens using a photo-curable

polymer ($\varepsilon_r = 2.8$) with designed air voids to achieve a variation in permittivity from 1.5 to 2.6 [18]. Electric field and far field radiation patterns confirmed beam steering behavior (28 °) as intended by simulation. In [91], a low gain 20 dBi, 4λ (12 cm) 3D Luneburg lens antenna, shown in Figure 2.8(a), was fabricated to operate at 8.2 to 12.4 GHz, with a layer thickness of 16 μm. A variation in permittivity profile was achieved by changing the size of the printed polymer cubes and the filling ratio of the polymer. The printed antenna showed good agreement with simulated results (gain of 18.5 dB) with a total print time less than four hours and a cost less than $100.

Another example of a polyjet antenna is shown in Figure 2.8(b) operating at 5.45 GHz, fabricated using an opaque photopolymer ($\varepsilon_r = 2.4$), and then coated with Ti and Cu with a measured gain of 6.94 dBi, in good agreement with simulations [92]. A multi-layer patch antenna of length 29.65 mm was also printed to investigate broad band operation, with a slight difference in operational frequencies compared with design due to air gaps between the ground plane and the dielectric layer.

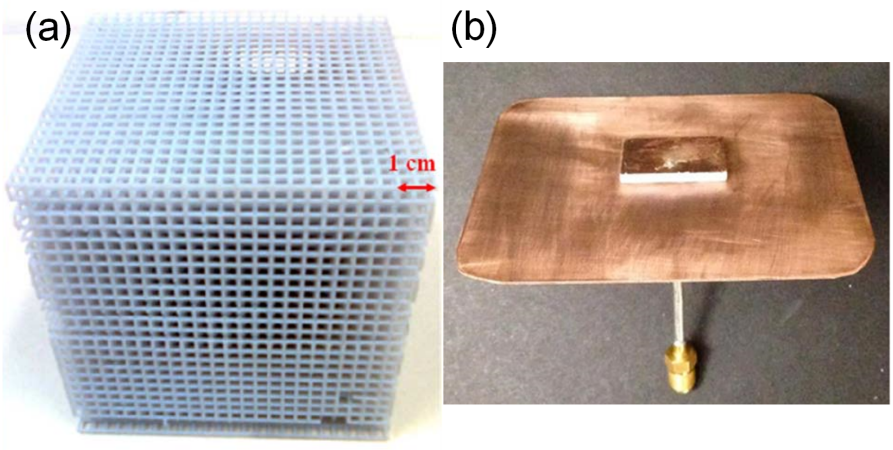


Figure 2.8: (a) A Luneburg lens made by polyjet. The lens (length of 24 cm) was comprised of different sized polymer cubes (5 mm) to manipulate the local dielectric permittivity distribution. Thin rods were used to connect all the cubes and support the whole structure [91], and (b) a metallized patch antenna made by polyjet. The dielectric substrate was sandwiched between a metallized ground plane at the bottom and a metallized radiating patch on top. A coaxial cable was attached from the back side and the center conductor was affixed to the top metal layer using Ag epoxy [92].

Polyjet has the advantage of low cost, and relative freedom to create complex geometries. However, the disadvantage lies in the weaker bonding between layers or air gaps between ground plane and dielectrics when compared with FFF, leading to poor mechanical properties or discrepancies in designed and operational frequencies. In addition, polyjet cannot process multiple materials in one print job, and so the control of local permittivity variation is achieved only through changing the local air fraction, giving restrictions in the dielectric contrast available.

Stereolithography (SLA)

In SLA, a photosensitive resin, which cannot be melted again for reuse, is contained within a tank [93]. A laser beam typically with diameter of 50 μm scans a thin (typically 25 μm) layer of the resin, which has been carefully coated over the build platform that sits within the tank (see Figure 2.9). After one 2D pattern layer is cured by the lasers according to the STL file, the platform is lowered and a fresh layer of viscous resin is coated over the solid layer using a sweeper/recoater. After all the layers are cured, the 3D part is rinsed of excess resin and then fully cured in a UV oven. Because the part is created in liquid, overhanging regions need support, which are trimmed afterwards. The accuracy achieved is approximately 0.1% of the overall dimensions [93].

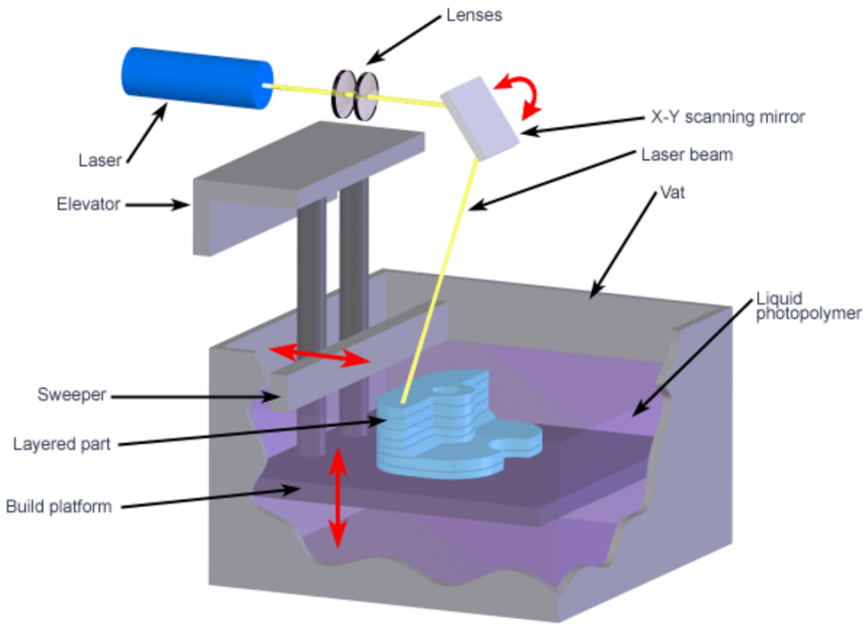


Figure 2.9: Schematic of stereolithography (SLA) printing process [77].

The waveguides shown in Figure 2.10(a) were fabricated using SLA with commercial Accura Xtreme resin and then Cu electroplated [77], with internal cross-sectional dimensions of 2.54 mm by 1.67 mm for the rectangular slot and 60 mm for length. Compared with FFF, a smoother surface (0.93 μm for stereolithography and 4.02 μm for FFF) as well as smaller feature size was achieved due to the low viscosity of resin, and smaller diameters of the laser beam than the FFF nozzle orifice. Due to the internal dimensions of the waveguide design being too small for metal plating, the waveguide was printed as two pieces and then assembled. Even with this assembly step, SLA proved to give accurate alignment and the measured insertion loss of the structure was only 0.95 dB and with an unloaded quality factor of 152, which were comparable with those of standard waveguides. Moreover, the cost for the SLA waveguide was lower than a traditional machined metal waveguide. A horn antenna shown in Figure 2.10(b) was fabricated by SLA (with dimensions of 40.2 mm by 29.3 mm by 51 mm) with measured gain and radiation patterns similar to simulations [94].

However, there are significant drawbacks of SLA, including the limited choices, cost and toxicity of the resins and high capital cost of the equipment. In addition, the equipment must be shielded from light to avoid premature polymerization. Parts have high surface hardness but are brittle, although in [95], filler reinforced resin was used with <5 wt% carbon nano-tubes to achieve an increase in tensile strength of 57% and a higher stiffness than an unfilled equivalent.

Resins may be loaded with a suspension of filler particles, such as 50 vol% ceramic, including alumina, silica, hydroxyapatite and 50 vol% uv-polymerized binder, with a low viscosity of < 5000 cps [96] to create 3D composite parts, but are susceptible to shrinkage cracking, and again support structures are required during the

print [97].

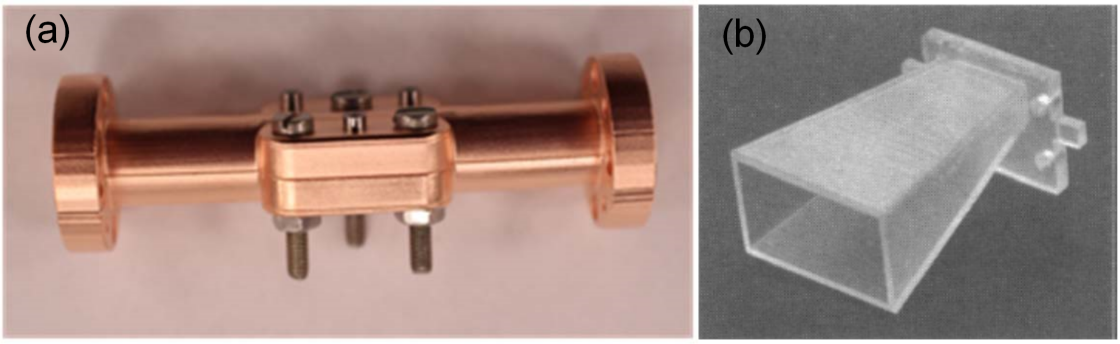


Figure 2.10: (a) A waveguide fabricated by SLA and then Cu-plated, assembled from two split blocks [77], with total length of 60 mm, and (b) a horn antenna fabricated by SLA and then metallized with conductive Ag ink. The dimensions are $40.2 \times 29.3 \times 51$ mm [94].

2.2.3 Summary

AM offers a potential manufacturing method for a variety of devices working at microwave frequencies, with the capability to achieve light-weight structures by the use of carefully designed distributions of pores, lattices, etc. The manufacturing flexibility of AM allows some verification of designs based on TO by providing some control of local permittivity in model devices. In all but the most recent work, local permittivity can vary only between that of air and the printed polymer, as the lower and upper bound respectively, giving a limited dielectric contrast. More recent work uses fillers to increase the dielectric contrast, while maintaining printability. Amongst AM techniques, FFF has been studied most widely as it exploits the relative ease of fabrication with commoditized polymers, and multi-material FFF can fabricate graded and anisotropic materials. FFF composite materials are limited to polymer-base, but can be readily integrated with other materials by post-processing so long as high temperatures are avoided. Even though FFF does not provide the best feature resolution amongst AM techniques, for devices working at mm wavelengths, this has not been shown to be critical.

Bibliography

[1] D. H. Kwon and D. H.Werner, Transformation electromagnetics: An overview of the theory and applications,IEEE Antennas and Propagation Magazine,vol. 52, no. 1, 2010.

[2] M. Lax and N. D.F, Maxwell equations in material form, vol. 13, no. 4, 1975.

[3] Y. Liu and X. Zhang, Recent advances in transformation optics, Nanoscale, vol. 4, no. 17, 2012.

[4] D. Schurig, J. B. Pendry, and D. R. Smith, Calculation of material properties and ray tracing in transformation media, vol. 14, no. 21, 2006.

[5] B. N. B. Kundtz, D. R. Smith, and J. B. Pendry, Transformation Optics, Proceedings of the IEEE, vol.99, no.10, 2011.

[6] H. Chen, C.T. Chan and P. Sheng, Transformation optics and metamaterials, Nature Materials, vol.9, pp.387–396, 2010.

[7] R. Foster, P. Grant, Y. Hao, A. Hibbins, T. Philbin, R. Sambles, Spatial transformations: from fundamentals to applications, Phil. Trans. R. Soc. A.37320140365, 2015.

[8] G. W. Milton, M. Briane, and J. R. Willis, On cloaking for elasticity and physical equations with a transformation invariant form, New Journal of Physics, vol.8, no.248, 2006.

[9] K. L. Y.Hwang, Y.P. Zhang and E. Yung, Gain-enhanced miniaturised rectangular dielectric resonator antenna, Electronics Letters, vol.33, no.24, pp.350 – 352, 1997.

[10] S. Lei, H. Fan, X. Ren, J. Fang, L. Ma, and H. Tian, Microstructure, phase evolution and interfacial effects in a new $Zn_{0.9}Mg_{0.1}TiO_3 - ZnNb_2O_6$ ceramic system with greatly induced improvement in microwave dielectric properties, Scripta Materialia, vol. 146,pp.154-159, 2018.

[11] R. C. Rumpf, J. J. Pazos, J. L. Digaum and S. M. Kuebler, Spatially variant periodic structures in electromagnetics, Philosophical Transactions, Series A, no.2049, 2015.

[12] J. Pendry, Extremely Low Frequency Plasmons in Metallic Microstructures, Phys. Rev. Lett, vol.76, 4773, 1996.

[13] J. B. Pendry, A. J. Holden, D. J. Robbins, and W. J. Stewart, Magnetism from conductors and enhanced nonlinear phenomena, IEEE Transactions on Microwave Theory and Techniques, vol.47, no.11, pp.2075-2084, 1999.

[14] I. Gil, J. Bonache, J. Garca-Garca, and F. Martn, Tunable metamaterial transmission lines based on varactor-loaded split-ring resonators, IEEE Transactions on Microwave Theory and Techniques, vol.54, no.6, 2006.

[15] V. G. Veselago, The electrodynamics of substances with simultaneously negative values of ϵ and μ, Soviet Physics Uspekhi, vol.10, no.4, 1968.

[16] R. Rumpf and J. Pazos, 3D Printed Lattices with Spatially Variant Self-Collimation, Progress In Electromagnetics Research, vol.139, pp.1-14, 2013.

[17] D. Isakov, C. J. Stevens, F. Castles, and P. S. Grant, 3D-Printed High Dielectric Contrast Gradient Index Flat Lens for a Directive Antenna with Reduced Dimensions, Advanced Materials Technologies, vol. 1, 1600072, 2016.

[18] J. Yi, S. N. Burokur, G.-P. Piau, and A. de Lustrac, 3D printed broadband transformation optics based all-dielectric microwave lenses, Journal of Optics, vol. 18, 044010, 2016.

[19] L. Li, B. Zhang, and X. M. Chen, Dielectric characteristics of polyvinylidene uoride-polyaniline percolative composites up to microwave frequencies, Applied Physics Letters, vol. 103, no. 19, 192902, 2013.

[20] D. Sandi, A. Supriyanto, Anif, Jamaluddin, and Y. Iriani, The effects of sintering temperature on dielectric constant of Barium Titanate, IOP Conference Series: Materials Science and Engineering, vol. 107, 2016.

[21] R. C. Kell, A. C. Greenham, and G. C. Olds, High permittivity temperature stable ceramic dielectrics with low microwave loss, Journal of the American Ceramic Society, vol.56, no.7, pp.352-354, 1973.

[22] M. Born and E. Wolf, Principles of Optics, sixth edition, 1980.

[23] D. Pozar, Microwave Engineering. Wiley, 1997.

[24] G. Arlt, D. Hennings, and G. D. With, Dielectric properties of fine grained barium titanate ceramics, Journal of Applied Physics 58, 1619 ,1985

[25] A. R. West, T. B. Adams, F. D. Morrison, and D. C. Sinclair, Novel high capacitance materials: $BaTiO_3$ and $CaCu_3Ti_4O_{12}$, Journal of the European Ceramic Society, vol.24, no.6, pp.1439-1448, 2004.

[26] Z. M. Dang, T. Zhou, S. H. Yao, J. K. Yuan, J. W. Zha, H. T. Song, J. Y. Li, Q. Chen, W. T. Yang, and J. Bai, Advanced calcium copper ti-tanate/polyimide functional hybrid films with high dielectric permittivity, Advanced Materials, vol.21, no.20, pp.2077-2082, 2009.

[27] D. Zhang, D. Wang, J. Yuan, Q. Zhao, Z. Wang and M. Cao, Structural and

electrical properties of PZT/PVDF piezoelectric nanocomposites prepared by cold-press and hot-press routes, Chin. Phys. Lett, vol.25, 2008.

[28] S. P. Marra, K. T. Ramesh, and A. S. Douglas, The mechanical properties of lead-titanate/polymer 0-3 composites, Composites Science and Technology, vol. 59, no. 14, pp.2163-2173, 1999.

[29] M. Basta, V. Picciarelli, and R. Stella, An introduction to percolation, Taylor & Francis 1994.

[30] Y. Zhang, Y. Wang, Y. Deng, Y. Guo, W. Bi, M. Li, Y. Luo, and J. Bai, Excellent dielectric properties of anisotropic polymer composites filled with parallel aligned zinc flakes, Applied Physics Letters, vol. 101, no. 19, 2012.

[31] L. Qi, B. I. Lee, S. Chen, W. D. Samuels, and G. J. Exarhos, High-dielectric constant silver-epoxy composites as embedded dielectrics, Advanced Materials, vol.17, no.14, pp.1777-1781, 2005.

[32] F. He, S. Lau, H. L. Chan, and J. Fan, High dielectric permittivity and low percolation threshold in nanocomposites based on polyvinylidene and exfoliated graphite nanoplates, Advanced Materials, vol.21, no.6, pp.710-715, 2009.

[33] Y. Dang, Y. Wang, Y. Deng, M. Li, Y. Zhang, and Z. Zhang, Enhanced dielectric properties of polypropylene based composite using Bi_2S_3 nanorod filler, Progress in Natural Science: Materials International, vol.21, no.3, pp.216-220, 2011.

[34] B. H. Fan, J. W. Zha, D. Wang, J. Zhao, and Z. M. Dang, Size-dependent low-frequency dielectric properties in the $BaTiO_3$/poly(vinylidene nanocomposite films, Applied Physics Letters, vol. 100, no. 1, 2012.

[35] Q. Xiao, L. Li, B. Qing Zhang, and X. Ming Chen, Polyvinylidene modified $BaTiO_3$ composites with high dielectric constant and temperature stability, Ceramics International, vol. 39, 2013.

[36] L. Jylha, Modelling of electrical properties of composites, Helsinki University of Technology, PhD thesis, 2008.

[37] Agilent Technologies, Basics of Measuring the Dielectric Properties of Materials, Application Note, 2006.

[38] K. C. Yaw (Rohde& Schwarz), Measurement of dielectric material properties Application Note, Measurement Techniques, 2006.

[39] M. D. Janezic, J. Baker-jarvis, and S. Member, Full-Wave Analysis of a Split-Cylinder Resonator for Non-destructive Permittivity Measurements, vol.47, no.10, pp.2014-2020, 2014.

[40] A. S. N. R.Weir-based, O. Luukkonen, S. I. Maslovski, and S. A. Tretyakov, A stepwise Nicolson-Ross-weir Material Parameter Extraction Method, IEEE Antennas and Wireless Propagation Letters, vol.10, 2011.

[41] J. Baker-Jarvis, M. Janezic, J. Grosvenor, and R. Geyer, Transmission/Reflection and Short-Circuit Line Methods for Measuring Permittivity and Permeability. NIST, United States Department of Commerce, 1990.

[42] D. L. Faircloth, M. E. Baginski, S. Member, and S. M. Wentworth, Complex Permittivity and Permeability Extraction for Multilayered Samples Using S - Parameter Waveguide Measurements, IEEE Transactions on Microwave Theory and Techniques, vol.54, no.3, pp.1201-1209, 2006.

[43] P. S. Grant, F. Castles, Q. Lei, Y.Wang, J. M. Janurudin, D. Isakov, S. Speller, C. Dancer, and C. R. Grovenor, Manufacture of electrical and magnetic graded and anisotropic materials for novel manipulations of microwaves, Philosophical Transactions A, vol.373, no.2049, 2015.

[44] X. Zhao, C. Hinchlie, C. Johnston, P. J. Dobson, and P. S. Grant, Spray deposition of polymer nanocomposite films for dielectric applications, Materials Science and Engineering B: Solid-State Materials for Advanced Technology, vol.151, no.2, pp.140-145, 2008.

[45] D. A. Barrow, T. E. Petro, and M. Sayer, Thick ceramic coatings using a sol gel based ceramic-ceramic 03 composite, Surface and Coatings Technology, vol. 76-77, pp.113-118, 1995.

[46] S. J. Kim and T. H. Kwon, Enhancement of mixing performance of single-screw extrusion processes via chaotic flows: Part I. Basic concepts and experimental study, Advances in Polymer Technology, vol.15, no.1, pp.41-54, 1996.

[47] L. M. Mathieu, P. E. Bourban, and J. A. E. Manson, Processing of homogeneous ceramic/polymer blends for bioresorbable composites, Composites Science and Technology, vol.66, pp.1606-1614, 2006.

[48] R. Janssen, S. Scheppokat, and N. Claussen, Tailor-made ceramic-based components-Advantages by reactive processing and advanced shaping techniques, Journal of the European Ceramic Society, vol.28, no.7, pp.1369-1379, 2008.

[49] S. H. Masood and W. Q. Song, Development of new metal/polymer materials for

rapid tooling using Fused deposition modelling, Materials and Design, vol.25, no.7, pp.587-594, 2004.

[50] F. Castles, D. Isakov, A. Lui, Q. Lei, C. E. J. Dancer, Y. Wang, J. M. Janurudin, S. C. Speller, C. R. M. Grovenor, and P. S. Grant, Microwave dielectric characterisation of 3D-printed $BaTiO_3/ABS$ polymer composites, Scientic reports, vol.6, 22714, 2016.

[51] C. Rauwendaal, Polymer Extrusion, Polymer Processing Institute, Hanser, 1994.

[52] G. Withers, A low cost, light weight aluminium metal matrix composite for braking applications, National Instruments ans SAE, 2008.

[53] Q. Lei, R. Foster, P. S. Grant, and C. Grovenor, Generalized Maxwell Fish-Eye Lens as a Beam Splitter: A Case Study in Realizing All-Dielectric Devices From Transformation Electromagnetics, IEEE Transactions on Microwave Theory and Techniques, pp.1-13, 2017.

[54] O. Quevedo-Teruel, W. Tang, R. C. Mitchell-Thomas, A. Dyke, H. Dyke, L. Zhang, S. Haq, and Y. Hao, Transformation optics for antennas: Why limit the bandwidth with metamaterials?, Scientic Reports, vol.3,1903, 2013.

[55] S. Ogitani, S. Bidstrup-Allen, and P. Kohl, Factors influencing the permittivity of polymer/ceramic composites for embedded capacitors, IEEE Transactions on Advanced Packaging, vol.23, no.2, pp.313-322, 2000.

[56] P.-c. Sung, T.-h. Chiu, and S.-c. Chang, Microwave curing of carbon nanotube/epoxy adhesives, Composites Science And Technology, vol.104, pp.97-103, 2014.

[57] O. S. Carneiro, A. F. Silva, and R. Gomes, Fused deposition modelling with polypropylene, Materials and Design, vol.83, pp.768-776, 2015.

[58] W. J. Otter and S. Lucyszyn, 3D printing of microwave components for 21st century applications, 2016 IEEE MTT-S International Microwave Workshop Series on Advanced Materials and Processes for RF and THz Applications, 2016.

[59] K. V. Wong and A. Hernandez, A Review of Additive Manufacturing, ISRN Mechanical Engineering, vol.2012, 2012.

[60] M. Vaezi, H. Seitz, and S. Yang, A review on 3D micro-additive manufacturing technologies, International Journal of Advanced Manufacturing Technology, vol.67, no.5-8, pp.1721–1754, 2013.

[61] H. Bikas, P. Stavropoulos, and G. Chryssolouris, Additive manufacturing methods and modelling approaches: A critical review, International Journal of Advanced Manufacturing Technology, vol.83, no.1-4, pp.389–405, 2016.

[62] J. O'Donnell, M. Kim, and H.-S. Yoon, A Review on Electromechanical Devices Fabricated by Additive Manufacturing, Journal of Manufacturing Science and Engineering, vol.139, no.1, 2016.

[63] J. G. Drobny, Polymeric Materials. John Wiley Sons, Inc., 2012.

[64] T.Wohlers, W. Associates, R. Campbell, and T. Carey, Wohlers Report 2016: 3D Printing and Additive Manufacturing State of the Industry : Annual Worldwide Progress Report. Wohlers Associates, 2016.

[65] T. Grimm, Fused deposition modelling: A technology evaluation, T. A. Grimm & Associates, Inc., vol.11, no.2, 2003.

[66] M. Nikzad, S. H. Masood, and I. Sbarski, Thermo-mechanical properties of a highly filled polymeric composites for Fused Deposition Modeling, Materials and Design, vol. 32, no. 6, pp. 3448-3456, 2011.

[67] M. L. Shofner, K. Lozano, F. J. Rodrguez-Macas, and E. V. Barrera, Nanober-reinforced polymers prepared by fused deposition modeling, Journal of Applied Polymer Science, vol. 89, no. 11, pp.3081-3090, 2003.

[68] D. Roberson, C. M. Shemelya, E. Macdonald, and R. Wicker, Expanding the applicability of FDM-type technologies through materials development, Rapid Prototyping Journal, vol. 2, 2015.

[69] D. Espalin, J. Alberto Ramirez, F. Medina, W. M. Johnson, M. Rowell, B. Deason, M. Eubanks, B. N. Turner, R. Strong, and S. A. Gold, Rapid Prototyping Journal A review of melt extrusion additive manufacturing processes: I. Process design and modeling, Rapid Prototyping Journal, vol. 20, no.3, 2014.

[70] O. A. Mohamed, S. H. Masood, and J. L. Bhowmik, Optimization of fused deposition modeling process parameters : a review of current research and future prospects, Advances in Manufacturing, vol. 3, pp. 42–53, 2015.

[71] R. Anitha, S. Arunachalam, and P. Radhakrishnan, Critical parameters in enhancing the quality of prototypes in fused deposition modelling, Journal of Materials Processing Technology, vol. 118, pp.385-388, 2001.

[72] T. N. D. R. Raju and V. R. Raju, An experimental investigation on surface quality and dimensional accuracy of FDM components, vol. 1, no. 2, 2010.

[73] A. Kumar, R. K. Ohdar, and S. S. Mahapatra, Improving dimensional accuracy of Fused Deposition Modelling processed part using grey Taguchi method, Materials and Design, vol. 30, no. 10, pp.4243-4252, 2009.

[74] P. Gu and L. Li, Fabrication of biomedical prototypes with locally controlled properties using FDM, CIRP Annals, vol.51, no.1, pp.181-184, 2002.

[75] N. Guo and M. C. Leu, Additive manufacturing : technology , applications and research needs, Frontiers of Mechanical Engineering, vol.8, no.3, pp.215–243, 2013.

[76] V. Kyovtorov, I. Georgiev, S. Margenov, D. Stoychev, F. Oliveri, and D. Tarchi, New antenna design approach 3D polymer printing and metallization. experimental test at 1418GHz, AEU - International Journal of Electronics and Communications, vol.73, 2017.

[77] M. D. Auria, S. Member, W. J. Otter, J. Hazell, B. T. W. Gillatt, C. Long-collins, and N. M. Ridler, 3-D Printed Metal-Pipe Rectangular Waveguides,IEEE Transactions on Components, Packaging and Manufacturing Technology, vol.5, 2015.

[78] Y. Xie, S. Ye, C. Reyes, P. Sithikong, B. I. Popa, B. J. Wiley, and S. A.Cummer, Microwave metamaterials made by fused deposition 3D printing of a highly conductive copper-based lament, Applied Physics Letters, vol.110, no.18, 2017.

[79] Y. Arbaoui, P. Agaciak, A. Chevalier, V. Laur, A. Maalouf, J. Ville, P. Roquefort, T. Aubry, and P. Queelec, 3D printed ferromagnetic composites for microwave applications, Journal of Materials Science, vol.52, no.9, pp.4988–4996, 2017.

[80] S. N. A. M. Halidi and J. Abdullah, Moisture effects on the ABS used for Fused Deposition Modeling rapid prototyping machine, 2012 IEEE Symposium on Humanities, Science and Engineering Research, 2012.

[81] C. C. Kuo and R. C. Mao, Development of a Precision Surface Polishing System for Parts Fabricated by Fused Deposition Modeling, Materials and Manufacturing Processes, vol. 31, no. 8, pp.1113-1118, 2016.

[82] Y. Zhang and K. Chou, A parametric study of part distortions in fused deposition modelling using three-dimensional finite element analysis, Proceedings of the Institution of Mechanical Engineers, Part B, Journal of Engineering Manufacture, vol. 222, no. 8, 2008.

[83] D. Qiu and N. A. Langrana, Void eliminating toolpath for extrusion based multimaterial layered manufacturing, Rapid Prototyping Journal, vol. 8, no. 1, pp.38-45, 2002.

[84] M. Liang, X. Yu, C. Shemelya, E. Macdonald, and H. Xin, 3D printed multilayer microstrip line structure with vertical transition toward integrated systems, 2015 IEEE MTT-S International Microwave Symposium, no.l, 2015.

[85] M. Liang, C. Shemelya, E. MacDonald, R. Wicker, and H. Xin, 3-D printed microwave patch antenna via fused deposition method and ultrasonic wire mesh

embedding technique, IEEE Antennas and Wireless Propagation Letters, vol.14, pp.1346 - 1349, 2015.

[86] E. A. Rojas-Nastrucci, T. Weller, V. L. Aida, F. Cai, and J. Papapolymerou, A study on 3D-printed coplanar waveguide with meshed and finite ground planes, 2014 IEEE 15th Annual IEEE Wireless and Microwave Technology Conference, WAMICON 2014, 2014.

[87] S. Zhang, Y. Vardaxoglou, W. Whittow, and R. Mittra, 3D-printed at lens for microwave applications, 2015 Loughborough Antennas and Propagation Conference, 2015.

[88] G. M. Lous, I. a. Cornejo, T. F. McNulty, a. Safari, and S. C. Danfortha, Fabrication of Piezoelectric Ceramic / Polymer Composite Transducers using Fused Deposition of Ceramics, MRS Proceedings, vol.542, 1998.

[89] Antenna Basic Concepts, Pulse Electronics and Larsen Antennas, 2016.

[90] F. Cai, T. Khan, and J. Papapolymerou, Low Loss X-band Filter Using 3D Poly jet Technology, IEEE MTT-S International Microwave Symposium, 2015.

[91] M. Liang, W. R. Ng, K. Chang, K. Gbele, M. E. Gehm, and H. Xin, A 3D luneburg lens antenna fabricated by polymer jetting rapid prototyping, IEEE Transactions on Antennas and Propagation, vol.62, no.4, pp.1799-1807, 2014.

[92] M. I. M. Ghazali, E. Gutierrez, J. C. Myers, A. Kaur, B. Wright, and P. Chahal, Aordable 3D printed microwave antennas, Electronic Components and Technology Conference, 2015.

[93] X. Yan and P. Gu, A review of rapid prototyping technologies and systems, CAD Computer Aided Design, vol.28, no.4, 1996.

[94] Y. Huang, X. Gong, S. Hajela, and W. J. Chappell, Layer-by-layer stereolithography of three-dimensional antennas, IEEE Antennas and Propagation Society, AP-S International Symposium (Digest), vol.1A, 2005.

[95] S. Kumar, M. Hofmann, B. Steinmann, E. J. Foster, and C. Weder, Reinforcement of Stereolithographic Resins for Rapid Prototyping with Cellulose Nanocrystals, ACS Applied Matter Interfaces 2012, vol.4, pp.5399–5407, 2012.

[96] G. A. Brady, T.-m. Chu, and J. W. Halloran, Curing Behavior of Ceramic Resin for Stereolithography, International Solid Freeform Fabrication Symposium, no.1, 1996.

[97] D. Pham and R. Gault, A comparison of rapid prototyping technologies, International Journal of Machine Tools and Manufacture, vol.38, no.10-11, pp.1257-1287, 1998.

Chapter 3

Filament Optimization

This chapter describes the development and optimization of a polymer based filament with a high fraction of high dielectric permittivity filler for FFF 3D printing, including the addition of surfactant and plasticiser. The fabrication method as well as microstructural and dielectric characterization of the bespoke composite filaments are presented. The filament is composed of 32 vol% of ferroelectric barium titanate ($BaTiO_3$) micro-particles in a polymeric acrylonitrile butadiene styrene (ABS) matrix. An ionic organic ester surfactant (octyl gallate) is added during formulation to enhance the compatibility between the polymer and $BaTiO_3$. To promote reproducible and robust printability of the fabricated filament, and to promote plasticity, dibutyl phthalate is additionally used. The combined effect of 1 wt% surfactant and 5 wt% plasticizer results in a uniform, continuous (> 50 m) filament capable of many hours of uninterrupted 3D printing. The success of the optimized filament makes the printing of microwave devices (e.g. quarter wave plate and spiral phase plate) feasible. These printed microwave devices and their performance are described subsequently in Chapters 4 and 5.

3.1 Introduction

Development of 3D printing capability to enable the fabrication of composite and/or multiple material structures with a broad range of electromagnetic properties may provide new possibilities for novel functional structures [1, 2], smart microwave devices, and systems possessing meta-material features [3] utilising the principles of transformation optics. Available techniques for multiple material 3D printing are mostly limited by photo-solidification and extrusion-based approaches where the printing material matrix (usually a thermoplastic polymer or a photoactive resin) is mixed with active particles (e.g. colour dye [4, 5], dielectric [6] and magnetic microparticles [7, 8], carbon nanofibers [9, 10], wood fibers [11], etc.) that bring the desired functionality to the final composite printed component.

In extrusion-based approaches, FFF remains the most mainstream printing technique due to its low cost, flexiblility in changing materials, and open community RepRap [12] society support. Leight *et al.* used a polycaprolactone thermoplastic matrix and magnetite nanoparticles to fabricate feedstock filament (although the volume fraction of magnetite was not reported) for FFF printing and demonstrated a fully 3D-printed flow sensor [13]. A polycaprolactone matrix was also used for fabrication of conductive filament containing carbon black. The loading of carbon black within the polymer matrix was optimised (through tests to observe how the composites performed under extrusion through the printer nozzle) so as to be easily printable by a desktop FFF machine without modification [10] .

Additionally, bespoke composite filaments are also widely used for 3D printing of structured composites. FFF with Cu/ABS and Fe/ABS composites of up to 40 vol% filler has been used to show significant improvements in ABS mechanical and

thermal properties due to the incorporation of metallic fillers [14]. 5 wt% of tungsten-polycarbonate composite was fabricated as an FFF feedstock filament for space-based applications and printed parts showed improvement X-ray radiation shielding [15]. Carbon nanotubes have been used to reinforce thermoplastic polyurethane filaments and to induce electrical conductivity [16–18]. The use of thermotropic liquid crystalline polymer fibrils resulted in the improvement of mechanical strength of polypropylene composite feedstock [19].

Fabrication of highly anisotropic structures with designed anisotropy can be realized. For example, the orientation of magnetized alumina particles in a polymer matrix can be effectively controlled by using a magnetically assisted 3D printing platform [20]. A large anisotropy in thermal conductivity was observed in a 3D-printed 4.3 vol% graphite/ABS composite due to the as-printed alignment of graphite flakes [21]. Duigou *et al.* also showed that wood fibre reinforced filaments could be used to achieve mechanical anisotropy as a function of printing orientation in 3D-printed composite materials [11].

While a very wide range of composite feedstock materials for AM (3D printing) are commercially available, the availability of composite filaments, for example of functional ceramic in a printable polymer matrix for FFF usage is mainly limited by the brittleness of the resulting composite filament as the fraction is increased, which leads to unreliable printing and problems. For example, in [6] the dielectric characterisation of $BaTiO_3$/ABS filaments was presented, but loadings above 70 wt% of $BaTiO_3$ were not investigated as the filament became too brittle to be readily printed, causing snapping during spooling and/or feeding. This maximum loading threshold may be varied depending on the specific inorganic oxides material [3], but is approximately 27 vol% for ferroelectric $BaTiO_3$ microparticles possessing the highest

relative dielectric permittivity $\epsilon_r \sim 500$ [22] at microwave frequencies.

The objective of this chapter is to study and improve the binding mechanism in composite ABS/$BaTiO_3$ and further improve the fabrication route for producing continuous uniform composite filament with relatively high dielectric permittivity (>10).

3.2 Methods

High permittivity filaments were fabricated based on the method described in [6] and shown schematically in Figure 3.1. Commercially supplied acrylonitrile butadiene styrene (ABS MFI-22, Styrolution, Germany) was dissolved in acetone until total dissolution and then 30 vol% of $BaTiO_3$ microparticulate powder (Sigma Aldrich) was added and stirred for 12 hours in pursuit of a uniform dispersion. The suspension was then first spread on a tray in a fume cupboard to dry and then subsequently placed in an oven for 8 h at 70°C to ensure that the acetone had fully evaporated. The dried composite was mechanically blended and extruded (at a temperature in the range 160–180°C) through a desktop single screw extruder (Noztek, London) with a 1.6 mm die orifice to form a continuous filament of approximately 1.75 mm diameter. Various amounts (0.5, 1, 1.5 and 2 wt%) of octyl gallate ($C_{15}H_{22}O_5$) and (5 and 10 wt%) of dibutyl phthalate ($C_{18}H_{22}O_4$) (both Sigma Aldrich) were used as surfactant and plasticiser respectively, and added with the intention of altering the binding and mechanical properties of the $BaTiO_3$/ABS composite after the mixing step, see Table 3.1 for further details.

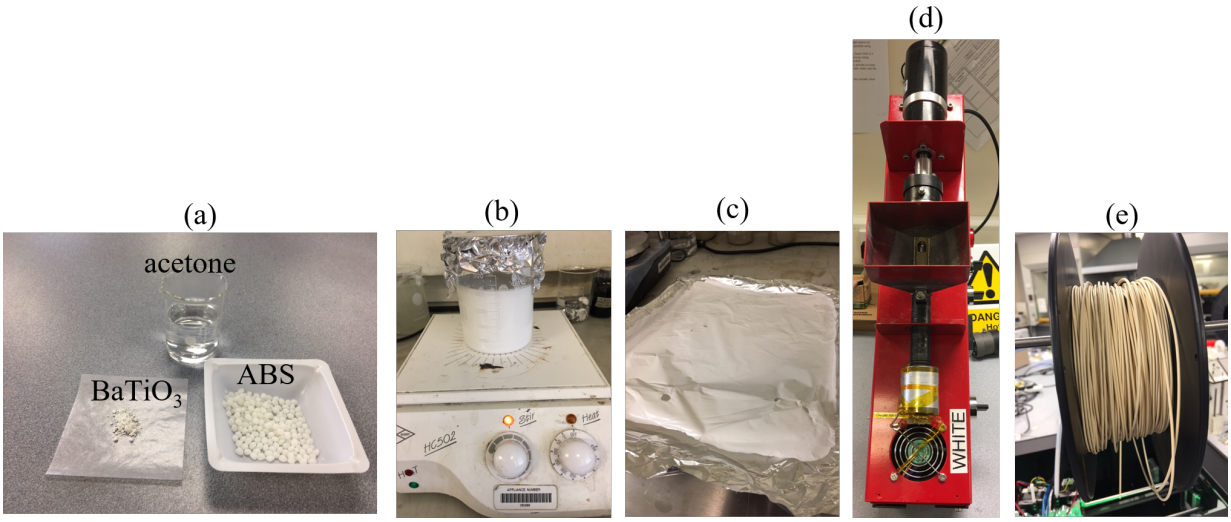


Figure 3.1: Stages of filament fabrication process: (a) $BaTiO_3$ powder, ABS pellets and acetone; (b) mixing and stirring on a stir plate to form a solution; (c) drying of the solution on a tray covered with aluminium foil; (d) single screw extrusion to fabricate the composite filament, and (e) the extruded filament on a spool.

To study the microstructural distribution of the $BaTiO_3$ particles within the polymer matrix, scanning electron microscopy (JEOL JSM-6500F) was performed at 5 kV. Cross-sections for electron microscopy of the filaments and printed coupons were prepared with a rotary microtome diamond blade (Reichert-Jung Ultracut).

To verify the volume fraction of incorporated ceramic particles, thermogravimetric analysis (TGA) was used. The feedstock filament was heated from 40°C to 600°C at a heating rate of 10°C/min, under a flowing air atmosphere using a PerkinElmer TGA. The ABS fraction was fully volatilized at high temperature and the remaining weight fraction of $BaTiO_3$ measured. Differential scanning calorimetry (DSC) of the filament was performed using a PerkinElmer Diamond DSC with alumina as the reference sample, from 0°C to 300°C at a heating/cooling rate of 20°C/min to investigate the effect of the surfactant and plasticiser on any shift in the glass transition temperature of the ABS.

To assess the printability of the optimized filament, surface roughness and filament bending tests were used. Surface roughness was measured by optical microscopy using a μsurf (NanoFocus AG, Germany) digital microscope with X10 lens. High surface roughness could result in printing disruption by blockage at the print head.

Filament bend testing was performed using an in-house designed rig by Prof. D. Isakov as shown in Figure 3.2. The two ends of a 26.5 ± 0.5 cm filament length were clamped in holders free to rotate in the vertical xz plane only. While one holder was fixed at $x = 0$ cm, the other end slid smoothly with a constant velocity of 4.7 cm/s towards this fixed holder, starting from $x = 26$ cm so that the filament was progressively bent in the vertical xz plane. The process was videoed normal to the xz plane to record the filament-curvature at the point of failure. The curvature R was calculated by best-fit of the filament shape immediately prior to failure to an arc shape where the radius of curvature was calculated from $R = [(d/2)^2 + h^2]/2h$, where d is the diameter of the arc, and h is the height from the base to the highest point of the arc.

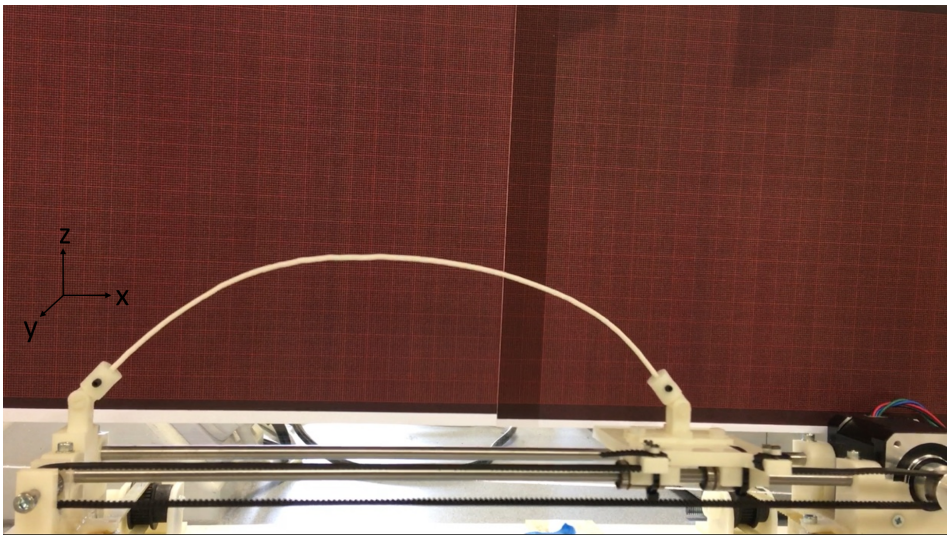


Figure 3.2: In-house built bending test rig. The filament was clamped into two holders with the left one stationary and the right one moving towards the left at constant velocity.

The complex dielectric properties were measured from 3D-printed coupons using a Rohde & Schwarz ZNB20 vector network analyser and split-post dielectric resonator (SPDR, QWED) at 15 GHz and a Ku-band waveguide technique operating from 12 to 18 GHz.

3.3 Results and Discussion

3.3.1 Effect of surfactant

Residual air voids (pores) and agglomerates of $BaTiO_3$ in the extruded ceramic-polymer composite filaments were the most serious defects and severely limited the bend and/or tensile properties due to reduced load carrying capability and stress concentration effects. Therefore the use of a surfactant was investigated to promote interphase/interface chemical compatibility and bonding. This might help to pro-

mote a more uniform dispersion of the two components and to reduce the air voids that otherwise tended to form in and around micro-particle clusters [23]. There are many surfactants available and in general, a certain surfactant can be chosen based on the chemical composition of the polymer matrix and the solid filler. Relatively large organic molecules may reduce agglomeration of treated relatively small particles by steric hindrance effects. The polar units that may be present as side chains can also increase the affinity of the filler particles for the polymer [24]. Surfactant with a very large molecular weight may hinder the dispersion of the ceramics particles because longer chains have lower mobility and become increasingly ineffective at inhibiting agglomeration [23, 25]. Based on the literature, above reasons and informal discussions, octyl gallate (OG)($M_w = 282.33$ g/mol) was chosen as a surfactant, which has four side polar groups: three $-$OH groups to promote interaction with the surface of $BaTiO_3$ and one C=O group to interact with non-polar aliphatic chain in the ABS.

Table 3.1 presents the dielectric characterisation results of FFF 3D-printed $BaTiO_3$/ABS composite samples with various loadings of surfactant in the range of 0–1.5 wt% measured at 15 GHz. Four samples were made for each formulation and three permittivity measurements were taken for each sample. The average measured volume fraction of $BaTiO_3$ was 32.6 vol%, approximately an 8% increase over the nominal fraction of 30 vol%. The higher volume fraction of $BaTiO_3$ of 32.6 vol% than the intended 30 vol% might come from more $BaTiO_3$ micro-particles being bonded with ABS. It could also be a result from slight inaccurate measurement from TGA by considering the ash weight into the $BaTiO_3$ weight after buring. The relative dielectric permittivity increased with increasing surfactant and reached $\epsilon_r = 11.0$ for Sample 3 containing 1 wt% OG. However, further increases in OG fraction reduced

the dielectric constant by 10%, which may be caused by excess surfactant hindering the dispersion of ceramic particles, as suggested by the relatively high extent of inhomogeneity in the composite microstructure.

Table 3.1: Dielectric permittivity of 3D-printed nominal 30 vol% $BaTiO_3$/ABS composites at 15 GHz with various loadings of surfactant, with the actual $BaTiO_3$ fraction obtained by thermogravimetric analysis (TGA).

Sample	Surfactant wt%	Measured $BaTiO_3$ vol%	Permittivity ϵ_r	Loss $\tan\delta \times 10^{-2}$
1	0	33.2	10.68±0.50	3.25±0.4
2	0.5	32.6	10.88±0.35	2.05±0.1
3	1.0	32.4	11.04±0.21	3.03±0.6
4	1.5	32.7	10.08±0.16	3.43±0.1

Figures 3.3(a,b) show low and high magnification micrographs of the $BaTiO_3$/ABS filament cross-sections respectively, taken from a randomly chosen section, without any surfactant. The $BaTiO_3$ micro-scale particles were generally not in intimate contact with the ABS and the filament contained a considerable fraction of micro-pores (Figures 3.3(b,c)) and bubbles up to 200 μm in diameter (Figure 3.3(a)). Additionally, $BaTiO_3$ microparticles frequently formed irregular shaped and pore-containing clusters. Although interfacial debonding may have occurred during sample preparation, the prevalence of apparently debonded particles suggested that interfacial compatibility was generally poor.

Typical SEM images of Samples 2 to 4 (Figures 3.3(d)–(l)) show that the addition of surfactant reduced the air voids, and that $BaTiO_3$ particles were more readily contacted and embedded more uniformly in the ABS, with less clustering. This reduction of voids in the FFF filaments correlated with the increase of permittivity

in the corresponding FFF printed samples in Table 3.1. The exception was Sample 4 with 1.5 wt% OG surfactant where dielectric permittivity was reduced, presumably because there was now an excess of surfactant and the filler/matrix dispersion and/or contact was undermined. Sample 3 with 1 wt% of OG surfactant showed qualitatively the best dispersion and the lowest porosity; it also showed a maximum dielectric permittivity and minimized tangent loss.

The corresponding 3D-printed samples (right-hand column in Figure 3.3) obtained with each of the filaments showed less porosity than the filament cross-sections (middle column in Figure 3.3). During the printing process the filament was heated to 245°C (the molten state) where entrapped small air bubbles were more likely mobile and, together with voids, could be fused together as the composite material was extruded and sheared through the heated nozzle. Nonetheless, the overall trend of printed porosity variation was inherited from the filament, with higher porosity in Sample 1 (Figure 3.3(c)) and Sample 4 (Figure 3.3(l)) and lower porosity in Sample 2 (Figure 3.3(f)) and Sample 3 (Figure 3.3(i)). Overall, the addition of surfactant improved the dispersion and interfacial contact of the $BaTiO_3$, and reduced the tendency for air bubbles and voids.

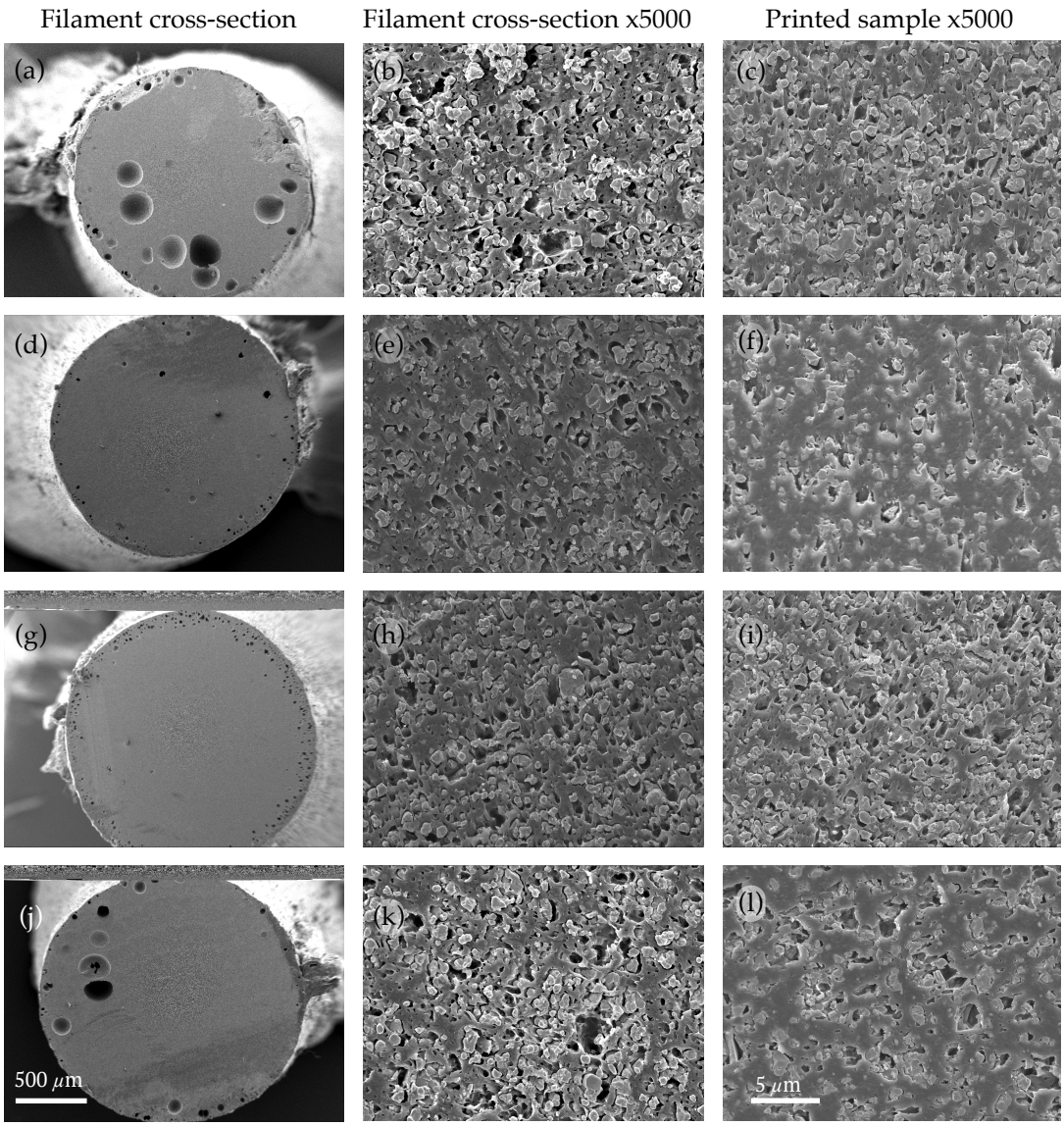


Figure 3.3: Electron micrographs of the cross-section of 30 vol% $BaTiO_3$/ABS filaments (column 1 and 2) and 3D-printed samples using the corresponding filament (right column) (a-c) $BaTiO_3$/ABS with 0 wt% surfactant; (d-f) 0.5 wt% surfactant; (g-i) 1.0 wt% surfactant; and (j-l) 1.5 wt% surfactant.

3.3.2 Effect of plasticiser

Plasticisers modify the properties of polymers, typically increasing elongation to failure and decreasing tensile strength by reducing intermolecular friction between the polymer molecules [26]. When a relatively stiff plastic part is flexed, the polymer molecules move relative to each other either elastically or plastically and the plasticiser acts to lubricate the relative movement of the plastic micellae by reducing their internal resistance to sliding.

To study the effect of plasticiser on morphological, microstructure and dielectric properties of the $BaTiO_3$/ABS composites, two additional Samples 5 and 6 were fabricated, comprising the basic formulation of Sample 3 (30 vol% $BaTiO_3$/ABS with 1 wt% surfactant) together with either 5 wt% or 10 wt% dibutyl phthalate respectively. Dibutyl phthalate was chosen because of its low toxcicity. Figure 3.4 shows the resulting SEM cross-section images of the filaments. The dispersion of the $BaTiO_3$ particles was consistent with that of filament with no plasticiser, and there was no noticeable microstructural effect.

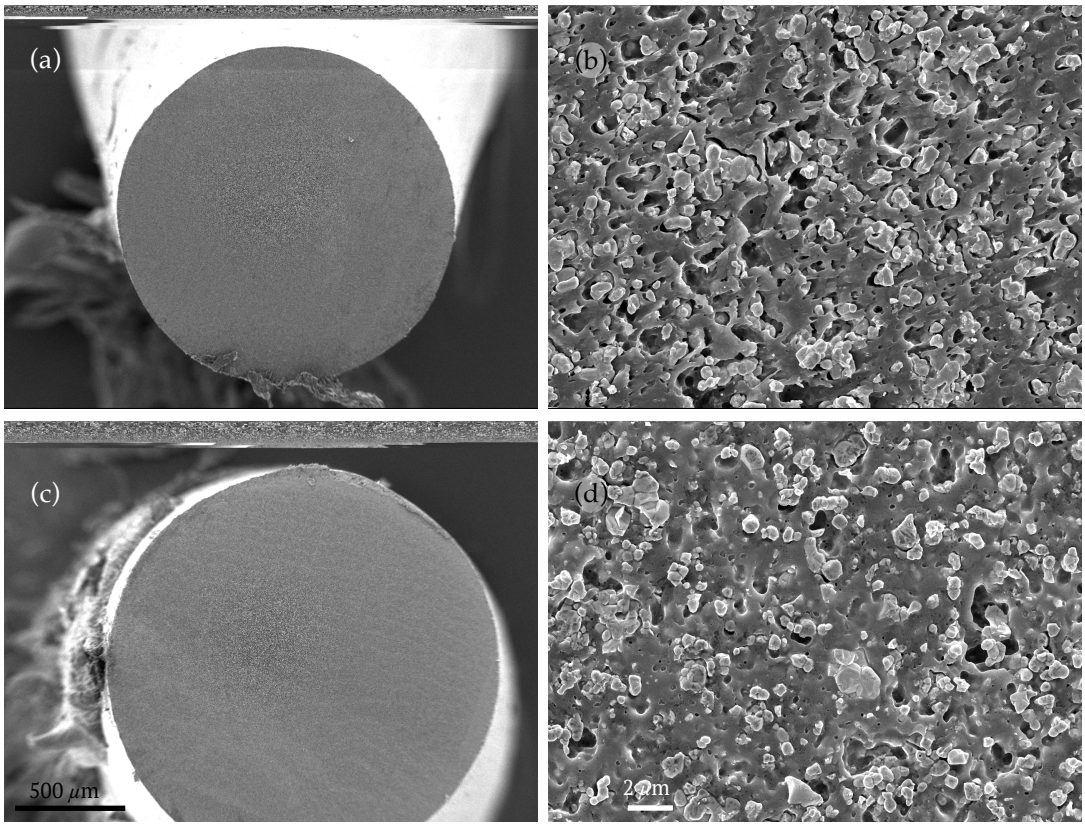


Figure 3.4: Electron micrographs of the cross-section of fabricated filaments (a-b) Sample 5, and (c-d) Sample 6, with 5 and 10 wt% dibutyl phthalate plasticizer respectively.

During extrusion, it was immediately obvious by eye that the addition of plasticiser improved the ceramic-polymer composite flow through the extrusion die [27] and reduced the filament surface roughness. Figure 3.5 shows optical images of the surface of filaments 1 to 5. Filament 1 had the roughest surface with an average roughness $Ra = 4.26$ μm while filament 5 had $Ra = 0.57$ μm; which was similar to the commercial as-supplied ABS. Since all filaments were extruded from the same single screw extruder with the same 1.6 mm diameter nozzle, changes in the surface roughness of the composites were ascribed to the different amounts of filament surfactant and plasticiser. Filament 4 (1.5 %wt surfactant) had a similarly rough

surface as to filament 1 due to the greater agglomeration of $BaTiO_3$ microparticles as previously shown in Figure 3.3(k).

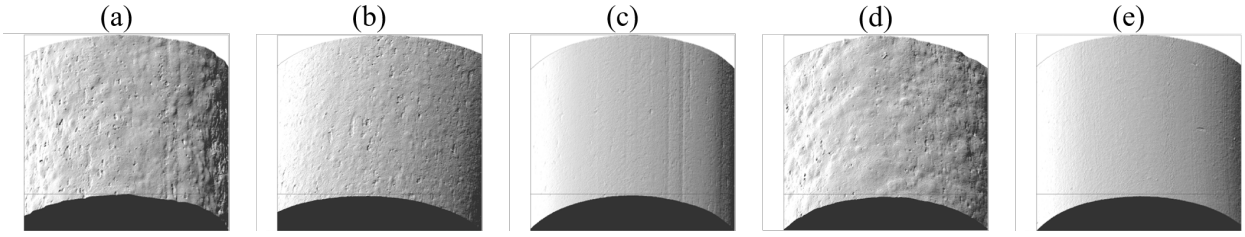


Figure 3.5: Optical images of the surface of the $BaTiO_3$/ABS composite filaments (a) Filament 1 (roughness $Ra = 4.26$ μm); (b) Filament 2 ($Ra = 1.49$ μm); (c) Filament 3 ($Ra = 0.72$ μm); (d) Filament 4 ($Ra = 4.01$ μm), and (e) Filament 5 ($Ra = 0.57$ μm).

The addition of plasticiser also reduced the pressure of the extrusion such that it was possible to increase the extrusion rate to produce a more reliably continuous filament of smaller diameter, with the same pressure and heater head temperature settings. The plasticiser likely decreased the ABS glass transition temperature (T_g) from $T_g = 102$°C in Sample 3 with no plasticiser was shifted to $T_g = 60$°C and $T_g = 20$°C for Samples 5 and 6 respectively, as shown in the differential scanning calorimetry traces in Figure 3.6 from 0°C to 300°C at a heating/cooling rate of 20°C/min. The temperature in the inclined region of the first peak were taken as T_g. Note also that adding the OG surfactant also reduced T_g, suggesting that OG was as intended, relatively soluble in ABS [28].

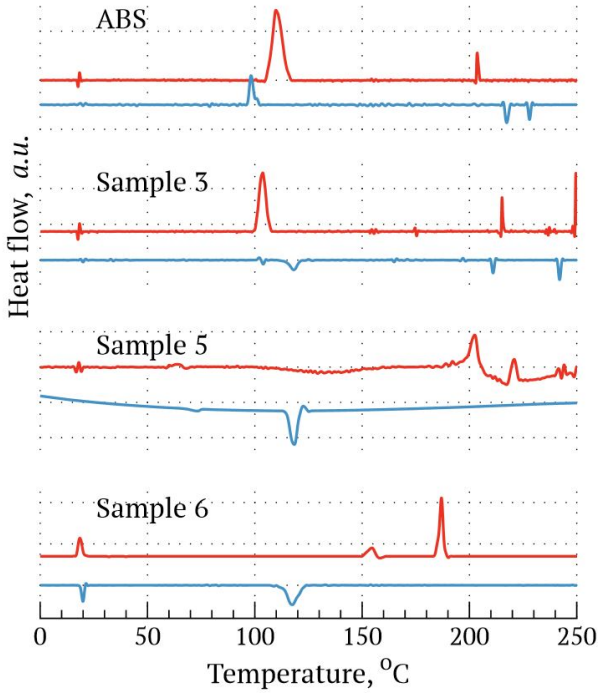


Figure 3.6: Differential scanning calorimetry measurements of heating (red curves) and cooling (blue curves) for ABS filament, Sample 3 (1 wt% surfactant), Sample 5 (1 wt% surfactant, 5 wt% plasticizer) and Sample 6 (1 wt% surfactant, 10 wt% plasticizer).

To show the effect of the various additions on the filament mechanical properties, particularly the ability to be coiled/uncoiled and fed robustly during the 3D printing, Table 3.2 summarizes the travel distance and curvature of all five formulations of filaments at the instant of filament failure. The as-supplied commercial ABS only filament is typically supplied on a spool with a radius of curvature of 4.5 cm and whether the various modified filaments were able to achieve this requirement was assessed. Figure 3.7 shows the best-fit filament arc at fracture, obtained from the videos. Their sequence of increasing failure radius was filament 1, 2, 4 and 3, was in good qualitative agreement with the filament tendency for pores and clustering in the microstructures in Figures 3.3 and 3.4, confirming that reduced air voids

increased filament bend to failure. Filament 5 and standard ABS did not break over the range of travel/curvature in the test. The tendency for bend failure also corresponded to the dielectric permittivities. All the data indicated that filament 5 (32 vol% $BaTiO_3$/ABS with 1 wt% surfactant and 5 wt% plasticiser) had the optimal combination of surfactant and plasticiser of the options studied and could provide useful dielectric properties, excellent mechanical flexibility, and printability. A further increase in plasticiser fraction to 10 wt% produced a too soft filament that was not rigid enough to support itself when placed into the fixtures of the bend test, and which also made it impossible to print.

Table 3.2: Bending filament curvature at fracture.

Filament	Distance Travelled, cm	Curvature, cm
ABS	21	<4.5
1	5.8±0.10	10.8±0.2
2	7.0±0.35	9.7±0.9
3	11±1.5	7.7±2.3
4	9±0.5	8.5±1.4
5	21	<4.5

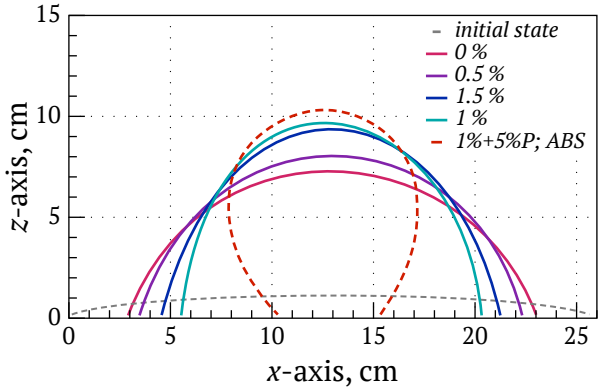


Figure 3.7: Typical bend test behavior of ABS only and $BaTiO_3$/ABS composite filaments. The composite filament composed of 32 vol% $BaTiO_3$/ABS with 1 wt% surfactant and 5 wt% plasticiser (filament 5) showed the same flexibility as ABS only (shown as the dotted line).

The relative dielectric permittivity and loss of 3D-printed coupons using filament 5 were $\epsilon_r = 11 \pm 0.19$ and $\tan\delta = 2.89 \pm 0.12 \times 10^{-2}$ measured at 15 GHz by the SPDR method. The relative dielectric permittivity of coupon 5 was approximately 0.063 lower than coupon 3, however the actual volume fraction f of $BaTiO_3$ was less in coupon 5 (dielectric ratio $\epsilon_r/f = 0.351$ for coupon 5, and $\epsilon_r/f = 0.341$ for coupon 3). Figure 3.8 presents the real part of the relative dielectric permittivity ϵ_r as a function of frequency for 3D-printed coupons using filament 3 (nominal 30 vol% $BaTiO_3$/ABS + 1 wt% surfactant) and filament 5 (same as filament 3 with added 5 wt% plasticiser) measured using a 7.89×15.79 mm^2 rectangular waveguide and the well-known Nicholson-Ross-Weir retrieved method [29]. In the 12–18 GHz frequency range, the coupons exhibited a little dispersion in relative permittivity and average dielectric permittivities of 10.9 and 10.1 were in good agreement with the SPDR measurements. The lower permittivity of coupon 3 through waveguide measuremnt might be associated with the air between the waveguide flange and not perfectly machined sample.

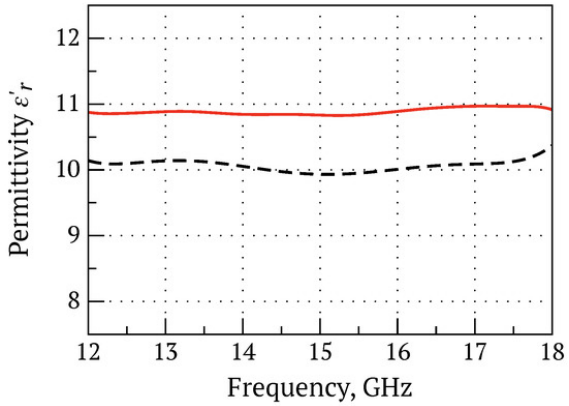


Figure 3.8: Measured real part of the relative dielectric permittivity as a function of frequency for 3D-printed coupons from filament 5 (solid red) and 3 (dashed black).

3.3.3 Demonstration

The 3D-printed sample using the filament comprising ∼32 vol% $BaTiO_3$/ABS composite with 1 wt% surfactant and 5 wt% plasticiser (Sample 5) showed the highest dielectric permittivity of approximately 11 and outstanding flexibility, and a smooth surface.

To demonstrate the printability, several cube-like coupons with different printing precision and fabrication time were produced. Due to the expected lower melting temperature of the filament 5, the print head extruding temperature was decreased by 20°C compared with ABS only (230–245°C). Figure 3.9(a) shows a reconstructed X-ray tomography image of 15 mm side length cube 3D-printed with 0.1 mm layer resolution and 100 % infill using a RepRap FFF 3D printer. As seen from the plane cross-sections in Figure 3.9(b) and (c), the printed internal structure was dense with no resolvable voids or interlayer air gaps/porosity, as is otherwise often found in 3D printed composites [6].

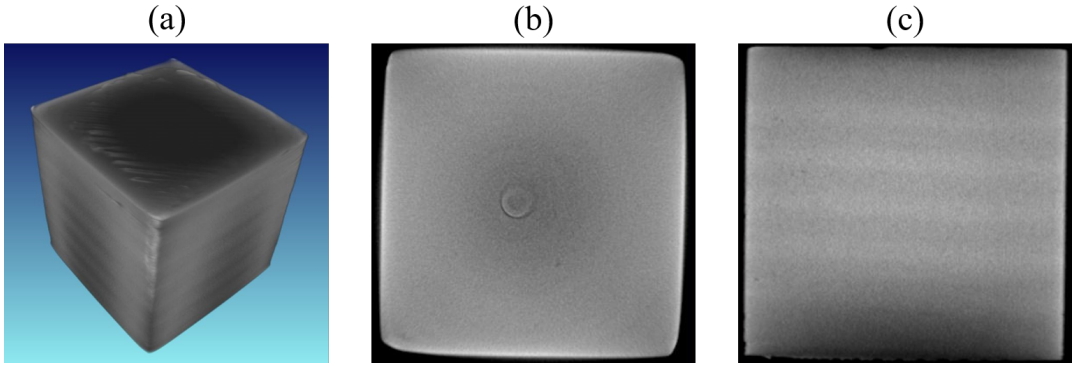


Figure 3.9: X-ray tomography image of the 3D-printed $15 \times 15 \times 15$ mm^3 cube using optimized composite filament 5 (a) Full 3D reconstruction; (b) typical xy-plane slice, and (c) typical xz-plane slice. The images show no resolvable voids or interlayer porosity.

Other examples of more device-like printed structures using filament 5 are shown in Figure 3.10. In each case, the devices are versions of a 3D-printed spiral phase plate, which is an optical device described in more detail in Chapter 5, and consisted of a coupon with an azimuthally dependent thickness that imparts an azimuthal phase shift to incident radiation. This azimuthal phase retardation can be achieved by a continuous variation in thickness, or by a local change in the material's relative dielectric permittivity, and both types are shown. For changes in thickness (i.e. optical length), the total step height was chosen so that the total phase shift around the centre of the phase plate was 2π. The phase plates was printed with 0.2 mm layer thickness and took approximately 3 hours using using commercial MakerBot Desktop software with standard settings.

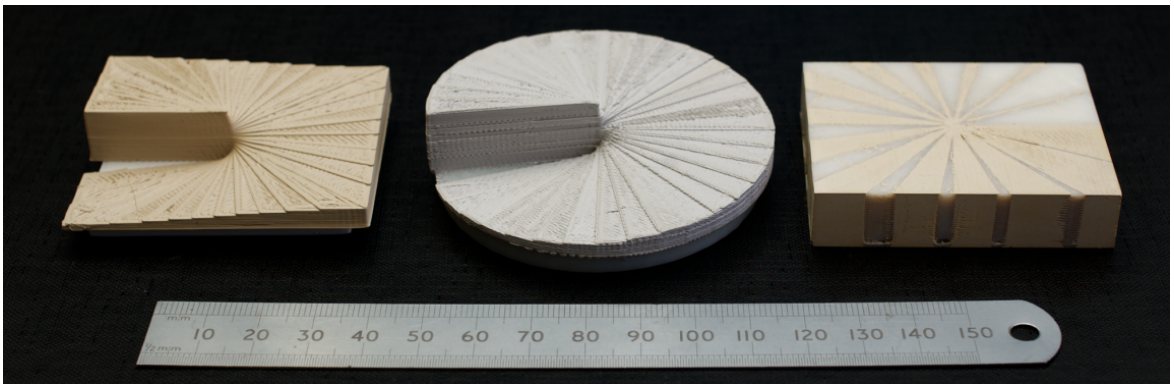


Figure 3.10: Demonstration examples of several 3D-printed microwave devices for generation of orbital angular momentum.

3.4 Conclusions

An optimised formulation of a high relative permittivity, low loss $BaTiO_3$/ABS composite filament for FFF 3D printing has been demonstrated. The filament had a commercial quality surface finish and an effective relative dielectric permittivity $\epsilon_r = 11$ in printed coupons, which was typically 30% to 40% higher than previously reported for a similar composite system. Critical to the performance was the use of a surfactant (1 wt%) and a plasticiser (5 wt%), which facilitated an acceptably uniform micro-particle distribution and reduction of void fraction, and enhanced bend properties. Several 3D-printed structures were fabricated to demonstrate the applicability of the bespoke filament for robust long-time printing without interruption. These types of composites with enhanced and spatially controlled electromagnetic properties may widen the application of 3D printed parts in the radio communication sector, facilitating, for example, direct 3D printing of antennas, microwave horns and compact lenses, some of which are shown in subsequent chapters.

Bibliography

[1] O Quevedo-Teruel, W Tang, R.C. Mitchell-Thomas, A Dyke, H Dyke, L Zhang, S Haq, Y Hao, Transformation optics for antennas: why limit the bandwidth with metamaterials?, Scientific Report, no.3, 1903, 2013.

[2] D Isakov, C.J. Stevens, F. Castles, P.S. Grant, 3D-Printed high dielectric contrast gradient index flat lens for a directive antenna with reduced dimensions, Advanced Materials Technologies,vol.1, 1600072, 2017.

[3] D Isakov, Q Lei, F Castles, C.J. Stevens, C.M.R. Grovenor, P.S. Grant, 3D printed anisotropic dielectric composite with meta-material features, Materials Design, vol.93, pp.423-430, 2016.

[4] A.P. Haring, A.U. Khan, G Liu, B.N. Johnson, 3D printed functionally graded plasmonic constructs, Advanced Optical Matter, vol.5, 1700367, 2017.

[5] B.M. Boyle, T.A. French, R.M. Pearson, B.G. McCarthy, G.M. Miyake, Structural colour for additive manufacturing: 3D-Printed photonic crystals from block copolymers, ACS Nano, vol.11,pp.3052–3058, 2017.

[6] F Castles, D Isakov, A Lui, Q Lei, C.E.J. Dancer, Y Wang, J.M. Janurudin, S.C Speller, C.R.M. Grovenor, P.S. Grant, Microwave dielectric characterisation of 3D-printed $BaTiO_3$/ABS polymer composites, Scientific Report, vol.6, 22714, 2016.

[7] P.S. Grant, F Castles, Q Lei, Y Wang, J.M. Janurudin, D Isakov, S Speller, C Dancer, C.R.M. Grovenor, Manufacture of electrical and magnetic graded

and anisotropic materials for novel manipulations of microwaves, Philosophical Transactions of the Royal Society A, vol.373, 20140353, 2015.

[8] S.J. Leigh, C.P. Purssell, J Bowen, D.A. Hutchins, J.A. Covington, D.R. Billson, A miniature flow sensor fabricated by micro-stereolithography employing a magnetite/acrylic nanocomposite resin, Sensor and Actuators A: Physical, vol.168, pp.66-71, 2011.

[9] J Czyzewski, P Burzyński, K Gawel, J Meisner, Rapid prototyping of electrically conductive components using 3D printing technology, Journal of Materials Processing Technology, vol.209, pp.5281-5285, 2009.

[10] S.J. Leigh, R.J. Bradley, C.P. Purssell, D.R. Billson, D.A. Hutchins, A simple, low-cost conductive composite material for 3D printing of electronic sensors, PLOS ONE, 2012.

[11] A Le Duigou, M Castro, R Bevan, N Martin, 3D printing of wood fibre biocomposites: From mechanical to actuation functionality, Materials Design, vol.96, pp.106-114, 2016.

[12] http://reprap.org.

[13] S.J. Leigh, C.P. Purssell, D.R. Billson, D.A. Hutchins, Using a magnetite/thermoplastic composite in 3D printing of direct replacements for commercially available flow sensors, Smart Materials and Structures, vol.23, 095039, 2014.

[14] M Nikzad, S.H. Masood, I Sbarski, Thermo-mechanical properties of a highly

filled polymeric composites for Fused Deposition Modeling, Materials and Design, vol.3, pp.3448-3456, 2011.

[15] C.M. Shemelya, A Rivera, A.T. Perez, C Rocha, M Liang, X Yu, C Kief, D Alexander, J Stegeman, H Xin, R.B. Wicker, E MacDonald, D.A. Roberson, Mechanical, Electromagnetic, and X-ray Shielding Characterization of a 3D Printable Tungsten–Polycarbonate Polymer Matrix Composite for Space-Based Applications, Journal of Electronic Materials 44, pp.2598–2607, 2015.

[16] W Zhong, F Li, Z Zhang, L Song, Z Li, Short fiber reinforced composites for fused deposition modeling, Materials Science and Engineering A, vol.301, pp.125-130 2001.

[17] F Ning, W Cong, J Qiu, J Wei, S Wang, Additive manufacturing of carbon fiber reinforced thermoplastic composites using fused deposition modeling, Composite Part B:Engineering, vol.80, pp.369-378, 2015.

[18] B Mariappan, S.N. Jaisankar, Properties of polyurethane nanocomposite filaments for conductive textile applications,Journal of Thermoplastic Composite Materials, 30(10), pp.1361-1372, 2017.

[19] R.W. Gray, D.G. Baird, J.H. Bohn, Thermoplastic composites reinforced with long fiber thermotropic liquid crystalline polymers for fused deposition modeling, Polymer Composites, vol.19, pp.383-394, 2004.

[20] D Kokkinis, M Schaffner, A.R. Studart, Multimaterial magnetically assisted 3D printing of composite materials, Nature Communications 6, 8643, 2015.

[21] C Shemelya, A Rosa, A.R. Torrado, K Yue, J Domanowskie, P.J. Bonacusee,

R.E. Martin, M Juhasz, F Hurwitz, R.B. Wicker, B Conner, E MacDonald, D.A. Roberson, Anisotropy of thermal conductivity in 3D printed polymer matrix composites for space based cube satellites, Additive Manufacturing, vol.16, pp.186-196, 2017.

[22] L Curecheriu, S Balmus, M.T. Buscaglia, V Buscaglia, A Ianculescu, L Mitoseriu, Grain size-dependent properties of dense nanocrystalline barium titanate ceramics, Journal of America Ceramic Society, vol.95, pp. 3912-3921, 2012.

[23] T Zhou, J.W. Zha, R.Y. Cui, B.H. Fan, J.K. Yuan, Z.M. Dang, Improving dielectric properties of $BaTiO_3$/ferroelectric polymer composites by employing surface hydroxylated $BaTiO_3$ nanoparticles, ACS Applied Materials Interfaces, vol.3, pp.2184–2188, 2011.

[24] S Ogitani, S.A. Bidstrup-Allen, P.A. Kohl, Factors influencing the permittivity of polymer/ceramic composites for embedded capacitors, IEEE Transactions on Advanced Packaging, vol.23, pp.313-322, 2000.

[25] L Ramajo, M.S. Castro, M.M. Reboredo, Effect of silane as coupling agent on the dielectric properties of $BaTiO_3$-epoxy composites, Composites Part A: Applied Science, vol.38, pp.1852-1859, 2007.

[26] A Kirkpatrick, Some Relations Between Molecular Structure and Plasticizing Effect, Journal of Applied Physics, vol.11, 255, 1940.

[27] B Tylkowski, V Marturano, P Cerruti, V Ambrogi, Polymer additives, Physics Science Review, 2017.

[28] L.A. Wood, Glass transition temperatures of copolymers, Journal of Polymer Science, 1958.

[29] Nicholson A. M., Ross, G. F. Measurement of the intrinsic properties of materials by time-domain techniques, IEEE Transactions on Instrument and Measurement, vol.19, pp.377 - 382, 1970.

Chapter 4

Printed Device Demonstration - Quarter Wave Plate

This chapter describes the manufacturing and analysis of a 3D printed quarter-wave plate ($\lambda/4$, QWP) using the bespoke composite filament described in Chapter 3. A QWP is an optical device that induces a phase retardation of $\pi/2$ between the electric components of an incident EM wave and can convert a linearly polarized wave to a circularly polarized wave or vice-versa. A QWP maybe manufactured from a birefringent materials such as quartz, which has double refraction to form an ordinary refractive index and an extraordinary refractive index [1]. The printed QWP in this thesis however comprises alternating layers or stripes of a printed high permittivity composite (ABS-32 vol% $BaTiO_3$ with $\epsilon_r = 10.8$), and low permittivity commercial acrylonitrile butadiene styrene (ABS with $\epsilon_r = 2.6$). The objective is to demonstrate the potential use of additive manufacturing combined with bespoke filaments to efficiently fabricate optical-like devices for use in the microwave frequency range.

4.1 Introduction

There are three types of polarization: linear, circular and elliptical [2]. To understand these polarisations, the electric field of an electromagnetic wave can be viewed as a combination of two orthogonal components. For example, if the phase difference between the two orthogonal components is 0° or 180°, the wave is defined as linearly polarized, as shown in Figure 4.1(a); if the phase difference is 90° or 270° and both components have the same amplitude, the wave is defined as circularly polarized, shown in Figure 4.1(b); and, if the phase difference is other than those for linearly and circularly polarized wave and/or the amplitudes of the components are not equal, the wave is defined as elliptically polarized, shown in Figure 4.1(c).

The manipulation of the phase distribution of EM waves may allow encoding of transmitted information and control over the propagation and divergence behaviour of the wave. Circular polarization reduces issues with alignment between receiving and transmitting optics in wireless communication systems [3]. A combination of linearly polarized and circularly polarized antennas has been shown to enhance the effective communication range and decrease deviations in the received power [4]. Consequently, such devices for the control of the amplitude, phase and polarization of EM waves are of importance in imaging systems and wireless communications [5].

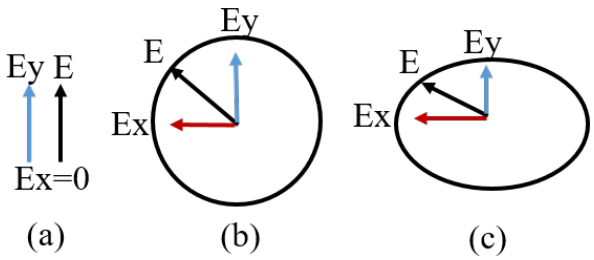


Figure 4.1: Schematic diagram of three types of polarization by resolving the electric field (E) into two orthogonal components Ex and Ey (a) example of a linearly polarized wave when the phase difference is 180°; (b) example of a circularly polarized wave with phase difference of 90 °, and (c) example of an elliptically polarized wave when the phase difference is 90°and the amplitude of Ex and Ey is different.

The phase difference/retardation is produced by light/wave propagating through media with different refractive indexes (n) in different directions. The velocity ($v = c/n$) of waves travelling in such media will be different, and the wave will transform into two components: an ordinary ray along the ordinary axis (O) with high refractive index and an extraordinary ray along the extraordinary axis (E) with low refractive index. However, because natural materials have only limited birefringence (and so produce only weak effects), especially for mm-wave and microwave applications, artificial birefringent materials have had to be developed, for example, using non-symmetric and chiral metamaterial resonators [6–10] to achieve more pronounced effects. Four birefringent GHz metasurfaces designs were proposed to perform operations typical of a $\lambda/2$ plate, a QWP, a beam splitter and provide orbital angular momentum multiplexing [11]. A THz narrow-band linear polarization converter has also been proposed using layered metal grating resonator arrays in a unit cell structure placed between polyimide dielectric spacers [12, 13]. However, these methods suffer from high absorption loss and narrow bandwidth.

Alternatively, all-dielectric, non-resonating polarization converters have also

been investigated. Prototypes for QWP and $\lambda/2$ plates consisting of a two-dimensional array of elliptic-shape dielectric resonators have been demonstrated in the 20–30 GHz microwave band [14]. Dielectric gradient gratings fabricated by lithography and etching have shown to possess high transmission, high artificial birefringence, and polarization conversion in the THz regime [15]. An all-dielectric wide-band polarization converter was fabricated using periodic stacking of rigid foam and polytetrafluoroethylene substrates [16]. Although these examples demonstrated concepts for phase retarder plates and polarisation converters using all dielectric materials, the fabrication methods were inelegant, complicated and probably costly. Here, 3D printing of dual materials ($BaTiO_3$/ABS filament and ABS filament) is used to fabricate an all-dielectric QWP with attractive performance that shows potentially facile extension to many other optical-like devices operating in the microwave regime.

4.2 Methods

The all-dielectric QWP plate design draws on the approach described for a 3D-printed anisotropic dielectric composite possessing Mie-type magnetic resonance [17]. This approach involves 3D-printed mm-scale striped regions of relatively low ϵ_{l} and high ϵ_{h} permittivity, produced by printing a commercial ABS filament and the bespoke $BaTiO_3$/ABS composite filament (see Chapter 3) respectively [18]. The effective dielectric permittivity ϵ_{eff} of an alternating, high-low permittivity striped structure at microwave frequencies varies with respect to the direction of the electric field E carried by an incident microwave and the volumetric fill fraction f of the high dielectric permittivity material ϵ_{h}. The effective permittivity ϵ_{eff} of the structure must lie in the range between the upper (E is parallel to the strips orientation)

and lower (E is perpendicular to the strips) Wiener bounds [19]:

$$\epsilon_{\max} = f\epsilon_{\mathrm{h}} + (1-f)\epsilon_{\mathrm{l}}, \tag{4.1}$$

$$\epsilon_{\min}^{-1} = f\epsilon_{\mathrm{h}}^{-1} + (1-f)\epsilon_{\mathrm{l}}^{-1}, \tag{4.2}$$

Figure 4.2(a) shows the effective relative dielectric permittivity of the upper ($\epsilon_{\max}$) and lower ($\epsilon_{\min}$) Wiener bounds of a two-phase composite with ϵ_{l} and ϵ_{h}, corresponding to the measured values of the ABS and $BaTiO_3$/ABS composite filaments. The complex dielectric permittivity of both materials was characterised at 15 GHz by the split-post resonator method [22] as $\epsilon_{\mathrm{l}} = 2.6$ and $\epsilon_{\mathrm{h}} = 10.8$. The maximum dielectric anisotropy $\Delta\epsilon = \epsilon_{\mathrm{h}} - \epsilon_{\mathrm{l}}$ for a given ϵ_{h} and ϵ_{l} will be achieved at an optimum volume fraction f_0 of ϵ_{h} obtained from the solution of the differential equation $\frac{d\Delta\epsilon}{df} = 0$, and is given by:

$$f_0 = \frac{\sqrt{\epsilon_{\mathrm{h}}\epsilon_{\mathrm{l}}} - \epsilon_{\mathrm{h}}}{\epsilon_{\mathrm{l}} - \epsilon_{\mathrm{h}}}, \tag{4.3}$$

which gives $f_0 = 0.67$ for the materials used here. Equation 4.3 is also shown graphically in Figure 4.2(b). For a structure composed of periodic, alternating stripes with ϵ_{l}=2.6 and ϵ_{h}=10.8 at a filling fraction of $f = 0.67$, the effective dielectric permittivity along the stripes was $\epsilon_{yy} = 8.1$, while the dielectric permittivity orthogonal to the stripes was $\epsilon_{xx} = 5.3$.

The phase retardation $\Delta\phi$ is provided by:

$$\Delta\phi = \phi_y - \phi_x = \frac{2\pi}{\lambda}(\sqrt{\epsilon_{yy}} - \sqrt{\epsilon_{xx}})d, \tag{4.4}$$

where d is the thickness of the dielectric anisotropic plate built up from the alter-

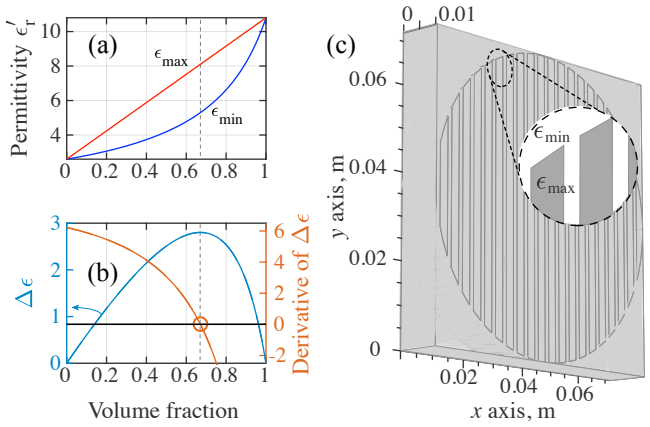


Figure 4.2: The design approach for a microwave QWP. (a) The effective relative dielectric permittivity of the upper ($\epsilon_{\max}$,) and lower ($\epsilon_{\min}$) Wiener bounds as a function of volume fraction f of a two-phase composite with $\epsilon_{\rm l}$=2.65 and $\epsilon_{\rm h}$=10.8 corresponding to ABS and $BaTiO_3$/ABS filaments; (b) the difference between the upper and lower Wiener bounds $\Delta\epsilon = \epsilon_{\max} - \epsilon_{\min}$ and the corresponding derivative $\Delta\epsilon(f)$ that determines the optimum volume fraction f_0, shown as a dashed vertical line, and (c) CAD model of the QWP composed of two materials and designed with regards to the conditions shown in (b) and Equation 4.4.

nating stripes. Given the desired $\Delta\phi = \pi/2$, and λ = 19.9 mm (15 GHz), and by inserting the ϵ_{yy} and ϵ_{xx} from a previous equations, the required thickness of the QWP was estimated as 9.1 mm.

Figure 4.2(c) shows a schematic of a QWP that implements the periodic alternating structure. The final printed QWP had a side length of 72 mm to ensure full coverage of the transmitting horn used in experiments and consisted of 20 discrete stripes of $BaTiO_3$/ABS and ABS. The width of the ABS stripes was 1.2 mm (see Figure 4.3 (a), white stripes) and the width of the stripes of $BaTiO_3$/ABS was 2.4 mm (see Figure 4.3 (a), yellow stripes).

A CAD model of this QWP design was converted into .stl format and sent to a dual-head desktop printer (Makerbot Replicator 2X) for printing. The QWP was printed, shown in Figure 4.3, in a vertical way by standing the plate on its thin

edge to reduce cross-contamination of material during switching between the two filaments.

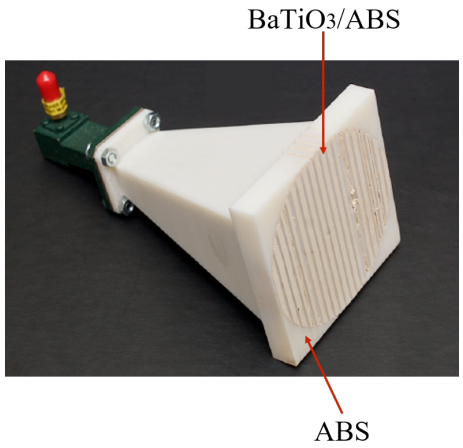


Figure 4.3: Printed QWP with alternating stripes of ABS (white) and $BaTiO_3$/ABS (yellow) attached to a 3D printed pyramidal microwave horn.

A schematic of the working principles of the printed QWP is shown in Figure 4.4, which shows the linear E field transforms into Ex and Ey of equal amplitude upon entering the QWP, with a 45° rotation.

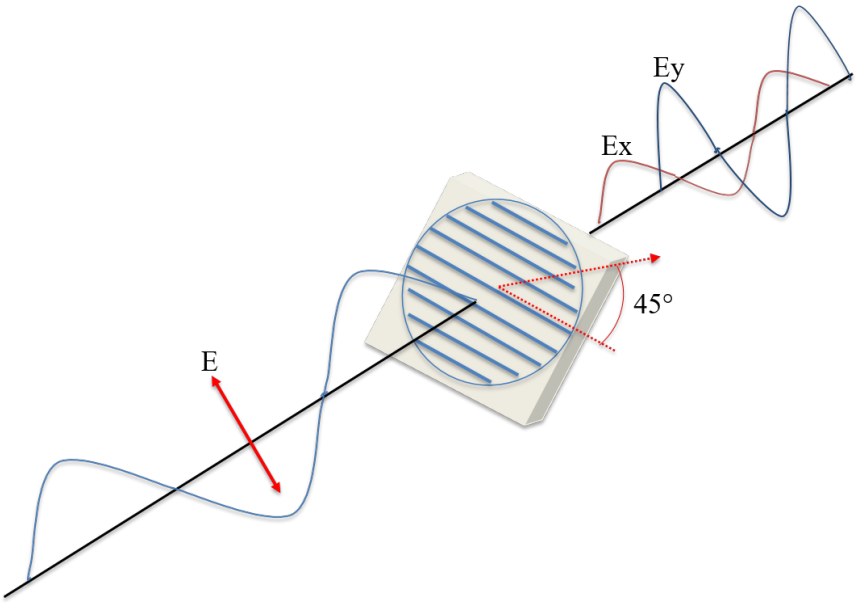


Figure 4.4: Schematic diagram showing how a linearly polarized wave with a linear E field enters the QWP placed at a 45° rotation, resulting in a circularly polarized wave with E field transformed into Ex and Ey components of equal amplitude.

4.3 Results and Discussion

4.3.1 Polarization analysis

Figure 4.5 shows simulation results obtained from software COMSOL Multiphysics for a pyramidal horn and a QWP plate inserted in the front of the horn aperture, performed by collaborator Prof. D. Isakov. Figures 4.5(a) and (b) show the near-field orthogonal components of the electric field as a function of propagation distance z for the anisotropic dielectric plate defined ($\epsilon_{xx} = \epsilon_{\min} = 5.3$, and $\epsilon_{yy} = \epsilon_{\max} = 8.1$) and oriented with its slow axis ($\epsilon_{\max}$) along the polarization of the radiated wave, and then with the same QWP then rotated by 45°, respectively. At 0° orientation in Figure 4.5(a), the QWP plate did not change the relative magnitude of

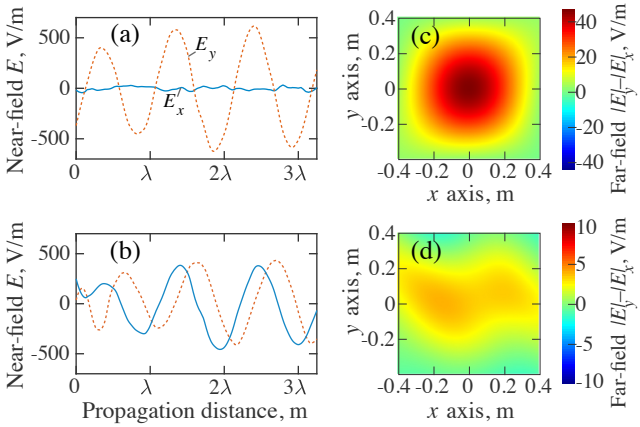


Figure 4.5: (a) Simulated near-field x and y components of the electric field E in the direction of radiation for pyramidal horn with E oriented along y-axis and QWP with its "slow" axis also parallel to y; (b) The same components after the rotation of the QWP at 45° to the polarization of the horn antenna; (c) Projection of the far-field $E_y - E_x$ difference on a plane 0.8×0.8 m^2 at a distance of 100λ from the horn aperture with the QWP oriented with its "slow" axis parallel to the radiation polarisation E_y, and (d) oriented at 45°. Note that the intensity contours in the colour legend have different scales.

the electric field vector, i.e. the polarization. In contrast, a 45° rotation of the QWP (Figure 4.5(b)) resulted in two non-zero components of the E-field polarization with equal amplitude and a $\pi/2$ relative phase shift, corresponding to circular polarization. Figures 4.5(c) and (d) show a 2D map of the amplitude difference $|E_y^{\text{far}} - E_x^{\text{far}}|$ at a distance of 100λ from the horn (far-field), for 0 and 45° orientations of the QWP plate, respectively. On rotation of the QWP to 45°, $E_y^{\text{far}} - E_x^{\text{far}}$ reduced to ≈ 0 (Figure 4.5(d)), indicating equal amplitude in the non-zero components of the E-field polarization (E_y and E_x).

Based on these simulated proof-of-concept results, a QWP plate was fabricated by dual-head FFF 3D printing technique using an approach previously described by the group for a graded index microwave lens [21] using the $BaTiO_3$/ABS composite as the high-permittivity filament and commercial ABS as the low permittivity filament.

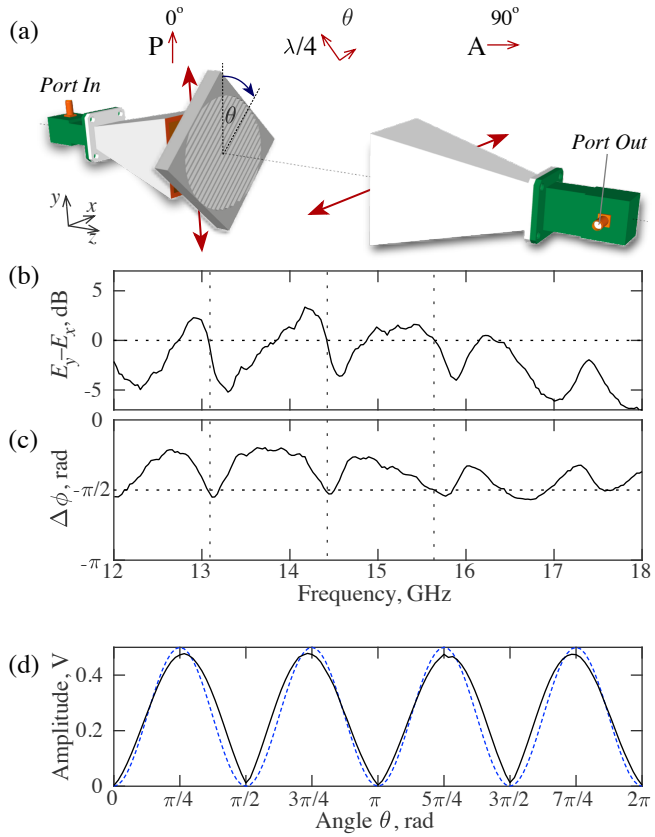


Figure 4.6: (a) Schematic of the experimental setup showing two pyramidal horns and the QWP; (b) Measured power gain difference and phase difference; (c) between transmitted E_y (P$\|$A) and E_x (P$\perp$A) components with QWP oriented at 45° to the principal axes, and (d) Measured transmittance (T) (solid black curve) as a function of the QWP rotation (θ) between two ports oriented perpendicularly to each other (P$\perp$A).

The performance of the 3D-printed QWP was assessed experimentally using the arrangement shown in Figure 4.6(a). Note that the distance between the two horns is not true to scale. A vector network analyser (VNA) (Rhodes& Schwartz, ZNB20) was used to energize microwave input to the transmission horn and to receive the microwave output signal from the receiving horn in the range 12 to 18 GHz. The QWP plate was placed between the two rectangular flange pyramidal horns referred hereafter as a polariser (P, transmitted horn) and analyser (A, receiver horn), by analogy with visual optics, facing each other at about 25λ separation. The horns had length 4.4λ and an aperture of $3.15\lambda \times 2.45\lambda$ radiating in TM_{01} mode with vertical polarization, and with a theoretical directivity of 18 dBi at 15 GHz [20].

The two orthogonal components E_y and E_x of the transmitted signal were analysed separately, at relative orientation of the A horn to the P horn of either 0° or 90° along the transmission direction and with the interposed QWP plate fixed at 45°, i.e. P0-QWP45-A0 and P0-QWP45-A90 conditions, respectively. Figure 4.6(b) shows the difference E_y-E_x between these two conditions while Figure 4.6(c) shows the phase difference $\Delta\phi = \phi_y - \phi_x$ obtained at the two orientations.

As described above, a circularly polarized wave must follow two conditions: $|E_x| = |E_y|$ and a phase difference $\pm(\frac{1}{2} + 2n)\pi$ $(n = 0, 1, 2, \dots)$. Although the QWP was designed for 15 GHz, the experimental data from Figures 4.6(b) and (c) show that these conditions were best realised at 13.1 GHz, 14.4 GHz, 15.7 GHz, and 16.35 GHz. The negative sign of $\Delta\phi$ in Figure 4.6(c) was indicative of left-handed circular polarization. The non-zero power gain difference E_y-E_x in Figure 4.6(b) suggested some slight elliptical character of the E-field polarization in the 12–18 GHz frequency range.

Figure 4.6(d) presents the transmitted wave amplitude (T) as a function of ro-

tation angle Θ of the QWP inserted between P and A horns fixed at 90° relative rotation (see Figure 4.6(a)), measured at 15.7 GHz. The solid curve represents the experimental measurements and the dashed curve represents the theoretical values. A good fit of experimental measurements to theoretical values is achieved. Theoretical value of the transmitted wave amplitude for a QWP is $T = \frac{1}{2}\sin^2(2\theta)$ [23]. The small deviations were attributed to non-ideal alignment of the QWP with respect to the propagation direction, possible printing defects, and radiation losses.

4.4 Conclusions

A 3D printed all dielectric QWP was fabricated in a single manufacturing operation. The QWP provided polarization conversion through a simple design comprising parallel strips of polymer and composite materials with alternating high-low dielectric permittivity resulting in an artificial effective dielectric anisotropy $\Delta\epsilon = 2.9$. The QWP exhibited broadband capability at frequencies other than designed frequency of ~ 15 GHz. This multi-material additive manufacturing method suggests wider applicability to other optical devices that work in the GHz frequency range, which is explored further in the next chapter.

Bibliography

[1] M. Born and E. Wolf, Principles of Optics: Electromagnetic Theory of Propagation, Interference and Diffraction of Light, 6th Ed. Cambridge Univ. Press, 1993.

[2] D. Halliday, and R. Resnick, Fundamentals of Physics. 9th Ed. John Wiley & Sons, Inc., 2011.

[3] F. Yildirim, A. S. Sadri and H. Liu, Polarization effects for indoor wireless communications at 60 GHz, IEEE Communications Letters, vol 12, no.9, pp.660-662, 2008.

[4] Z. Szalay and L. Nagy, Utilization of linearly and circularly polarized antennas for indoor positioning, 17th International Conference on Transparent Optical Networks (ICTON), pp. 1-4, 2015.

[5] N. J. G. Fonseca and C. Mangenot, High-performance electrically thin dual-band polarizing reflective surface for broadband satellite applications, IEEE Transactions on Antennas Propagation, vol 64 no.2, pp.640-649, 2016.

[6] J. Hao, Y. Yuan, L. Ran, T. Jiang, J. A. Kong, C. T. Chan, and L. Zhou, Manipulating electromagnetic wave polarizations by anisotropic metamaterials, Physics Review Letters, vol.99 , 063908, 2007.

[7] Z. Wei,Y. Cao, Y. Fan, X. Yu, and H. Li,Broadband polarization transformation via enhanced asymmetric transmission through arrays of twisted complementary split-ring resonators, Applied Physics Letters, vol.99, 221907, 2011.

[8] J. Y. Chin, J. N. Gollub, J. J. Mock, R. Liu, C. Harrison, D. R. Smith, and T. J. Cui, An efficient broadband metamaterial wave retarder, Optics Express, vol.17, pp. 7640-7647, 2009.

[9] X. Huang, D. Yang, and H. Yang, Multiple-band reflective polarization converter using U-shaped metamaterial, Journal of Applied Physics, vol.115, 103505, 2014.

[10] H. Shi, A. Zhang, S. Zheng, J. Li, and Y. Jiang, Dual-band polarization angle independent 90°polarization rotator using twisted electric-field-coupled resonators, Applied Physics Letters, vol.104, 034102, 2014.

[11] K. Achouri, G. Lavigne, and C. Caloz, Comparison of two synthesis methods for birefringent metasurfaces, Journal of Applied Physics, vol.120, 235305, 2016.

[12] N. K. Grady, J. E. Heyes, D. R. Chowdhury, and Y. Zeng, Terahertz metamaterials for linear polarization conversion and anomalous refraction, Science, vol.340, pp. 1304-1307, 2013.

[13] W. Mo, X. Wei, K. Wang, Y. Li, and J. Liu, Ultrathin flexible terahertz polarization converter based on metasurfaces, Optics Express, vol.24, pp. 13621-13627 2016.

[14] A. Yahyaoui, H. Rmili, K. Achouri, M. Sheikh, A. Dobaie, A. Affandi, and T. Aguili, Transmission Control of Electromagnetic Waves by Using Quarter-Wave Plate and Half-Wave Plate All-Dielectric Metasurfaces Based on Elliptic Dielectric Resonators, International Journal of Antennas and Propagation, 2017.

[15] M. Chen, F. Fan, S.-T. Xu, and S.-J. Chang, Artificial high birefringence in all-dielectric gradient grating for broadband terahertz waves, Scientific Report 6, 38562, 2016.

[16] M. Lorente-Crespo, G. C. Ballesteros, G. Goussetis, and C. Mateo-Segura, Experimental Validation of All-Dielectric mm-Wave Polarization Conversion Based on Form Birefringence, IEEE Microwave Wireless Components Letters, vol.26, no. 10, pp. 759-761, 2016.

[17] D.V. Isakov, Q. Lei, F. Castles, C.J. Stevens, C.R.M. Grovenor, and P.S. Grant, 3D printed anisotropic dielectric composite with meta-material features, Materials and Design, vol.93, pp.423-430, 2016.

[18] F. Castles, D. Isakov, A. Lui, Q. Lei, C.E.J. Dancer, Y. Wang, J.M. Janurudin, S.C. Speller, C.R.M. Grovenor, and P.S. Grant, Microwave dielectric characterisation of 3D-printed BaTiO3/ABS polymer composites, Scientific Report, vol.6, 22714, 2016.

[19] D.E. Aspnes, Bounds on allowed values of the effective dielectric function of two-component composites at finite frequencies, Physics Review B Condensed Matter, vol.25, 1982.

[20] C.A. Balanis, Antenna Theory: Analysis and Design, John Wiley & Sons, Inc., 1997.

[21] D. Isakov, C.J. Stevens, F. Castles, and P.S. Grant, 3D-Printed High Dielectric Contrast Gradient Index Flat Lens for a Directive Antenna with Reduced Dimensions Advanced Materials Technology, vol.1, 1600072, 2016.

[22] J. Krupka, Developments in techniques to measure dielectric properties of low-loss materials at frequencies of 1–50 GHz, Journal of European Ceramic Society, vol.23, pp.2607-2610, 2003.

[23] A. Yariv, Optical Electronics, 4th Ed. Saunders College Publishing, 1991.

Chapter 5

Printed Device Demonstration - Spiral Phase Plate

This chapter describes the design, manufacturing and analysis of 3D printed spiral phase plates (SPPs) as a further demonstration to show the versatility of utilizing AM to manufacture official devices that operate in the microwave frequency range. SPP is an optical device that transforms a plane EM wave (mode number 0) to a Laguerre-Gaussian (LG) beam, which carries orbital angular momentum (OAM) with a non-zero mode number. The characteristics for waves carrying OAM are a helical phase front, and a doughnut-like amplitude profile with a null in the center [1, 2]. Three SPP designs with modes $l = \pm 1$, and one SPP design with modes $l = \pm 2$ were manufactured using fused filament fabrication (FFF) and stereolithography (SLA). All the printed SPPs were characterized by assessing their ability to change an incoming plane EM wave into a helical twisted wave carrying OAM in the frequency range 12 to 18 GHz. A dielectric confocal lens was printed using SLA and used to collimate the OAM wave. Multiplexing and demultiplexing was also demonstrated

experimentally using both two opposite mode and two same mode SPPs of $l = \pm 1$.

5.1 Introduction

The characteristic of waves carrying OAM is that coaxial OAM waves are mutually orthogonal to each other and therefore minimise the possibility of inter-mode crosstalk. The use of multiple OAM waves simultaneously can significantly increase the date transfer capacity of a data transmission system [3–5], including in high-capacity wireless communication lines [6, 7].

The helical or azimuthal phase of an OAM wave is expressed by $\exp(il\phi)$, where l is the mode number and ϕ is the azimuthal angle [1, 8]. The $\pm$ of l indicates the orientation of the helical phase (e.g. clockwise or counter-clockwise). To create this helical phase, an OAM wave can be obtained using a spatial light modulator or forked diffraction grating to generate an interference pattern hologram that converts a plane wave into a wave with predefined phase and amplitude structure [1]. In the microwave frequency range, phased array antennas are the most commonly used method to create OAM, where antennas arrays (typically short dipoles or patches) are arranged around the circumference of a circle and triggered by high frequency electronics to produce an integral signal with an incremental azimuthal phase shift around the array elements [3, 9]. Metasurfaces (composed of sub-wavelength dipole or periodic arrays with specifically predefined shapes, orientation and location) have also been used for the transformation of a plane wave into an OAM wave, including concentrically arranged plasmonic nano-apertures [10], cross-dipole elements [11, 12], and split square resonators [13, 14]. These methods suffer from demanding and complex manufacturing processes.

An OAM wave can also be induced by a dielectric SPP, which is a very simple optical device, where the thickness (or the refractive index) of the SPP simply increases in a spiral pattern in order to generate the azimuthally phase delay gradient. For example, a section of plate-shaped polypropylene ($\epsilon = 2.25$) was milled and assembled to make a step SPP with mode 10 [15]. Alternatively, a PCB board was drilled with holes to make a flat SPP but using varying hole diameter and hole density to achieve an azimuthal gradient change in local refractive index [16]. In contrast to a meta-surface or a phased array antenna, all dielectric SPPs can produce OAM waves with any polarisation. However, for generation of higher mode OAM waves ($l > 1$), the manufacturing method can be laborious and require multiple step assembly. A comparison of some common methods to generate OAM are listed in Table 5.1.

Table 5.1: Methods to generate OAM.

Method	Mode	Scan Area (mm^2)	Frequency (GHz)
Antenna [17]	1, 3	$900 * 900$	8-12
Metasurface [18]	1	$300 * 300$	50-75
Step SPP [19]	1	NA	5.8
Step SPP [15]	10	$500 * 500$	100
Planar SPP [16]	1, 2, 4	$200 * 200$	94

Here, AM techniques were used to fabricate SPPs with mode $l = \pm 1$ and $l = \pm 2$, with the additional benefit of easy conversion between the modes because by reversing the azimuthal gradient of printed SPPs designs, the mode could be converted simply to the opposite sign (e.g. from mode 1 to mode -1). Different designs (flat SPP and step SPP) and materials (composite filament and resin) were printed. There

were three mode 1 SPPs designs: a SPP with steady increase in thickness printed in acrylic resin by SLA; a step SPP with a stair-case of thickness steps, printed from $BaTiO_3$/ABS composite filament by FFF; and a flat SPP, printed by FFF using two filaments ($BaTiO_3$/ABS and ABS) in which the local volume fraction of each material varied with azimuthal position, to achieve an azimuthally varying local permittivity (and therefore refractive index). Two mode 2 SPPs with stair-case designs were also printed by FFF using the $BaTiO_3$/ABS filament. The multiplexing and de-multiplexing ability of the SPPs was demonstrated using two mode +1 SPP and one mode +1 SPP and a mode -1 SPP.

5.2 Methods

The continuously varying thickness SPP with azimuthally increasing height was fabricated using a PolyJet 3D printer (J750 Stratasys) using commercial acrylic photopolymer (VeroClear, Stratasys), printed by collaborator, Prof. D. Isakov. The staircase SPP with mode 1 was printed using a dual-head extrusion desktop 3D printer (Makerbot 2X) with composite dielectric filament $BaTiO_3$/ABS ($\epsilon_r \sim$10.8). The flat SPP with azimuthally changing gradient refractive index was printed with the same desktop printer with ABS and $BaTiO_3$/ABS filaments, similar to the approach used for the QWP in the previous Chapter. The two mode 2 staircase SPPs were printed in the same way as the mode 1 staircase SPP. A dielectric bi-convex lens used to collimate the OAM wave was designed and manufactured using the J750 MultiJet 3D printer with photocurable resin ($\epsilon_r \sim$3), shown in Figure 5.1. The lens was 90 mm in diameter and had a focal length of 110 mm.

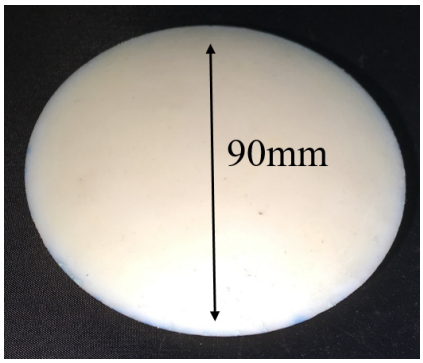


Figure 5.1: Photo of the 90 mm diameter, 10 mm thick (maximum) 3D printed dielectric lens.

The phase and amplitude of microwaves that had passed through the SPPs was measured using the set-up shown in Figure 5.2(a). Two printed rectangular horns with nominal high directivity of 18 dBi at 15 GHz [20] were connected to waveguide adaptors (Flann Microwave). The waveguide was connected to a Vector Network Analyzer (VNA, Rhode&Schwarz ZNB20) through Ku-band SMA coaxial cables. The VNA was used to excite microwaves in the frequency range from 12 GHz to 18 GHz. The separation distance between the two horns was 70 cm ($\sim$35λ). The SPP was attached to the transmitting horn, perpendicular to the xy-plane (wave propagating in the z direction) and kept stationary. The receiving horn moved in the xy-plane with a scan area of 700 mm by 700 mm with a step size of 5 mm. A XY-gantry system (X-Carve) was used for the movement of the receiver in a pre-programmed pattern. The complex scattering parameters (S_{11}, S_{12}, S_{21}, S_{22}), along with the coordinate information from the position of the receiver was used to map the phase and amplitude profile produced by the printed SPPs. The set-up for the investigation of the collimation effects due to the insertion of the printed lens involved placing the lens at the exit of the transmitting horn at the lens's focal length.

Figure 5.2(b) show schematically the arrangement for investigating the SPPs

for multiplexing and demultiplexing. Two transmitting horns were perpendicularly oriented with two SPPs (not shown) attached to them. At the geometrical crossing point of the horn axes, a Al_2O_3 thin square plate of area 100 cm^2 and thickness 2 mm was placed to act as a microwave half-mirror. The mirror was rotated to $\pi/4$ along its vertical axis with respect to both horn directions. With accurate alignment of all elements (centers of the rectangular horns, and the SPPs), both transmitted and reflected OAM waves should be collinear. The waves detected at the receiving horn would be the summation of the OAM modes from the two SPPs from the transmitting horns. For example, to obtain a summation of the OAM modes of +2, the SPPs with $l = +1$ and $l = -1$ must be used for the transmitting side, noting that the -1 mode SPP will be converted to +1 mode due to the phase change caused by the half mirror.

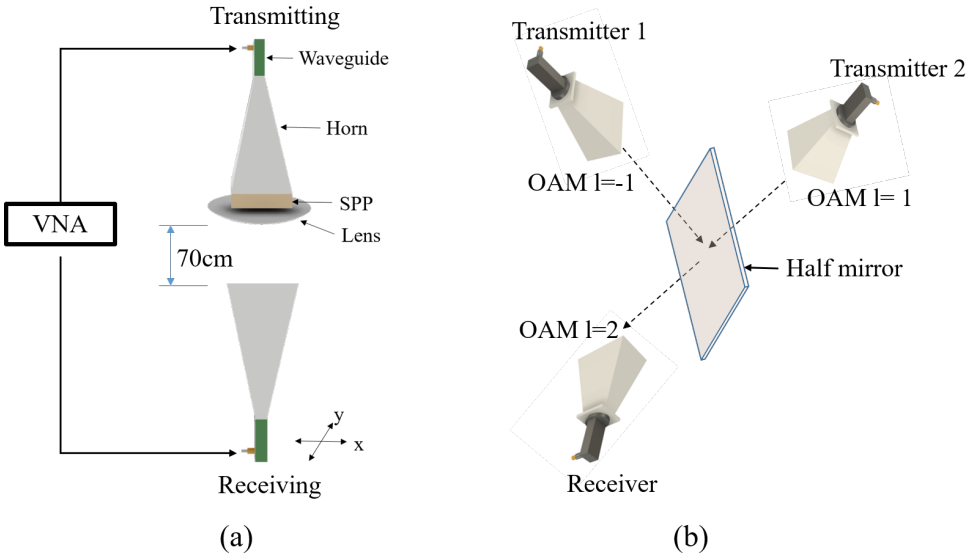


Figure 5.2: (a) Schematic of the experimental set-up for the characterization of phase and amplitude for SPPs, and (b) schematic of the experimental set-up for multiplexing and demultiplexing.

5.3 Results and Discussion

5.3.1 Spiral phase plate design and fabrication

Figure 5.3 shows the three mode 1 SPPs. From left to right are the staircase SPP, the flat SPP, and the varying thickness SPP. The staircase SPP had a thickness (t) of 8.6 mm from $l = \frac{t\Delta n}{\lambda}$, where Δn is refractive index difference between the composite filament (ϵ_r ~10.8) and the media (air $\epsilon_r = 1$), λ is the wavelength (designed at 15 GHz), l is the mode number. The step height of each discrete step in the SPP was given by $h_s = \frac{\lambda}{(n-1)}\frac{\alpha}{2\pi}$, where α is the incremental azimuthal angle of the step (10°). The step height was calculated as $h_s = 0.24\ mm$. To partially compensate for the reflection loss caused by the large difference in refractive index, the SPP was printed on an ABS index matching layer [21]. The varying thickness SPP, printed from resin (ϵ_r ~3) with continuous azimuthal height increase, shown in Figure 5.3 (right) had a maximum thickness of 27.3 mm.

The flat SPP comprised a gradient index design where the azimuthal variation of the optical path was changed by means of changes in the local refractive index rather than by thickness. The flat plate was split into 14 wedge-like segments that were small enough to allow a fine-scale distribution of effective permittivity while still being printable (further increase in the number of segments would result in failure from the printing of the central part of the flat SPP). Each segment was composed of two parts comprising high and low dielectric permittivity materials ($BaTiO_3$/ABS - yellow color and ABS - white color respectively) as shown in Figure 5.3 (middle). The effective local permittivity was determined by averaging over the local area of high and low permittivity. Keeping the thickness of the plate constant at $\lambda/\Delta n = 11.84$ mm, the area ratio of the high and low permittivity was changed

with azimuthal rotation to produce a distribution of refractive index such that the maximum generated phase delay for a wave at 15 GHz was 2π radians.

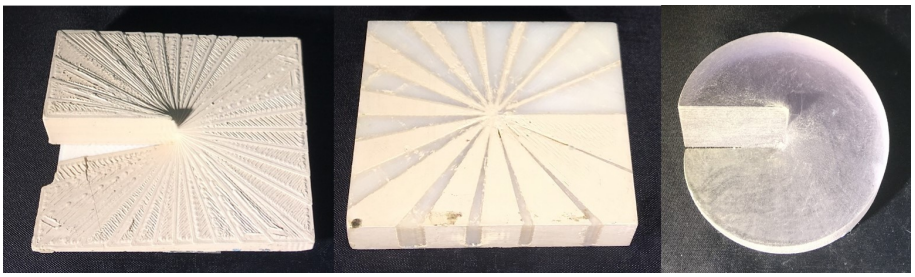


Figure 5.3: Photographs of the 3D-printed SPPs from left to right: SPP with staircase structure, flat SPP with gradient refractive index and a SPP of varying thickness.

Two mode 2 staircase SPPs shown in Figure 5.4 were printed using the same $BaTiO_3$/ABS filament ($\epsilon_r \sim 10.8$) and with a maximum thickness of 17.6 mm, which was twice the height of the staircase SPP with mode 1. The step height of each step within the SPP was 0.97 mm for every 10° azimuthal increment, until the azimuthal angle reached 180°. The thickness was then reduced back to 0.97 mm and then increased for a further 180° (2π radians in total).

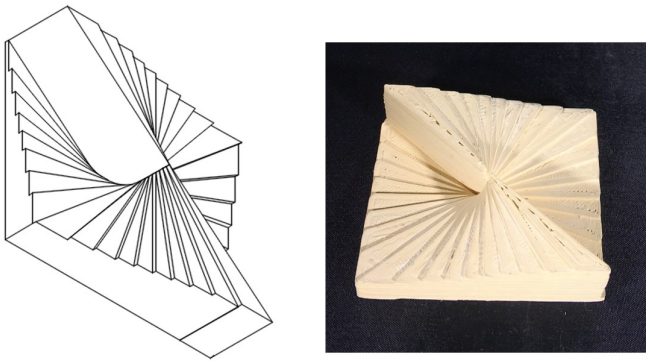


Figure 5.4: (a)The CAD models, and (b) a photograph of the mode $l = +2$ 3D-printed dielectric spiral phase plate.

In principle, a wide range of SPPs could be printed offering significant flexibility in design and manufacturing. The rectangular shaped SPPs printed had side lengths of 43 mm by 54 mm to ensure the exit aperture of the radiation horn was fully covered to prevent any leakage of the microwaves. The varying thickness SPP had a diameter of 110 mm which also satisfied this requirement.

X-ray tomography was used to evaluate the print quality of the step SPP and flat SPP of mode 1, and the reconstructed images of the plane cross-sections (see Figure 5.5) showed that there were no large internal pores in the staircase SPP and the flat SPP. However, small voids formed towards the center of the staircase SPP due to a narrower print path at the center compared with the edges. Voids will lower the effective permittivity and may cause a slight shift in the null center and the phase profile of the propagated OAM wave.

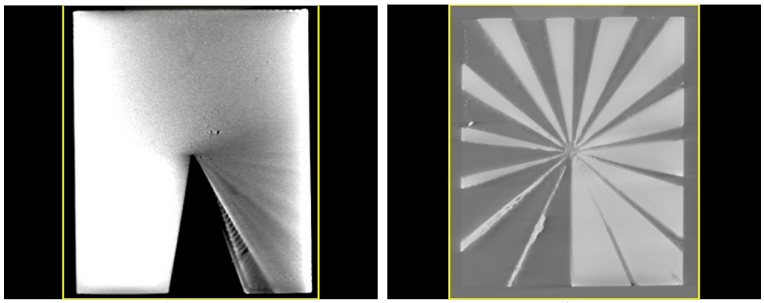


Figure 5.5: X-ray tomographs of the 3D-printed dielectric spiral phase plates (a) SPP with a stairwise structure, and (b) flat SPP with gradient refractive index.

5.3.2 Phase and amplitude analysis

Figure 5.6 shows the phase and amplitude profile generated by the 3D-printed mode 1 SPPs on the xy-plane (perpendicular to the direction of wave propagation) measured with a 5 mm step resolution over a total area of 700 mm by 700 mm.

From top to bottom are the (a-b) staircase SPP, (c-d) flat SPP and (e-f) varying thickness SPP. The printed SPPs were characterized across the frequency range 12 to 18 GHz and the phase and amplitude profiles showed qualitatively similar patterns for a specific SPP. The phase and amplitude profile at 15 GHz are shown as typical examples. The phase profile (left column in Figure 5.6) showed the expected spiral-like OAM phase profile with one spiral originating in the wave center, corresponding to OAM with mode $l = +1$. The amplitude pattern (right column in Figure 5.6) exhibited a doughnut-like beam profile with null intensity in the centre (yellow/blue in the center surrounded by red). The slight off-center position for the null region for the staircase SPP and the flat SPP likely came from slight misalignment of the transmitting and receiving horn arrangements.

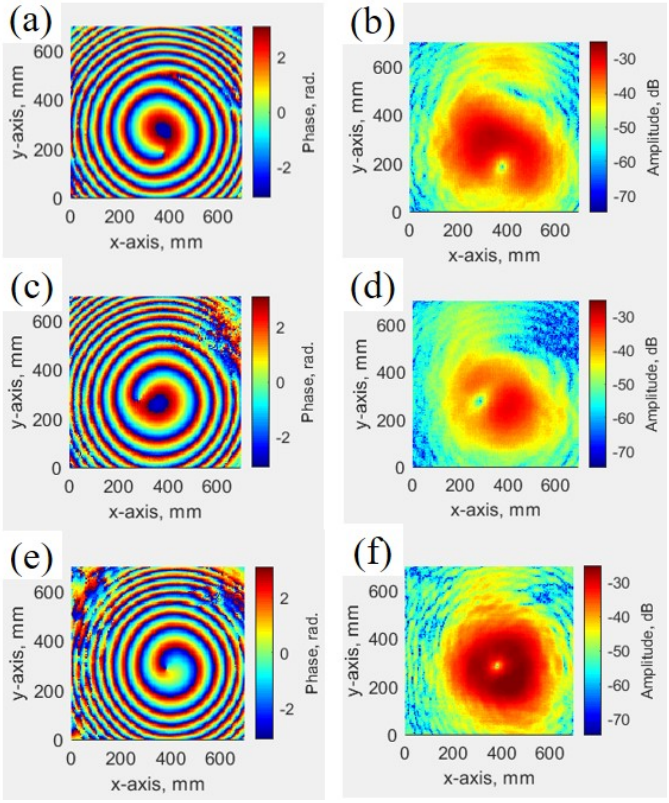


Figure 5.6: Experimental measurements from the printed SPPs with mode $l = 1$ in the xy-plane over an area of 700×700 mm^2 perpendicular to the wave propagation direction at 15 GHz: (a-b) staircase SPP phase profile and amplitude profile; (c-d) flat SPP phase profile and amplitude profile, and (e-f) varying thickness SPP phase profile and amplitude profile.

Figure 5.7 shows the amplitude and phase generated by the printed step SPP intended to produce mode 2 OAM. The phase profile shows two helical twists originating from the center that were π radians apart, which corresponded to the theoretical phase pattern of a wave with mode 2 OAM. The amplitude profile showed two null centres, which was different from the idealized amplitude pattern which has one null center, but with a much larger radius compared with mode 1 OAM. This deviation from theory might arise from inconsistencies or defects in the printing process. Interference of reflections from each staircase arrangement might also be involved,

with the staircases so close to one another (Figure 5.4(b)). In addition, differential thermal expansion of the material close to the heated platform and the material deposited at the top of the staircase profile, caused a small crack/separation of the staircases during, or immediately after, fabrication.

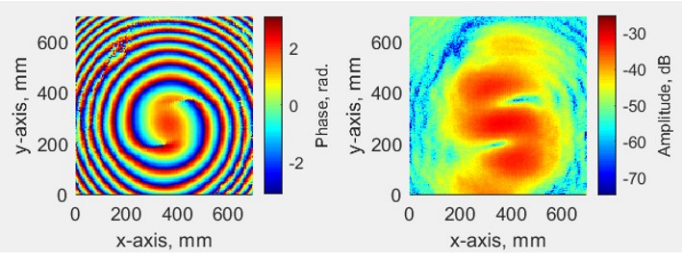


Figure 5.7: Experimental measurements from the printed staircase SPP design with mode $l = 2$, in the xy-plane cover an area of 700×700 mm^2 perpendicular to the wave propagation direction at 15 GHz: (a) phase profile, and (b) amplitude profile.

5.3.3 Reducing OAM beam divergence

Figure 5.8 shows the phase and amplitude generated from the printed staircase SPP, flat SPP, and varying thickness SPP at 15 GHz, with the addition of a printed lens placed at the exit of the transmitting horn. Compared with the phase and amplitude profiles for the same printed SPP without the lens (Figure 5.6), there was reduced diameter of the doughnut-like amplitude distribution for all SPPs, and a clearer null center. In addition, the lens improved the directivity (the desired collimation effect) of the transmitted signal and produced an additional gain of 11 dBi. Therefore, using a dielectric lens reduced the beam divergence and so may potentially increase the distance of which the wave may carry OAM.

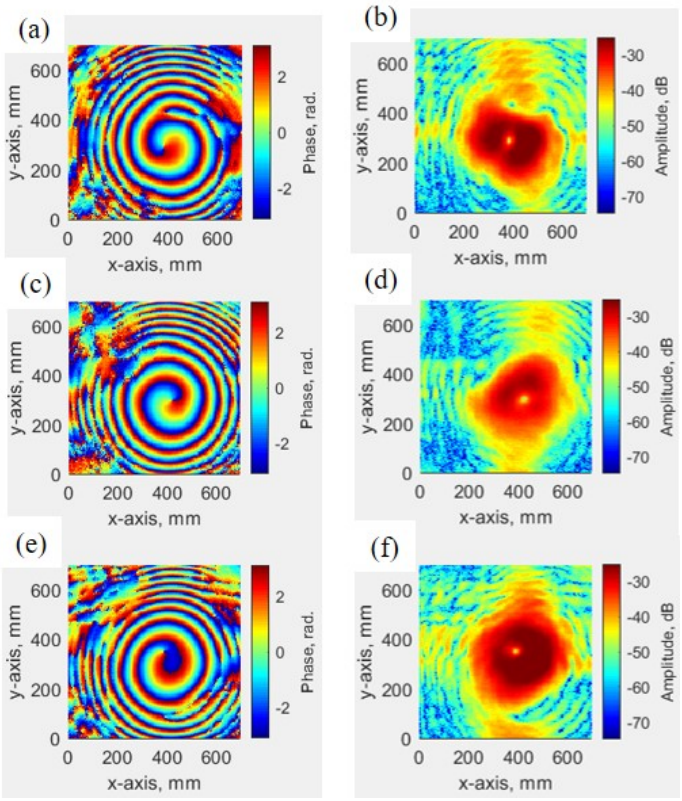


Figure 5.8: Experimental measurements from the printed SPPs with mode $l = 1$ in the xy-plane over an area of 700×700 mm^2 perpendicular to the wave propagation direction at 15 GHz with a printed lens at the transmission horn for collimation: (a-b) staircase SPP phase profile and amplitude profile; (c-d) flat SPP phase profile and amplitude profile, and (e-f) varying thickness SPP phase profile and amplitude profile.

5.3.4 Multiplexing and de-multiplexing with spiral phase plates

Mode mixing was explored with the aim to modulate $l_2 = 1 + 1$ mode or demodulate $l_0 = 1 - 1$ by mixing two OAM waves with ± 1 mode numbers as a proof-of-concept demonstration of using printed SPPs for multiplexing and de-multiplexing. The left column of Figure 5.9 shows the amplitude and phase profiles

obtained at 12 to 18 GHz from mixed signals passing through staircase SPPs for demultiplexing. Due to the phase sign change on reflection from the dielectric mirror, the two SPPs with modes $l = +1$ used in the experiment horns resulted in overall mode $l = 1 - 1 = 0$ after mixing. As conjectured, the phase profile therefore showed no helical twist, and no phase variation over the 2π radians. The amplitude profile showed a null center. The right column of Figure 5.9 shows the amplitude and phase profiles obtained at multiplexing or two SPPs with $l = 1$ and $l = -1$, which resulted in mode $l = 1 + 1 = 2$ after mixing. The phase profile showed a double helical twist which corresponded to mode $l = 2$, and the amplitude profile had a doughnut-like shape with a null center. Compared with the profiles produced by mode $l = 2$ printed staircase SPP (Figure 5.7), the wave with mode $l = 2$ OAM obtained from multiplexing of two printed SPPs showed qualitatively superior phase and amplitude profiles. This indicated the potential to spatially multiplex OAM modes using a single transmitter/receiver pair so that each mode carries an independent data stream at the transmitter and is demultiplexed at the receiver to allow for better efficiency in information transfer with minimal crosstalk.

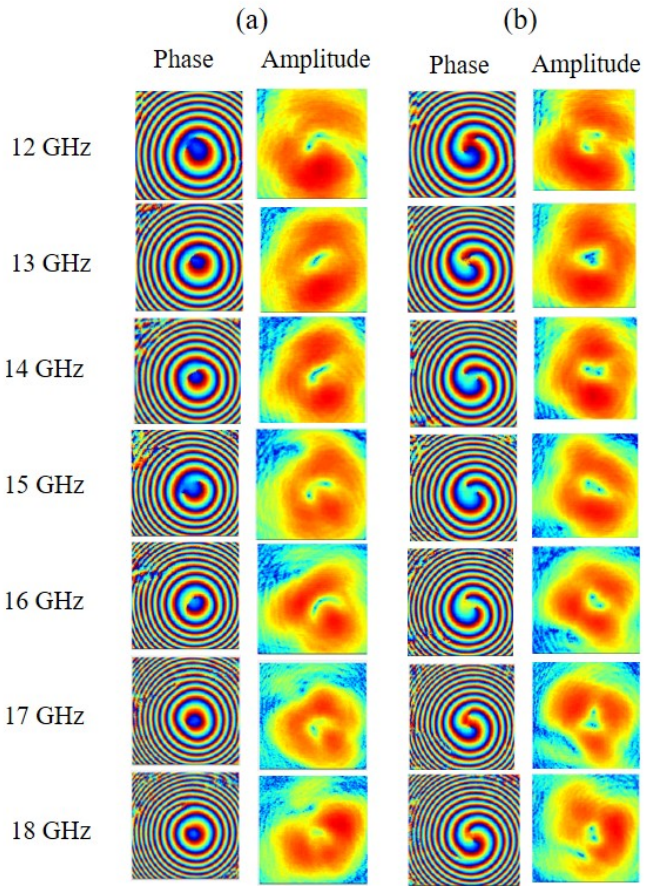


Figure 5.9: Experimental measurements of phase and amplitude profiles from the printed SPPs in the xy-plane over an area of 700×700 mm^2 perpendicular to the wave propagation direction in the frequency range 12 o 18 GHz (a) de-multiplexing with mode $l = 0$, and (b) multiplexing with mode $l = 2$.

5.4 Conclusions

Three designs of SPPs designed to induce orbital angular momentum (OAM) with mode $l = \pm 1$ and $l = \pm 2$ have been manufactured by AM utilizing single or dual material printing. All the printed SPPs showed the ability to transform a plane wave into a wave carrying OAM in the frequency range 12 to 18 GHz. The use of printed dielectric lens improved the quality of the OAM by reducing beam

divergence. The successful demonstration of printed SPPs suggested their potential application in communications systems to allow efficient use of the transmission line with OAM without energy leakage to other modes, and thus to exploit multipath propagation for multiplying the capacity of a communication link in the microwave frequency.

Bibliography

[1] D. L. Andrews, Structured light and its applications: An introduction to phase-structured beams and nanoscale optical forces, Academic Press, 2008.

[2] T. D. Drysdale, B. Allen, C. Stevensl. S. J. Berry, F. C. Smith, J. Coon, How orbital angular momentum modes are boosting the performance of radio links, IET Microw Antenn Pr. 12, 2018 1625–1632.

[3] D. Lee, H. Sasaki, H. Fukumoto, K. Hiraga, T. Nakagawa, Orbital angular momentum (OAM) multiplexing: An enabler of a new era of wireless communications, IEICE Trans. Commun. E100-B, 2017.

[4] J. Wang, J.-Y. Yang, I. M. Fazal, N. Ahmed, Y. Yan, .H Huang, Y. Ren, Y. Yue, S. Dolinar, M. Tur, and A. E. Willner, Terabit free-space data transmission employing orbital angular momentum multiplexing, Nature Photon. 6, 2012.

[5] Y. Yan, G. Xie, M. P. J. Lavery, H. Huang, N. Ahmed, C. Bao, Y. Ren, Y. Cao, L. Li, Z. Zhao, A. F. Molisch, M. Tur, M. J. Padgett, A. E. Willner, High-capacity millimetre-wave communications with orbital angular momentum multiplexing, Nature Comm. 5, 2014.

[6] W. Zhang, S. Zheng, X. Hui, R. Dong, X. Jin, H. Chi, X. Zhang, Mode division multiplexing communication using microwave orbital angular momentum: an experimental study, IEEE Trans. Wireless Comm. 16, 2017.

[7] Z. Zhang, S. Zheng, Y. Chen, X. Jin, H. Chi, and X. Zhang, The capacity gain of orbital angular momentum based multiple-input-multiple-output system, Scientific Report 6, 25418, 2016.

[8] L. Allen, M. W.Beijersbergen, R. L. C Spreeuw, J. P. Woerdman, Orbital angular momentum of light and the transformation of Laguerre–Gaussian laser modes, Phys. Rev. A 45, 1992.

[9] Q. Liu, Z. Ning Chen, Y. Liu, F. Li, Y. Chen, Z. Mo, Circular polarization and mode reconfigurable wideband orbital angular momentum patch array antenna, IEEE T. Anten. Propag. 66, 2018.

[10] Y. Zhu, D. Wei, Z. Kuang, Q. Wang, Y. Wang, X. Huang, Y. Zhang, M. Xiao, Broadband variable meta-axicons based on nano-aperture arrays in a metallic film, Scientific Report 8, 11591, 2018.

[11] J. Yang, C. Zhang, H. F. Ma, J. Zhao, J. Y. Dai, W. Yuan, L. X. Yang, Q. Cheng, and T. J. Cui, Generation of radio vortex beams with designable polarization using anisotropic frequency selective surface, Appl. Phys. Lett.,203501, 2018.

[12] K. Achouri, G. Lavigne, and C. Caloz, Comparison of two synthesis methods for birefringent metasurfaces, J. Appl. Phys. 120, 235305, 2016.

[13] T. Yuan, Y. Cheng, H. Wang, Y. Qin, and B. Fan, Radar imaging using elec-

tromagnetic wave carrying orbital angular momentum, J. Electron. Imaging, 2017.

[14] M. L. N. Chen, L. J. Jiang, and W. E. I. Sha, Ultrathin complementary metasurface for orbital angular momentum generation at microwave frequencies, IEEE T. Antenn. Prop, vol 65, no.1, 2016.

[15] P. Schemmel, G. Pisano, and B. Maffei, A modular spiral phase plate design for orbital angular momentum generation at millimetre wavelengths, Optics Express, vol.12, pp. 14712-14726, 2014.

[16] L. Cheng, W. Hong and Z. Hao, Generation of electromagnetic waves with arbitrary orbital angular momentum modes, Scientific Report 4, 4814, 2014.

[17] T. Yuan, Y. Cheng, H. Wang and Y. Qin, Generation of OAM radio beams with modified uniform circular array antenna, Electronics Letters, vol. 52, no. 11, pp. 896-898, 2016.

[18] F. Bi, Z. Ba and X. Wang, Metasurface-based broadband orbital angular momentum generator in millimeter wave region, Optics Express, vol.26, no.20, 2018.

[19] W. Y. Huang, J. L. Li, H. -Z. Wang, J. -P. Wang, and S.-S. Gao, Vortex electromagnetic waves generated by using a laddered spiral phase plate and a microstrip antenna, Electromagnetics, vol36, pp.102-110, 2016.

[20] C. A. Balanis, Antenna Theory. John Wiley & Sons, 2015.

[21] F. Castles, D. Isakov, A. Lui, Q. Lei, C. E. J. Dancer, Y. Wang, J. M. Janurudin, S. C. Speller, C. R. M. Grovenor, and P. S. Grant, Microwave dielectric charac-

terisation of 3D-printed BaTiO3/ABS polymer composites, Scientific Report 6, 22714, 2016.

Chapter 6

Active Device Tuning with Origami Structures

This chapter investigates the effect of a tunable structure based on dielectric sub-units in a flexible origami framework on the electromagnetic behaviour of a simple antenna. Two modular origami-inspired dielectric structures, fabricated by AM, are shown to shift the resonant frequency of a suspended patch antenna operating at approximately 1 GHz. FFF is used to manufacture the first flexible structure with the same composite filament of ABS-30 vol% $BaTiO_3$, used in prior chapters. The second flexible structure is composed of a polymeric lattice manufactured by sterolithography (SLA) containing dielectric elements based on a composite of ABS-60 vol% $CaTiO_3$ manufactured by field assisted sintering (FAST). Tunablity is achieved by different dielectric origami configurations that are actuated by hand or mechanically to achieve changes in the density of the dielectric origami. The dielectric origami structures provided a tunable range of at least 0.1 GHz, which is in good agreement with simulations.

6.1 Introduction

The growing number of applications requiring wireless connectivity has boosted the demand for compact wireless systems capable of multi-band operation [1, 2]. To meet the growing requirements in bandwidth but limited device space, it is beneficial for antennas to have wideband and frequency reconfigurability capabilities [3] [4]. Introducing reconfigurability to an antenna can improve the system performance (e.g. operating frequency, bandwidth and radiation pattern) and reduce the number of antennas needed [5].

Switching or tuning of antenna sub-elements is commonly used to electrically modify antenna radiation characteristics, such as pin diodes [6], varactor diodes [7], microelectromechanical switches (MEMSs) [8], or a combination [9]. However, the complexity of these approaches presents a number of drawbacks and limitations, including complexity of the system and the risk of an electrical breakdown of active components for high-power applications.

An alternative approach to accomplish reconfigurability/tunability may be by using dielectric origami (DO) structures, although this is much newer idea with few published results. At this early stage, it is difficult to assess the possible advantages and disadvantages of this approach, and this chapter presents some of the first proof of concept data. Using DO may offer new freedom for continuous frequency tuning ability, but the extent of which is unknown.

Origami structures use folding of sub-elements along pre-defined folds or creases to create geometrical change or transformation of a structure. The most common applications of origami structures are for mechanical movements. For example, a twisted tower inspired by origami structures has been fabricated using a flexible ma-

terial for the creases or hinges and a rigid material for the elements to demonstrate the ability to grip objects robustly [10]. The same concept can be applied in antenna manipulation, such as an early example simply using creased paper to create a foldable origami spring structure to change the operating frequency of an antenna [11]. However, those origami structures lack accurate and robust control over the configuration states.

To provide robust re-reconfigurability, and without binding or additional connecting elements, 3D printed origami structures have started to emerge. Fused filament fabrication (FFF) has been used to create a cross-shaped structure from VeroWhite plastic filament ($\epsilon_r < 4$) that folded into a cuboid, with small metallic patch antennas then printed directly on the cube surface [19]. In another example, a novel photocurable elastomer system has been developed and 3D printed to make origami assemblages with smooth hinges [20]. SLA has been used to print a bow-tie antenna, inspired by an origami fan, with an elastic resin ($\epsilon_r = 2.7$) before the whole structure was metallized to facilitate folding [21]. All these 3D printed origami structures showed a tuning range of less than 15%, and no demonstration of mechanical or other actuation was described.

In this chapter, the application of extensible DO made of high permittivity dielectric sub-units is used to realize a frequency tunable patch antenna. The approach is based on inserting a printed DO layer in the air gap of a suspended patch antenna and then changing the configuration of the DO to effect a change in the effective permittivity of the medium, thus causing the resonant frequency of the antenna to shift. The extent of the resonant frequency shift, corresponding to the tuning range of the antenna, is determined by the variation of the geometric configuration of the DO from a fully compressed/dense configuration (all the faces of the elements touching

each other) to a fully open configuration (elements only touching at their edges).

6.2 Methods

Two modular origami-inspired dielectric structures were fabricated by different AM methods. The first DO consisted of a collection of right-angled triangles fabricated by FFF (Makerbot Replicator) using the previously described filament comprising 32 vol% $BaTiO_3$ micro-powders dispersed in ABS ($\epsilon_r \sim 11$). The unit cell was composed of 4 right-angled triangles with a side length of 8.5 mm and thickness of 7 mm, connected through tape, shown in red in Figure 6.1(a). When a force was applied in the y direction, the unit cell transformed its configurations, e.g. 1 to 2 and then to 3. The DO assembly was 97 mm by 77 mm when fully closed or compressed (maximum density state), as shown in Figure 6.1 (b). As the DO expanded to 6.1 (c), the corresponding effective permittivity can be expected to decrease due to the progressive introduction of a greater volume fraction of air into the assembly.

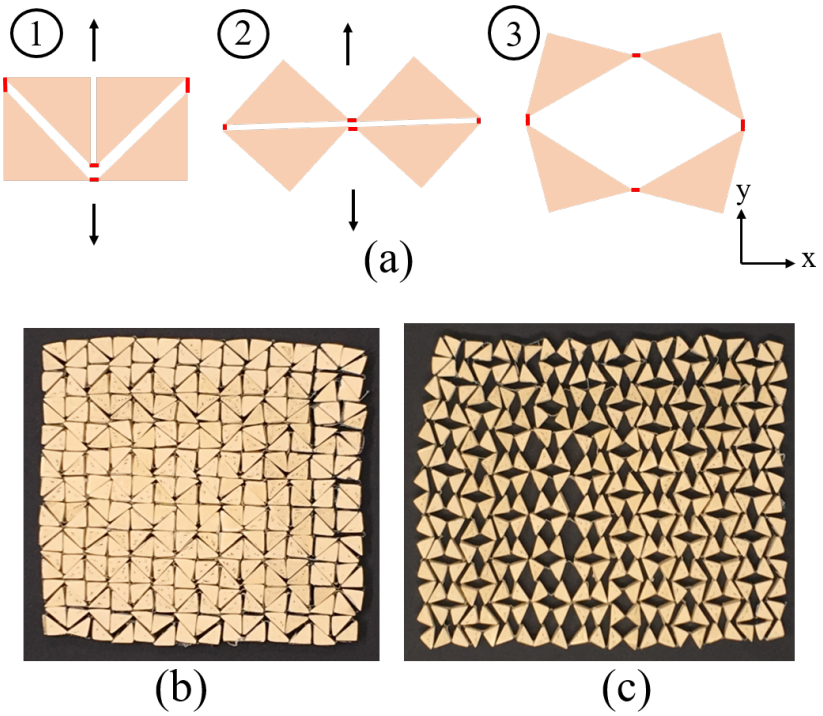


Figure 6.1: (a) The transformation of an origami unit cell from configuration 1 to 2 and 3, with arrows showing the direction of the applied force along y axis; (b) printed $BaTiO_3$/ABS DO in the fully compressed state, and (c) in the expanded state.

The second DO consisted of a flexible lattice-like structure printed with an elastic resin using a SLA printer (Formlabs 2) with high dielectric composite triangles then inserted, which comprised 60 vol% $CaTiO_3$ micro-scale powers dispersed in ABS. The flexible lattice had a wall thickness of 0.8 mm, and overall area of 106 mm by 114 mm with thickness of 1 mm, as shown in Figure 6.2 (a). The dielectric triangle elements shown in 6.2(b) had a thickness of 6.2 mm and a measured permittivity $\epsilon_r \sim 15.6$ and loss of $\tan\delta \sim 0.0113$ obtained by a split-post dielectric resonator (SPDR) measurement at 15 GHz. The dielectric elements were manufactured by dispersing $CaTiO_3$ and ABS in acetone solution until the ABS was fully dissolved. The solution was then dried and mechanically milled into small pieces using a blade

mixer. The fragments were then consolidated into a dense disc using field assisted sintering technique (FAST) (Dr Fritsch) at 120°C and 15 MPa. The consolidated disc had a diameter of 80 mm and thickness 6.2 mm, as shown in Figure 6.3(a). In the FAST process, electric current was passed through a graphite die that contained the $CaTiO_3$/ABS feedstock to provide heating, and while a uniaxial pressure was exerted. The triangular dielectric elements were then obtained by sectioning the composite disc using a waterjet cutter to obtain two sizes of right-angle triangles: one with a short-side length of 8 mm as shown in Figure 6.3 (b) and another with a short side length of 13.5 mm. Afterwards, the DO was assembled by fitting the triangles into the printed flexible lattice, as shown in Figure 6.4.

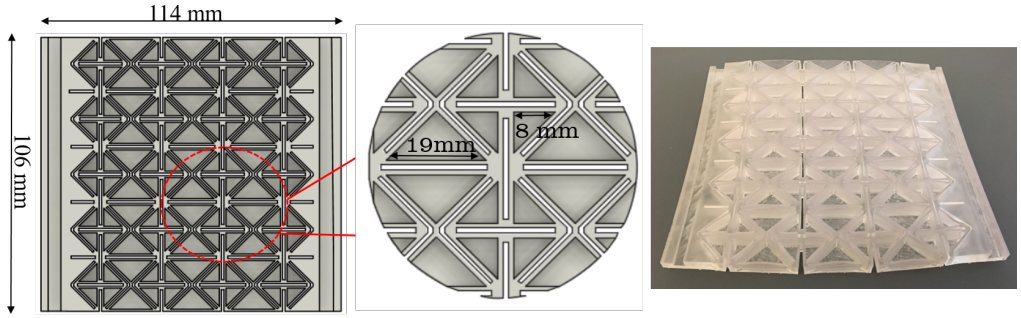


Figure 6.2: (a) CAD design of the SLA printed flexible lattice for DO with a groove on the left an right sides for fixation; (b) higher magnification view of the unit cells of triangle structures within the flexible lattice, and (c) a photograph of the printed flexible lattice.

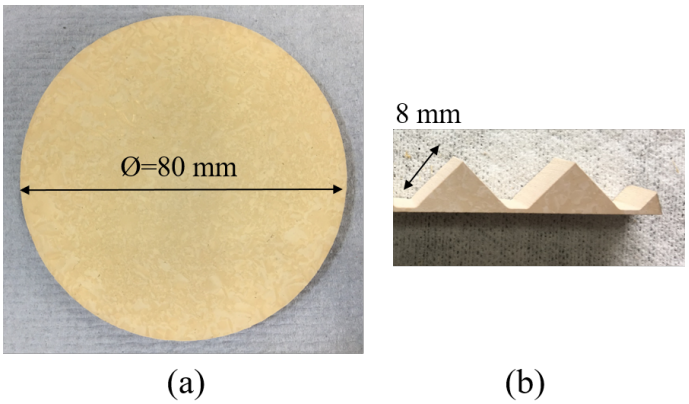


Figure 6.3: (a) Disc of $CaTiO_3$/ABS composite (diameter of 80 mm) produced by the field assisted sintering technique, and (b) triangular dielectric elements of short side length 8 mm obtained by waterjet cutting.

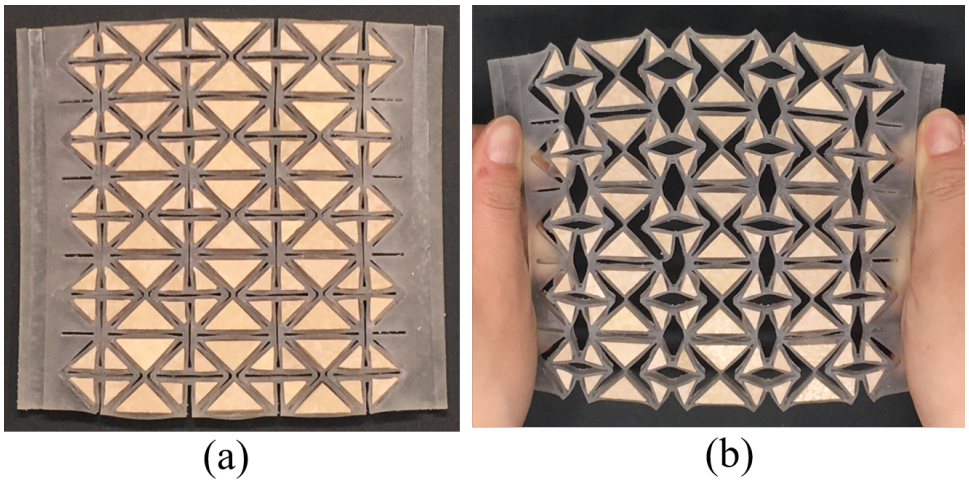


Figure 6.4: The ABS-60 vol% $CaTiO_3$ DO (a) fully compressed, and (b) expanded by hand.

The resonant frequency f for a square suspended patch antenna shown schematically in Figure 6.5, is given by:

$$f = \frac{c}{2L_{eff}\sqrt{\epsilon_{r,eff}}} \tag{6.1}$$

where c is the speed of light, $\epsilon_{r,eff}$ is the effective permittivity of the media in the gap of the antenna, and $L_{eff} = L + 2\Delta L$ is the effective length of the patch because of the fringing effects is larger than its physical dimension L by a distance of ΔL.

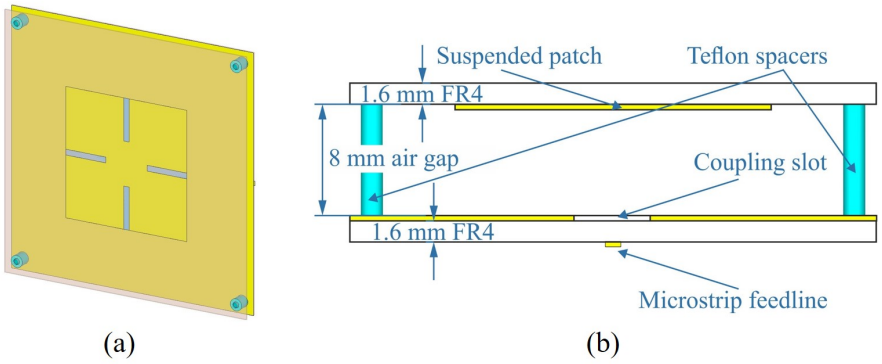


Figure 6.5: (a) Schematic and (b) cross-sectional view of the suspended patch antenna with an 8 mm air gap between the ground plane and the patch, into which the DO may be placed.

The antenna in Figure 6.5 (generated by Dr. Vallecchi, Department of Engineering Science, University of Oxford) has a side length $L = 90$ mm, and the dielectric substrate is 180 mm by 180 mm. A rectangular slot was cut at the centre of the ground plane to couple the patch to the microstrip feed line running on the opposite side of the bottom FR4 substrate. Insertion of the DO or any new material other than air into the gap of the antenna will modify $\epsilon_{r,eff}$, and will thus change the resonant frequency of the patch according to Equation 6.1. Further, frequency tunability can be achieved by actuating the DO into different configurations and different effective volume averaged mixtures of high (elements) and low (air) permittivity materials.

Although Equation 6.1 provides a convenient way to assess the effect of changes in $\epsilon_{r,eff}$ on antenna resonance, electromagnetic simulation software allows more sophisticated assessment of the changes in arrangement on patch performance, including capturing the specifics of the geometries under consideration. CST Microwave

Studio was used by Dr. Vallecchi to simulate the resonant frequency of the suspended patch antenna as a function of DO permittivity, as shown in Figure 6.6. As expected, there was an inverse relationship between the resonant frequency and DO permittivity, as indicated by Equation 6.1.

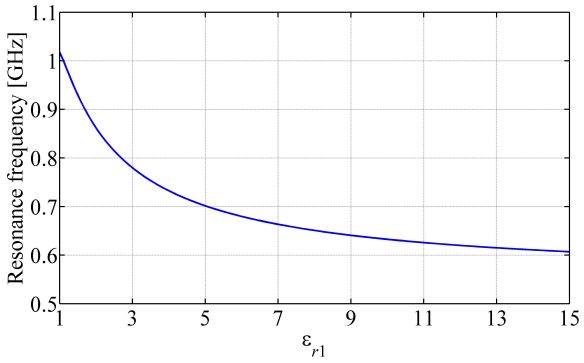


Figure 6.6: Resonant frequency of a suspended patch in Figure 6.5 when a dielectric layer of variable permittivity and thickness of 7 mm is inserted into the air gap, as calculated by Dr. Vallecchi using the approach described in [24].

To allow for a more repeatable and controllable transformation of the DO than that available by hand, a micro-linear mechanical actuation rig was designed and built, as shown in Figure 6.7. Two fixtures were 3D printed using Onyx filament (MarkForged) to attach to the left and right side of the flexible lattice using the grooves printed into the lattice for this purpose; the left side was fixed to a supporting board, and the right side was connected to the linear actuator (Actuonix L16). A controller box was used to control the movement of the linear actuator. The linear actuator was in its fully extended state when the DO was fully closed (maximum density state), and the DO then expanded as the actuator retracted. A ruler was used to measure the extension.

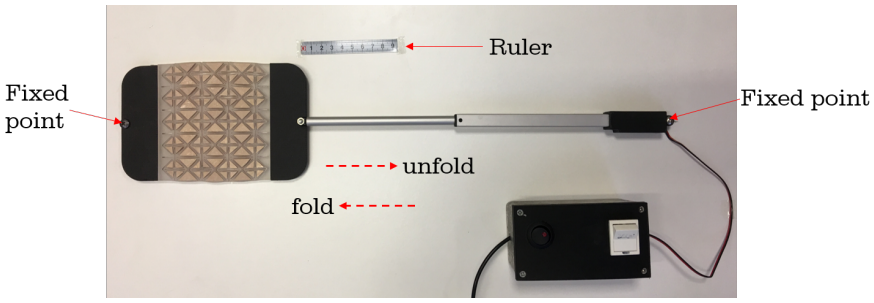


Figure 6.7: Mechanical actuation arrangement for the DO. Printed Onyx fixtures are shown in black.

The dielectric composite materials used for the two DOs were analysed using scanning electron microscopy (SEM, JEOL 6500) to study the micro-particle distribution within the polymer matrix. A vector network analyzer (VNA) E5061B (Keysight) was used to energize microwaves into the patch antenna and to measure the reflection coefficient S_{11} from the antenna at its input port.

6.3 Results and Discussion

6.3.1 Materials characterization

The material for the first DO with printed $BaTiO_3$/ABS (Figure6.8(a)) has already been characterized and discussed in Chapter 3. To explore the effect of higher ceramic loadings than those available from the printable filaments, FAST was used to manufacture composite dielectric elements with 60 vol% $CaTiO_3$ dispersed in ABS. Figure 6.8(b) shows $CaTiO_3$ particles embedded within the ABS matrix, and some small pores on the order of 1 μm. Although not reported further in this thesis, other high permittivity ceramic particulates (e.g. $BaTiO_3$ and $BaSrTiO_4$) were also used to make 60 vol% loading ABS-based composites, showing the versatility of this

approach, with their permittivity measured using SPDR at 15 GHz, shown in Table 6.1. $BaTiO_3$/ABS composite had the highest permittivity of $\sim$ 18. $CaTiO_3$/ABS was chosen for the DO due to its relatively low loss.

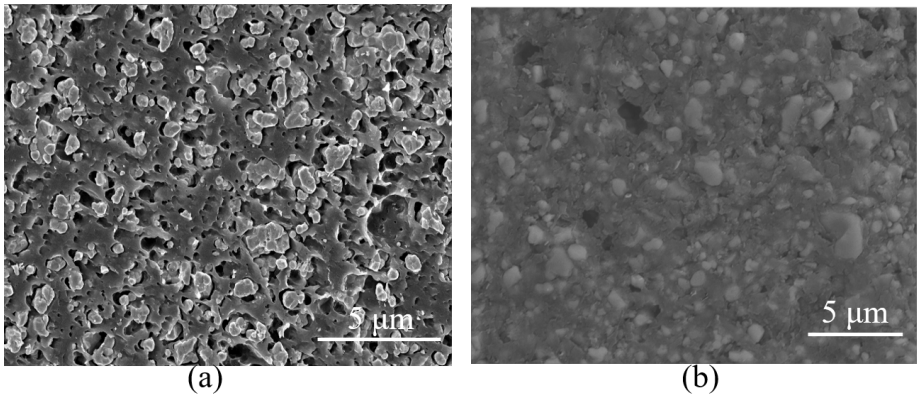


Figure 6.8: SEM images of (a) 32 vol% $BaTiO_3$ dispersed within ABS in filament form for FFF, and (b) 60 vol% $CaTiO_3$ dispersed within ABS in circular coupon form after production using FAST.

Material	ϵ_r	loss
$BaTiO_3$	18	0.0579
$CaTiO_3$	15.6	0.0113
$BaSrTiO_4$	15.6	0.0201

Table 6.1: Permittivity and loss for ABS-60 vol% ceramic composites prepared by FAST.

6.3.2 $BaTiO_3$/ABS dielectric origami

As shown in Figure 6.9, on introducing the fully dense DO into the air-gap between the suspended patch antenna and the ground plane, the resonant frequency shifted from 1 GHz to 0.736 GHz. Then by changing (actuating) the DO configu-

ration from fully dense to half dense, the effective permittivity was lowered and the resonant frequency changed to 0.791 GHz. Overall, there was a maximum tunable range of 0.055 GHz. In this arrangement, there was also a reduction in the S_{11} intensity when the DO was inserted. This arose from a larger impedance mismatch between the antenna and DO. The mismatch of the reflection coefficient was due to the discrepancy in the permittivity value of the DO compared with air. The inconsistency between the simulation results, also shown in Figure 6.9, and the experimental results might arise from the manual actuation of the DO and manufacturing inconsistencies, in part due to the final assembly by hand. For example, stretching of the hinges connecting the elements resulted in some reduction of the effective permittivity of the DO even when in the supposedly fully dense configuration. These effects could be reduced by printing more reproducible and consistent flexible hinges that might deform more reliably during transformation, and by improving the surface finish of the DO to account for the air gaps between each unit cell.

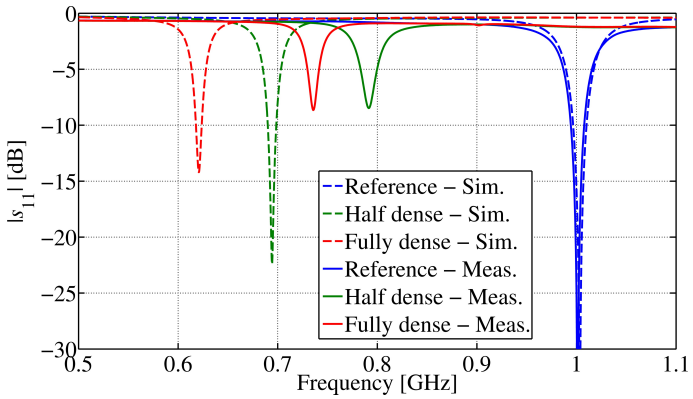


Figure 6.9: Modulus of the reflection coefficient S_{11} from a suspended patch antenna resonating at 1 GHz and with two configurations of DO placed below the antenna over a Cu ground plane. Dotted lines represent simulations and solid lines experiment.

6.3.3 $CaTiO_3$/ABS dielectric origami

The second DO comprised $CaTiO_3$/ABS composite and a flexible lattice that was actuated mechanically. Taking advantage of the precision and repeatability from the mechanical actuation, several measurements of the antenna reflection coefficient against linear extension distance were recorded, up to a linear extension of 50 mm. As the DO structure was extended to various distances, a greater air fraction was introduced into the structure, as shown in Figure 6.4(b). There was a larger resonant frequency shift of ~ 0.315 GHz for the fully closed ABS-60vol% $CaTiO_3$ DO due to its higher overall permittivity (despite the use of the flexible lattice with relatively low permittivity $\epsilon_r \simeq 3$). Correspondingly, the tuning range increased to 0.105 GHz, shown in Figure 6.10. An estimation of the effective permittivity of the DO can be obtained by interpolating the plot of the resonant frequency of the patch against the permittivity of a 7-mm-thick dielectric layer inserted into the original air gap of the antenna (Figure 6.6) calculated by using the theoretical expressions in Equation 6.1. The effective permittivity data are included in Figure 6.10 and shows that, as expected, the effective permittivity of the DO progressively decreased as the structure was opened.

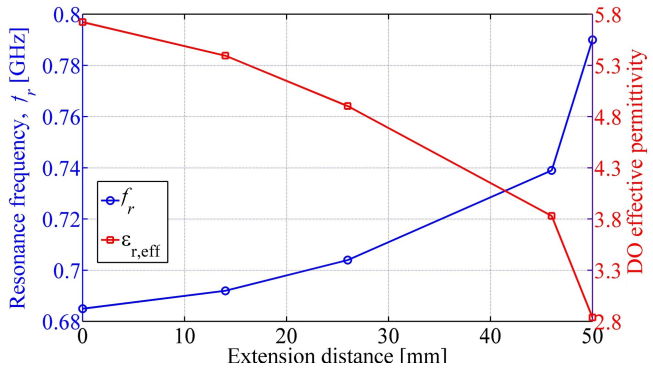


Figure 6.10: Measured resonant frequency of a patch antenna against the extension distance (opening) of the ABS-60vol% $CaTiO_3$ DO (blue circles) and the corresponding estimated effective permittivity of the DO (red diamonds) from simulation in Figure 6.6.

As the continuous mechanical deformation of the DO on extension is difficult to measure accurately, the effective permittivity could only be estimated in the closed/fully compressed configuration and when fully "open". The effective permittivity of the ABS-60vol% $CaTiO_3$ DO in the fully compressed state can also be estimated using Maxwell Garnett (MG) equation because the small air gaps in between the flexible lattice and the dielectric composite assumed negligible [25], and is given by:

$$\epsilon_{eff} = \epsilon_h \frac{\epsilon_i(1+2f) + 2\epsilon_h(1-f)}{\epsilon_i(1-f) + \epsilon_h(2+f)} \tag{6.2}$$

where ϵ_{eff} is the effective permittivity, ϵ_h is the permittivity of the flexible lattice, ϵ_i is the permittivity of the dielectric composite inclusions, and f is the fill fraction of the composite. f was estimated as 37% based on the volume fraction of triangles. The resulting effective permittivity is calculated as 5.5 for the fully compressed state, which corresponds well with the estimated value of $\sim$ 5.6 from Figure 6.6.

In the expanded state (50 mm expansion), MG Equation for two different types of inclusions is needed because air was considered as an inclusion in the expanded state, and is given by:

$$\epsilon_{eff} = \epsilon_h[1 + \frac{3(f_1\frac{\epsilon_1-\epsilon_h}{\epsilon_1+2\epsilon_h} + f_2\frac{\epsilon_2-\epsilon_h}{\epsilon_2+2\epsilon_h})}{1 - f_1\frac{\epsilon_1-\epsilon_h}{\epsilon_1+2\epsilon_h} - f_2\frac{\epsilon_2-\epsilon_h}{\epsilon_2+2\epsilon_h}}] \tag{6.3}$$

where ϵ_1 is the permittivity for the dielectric composite, ϵ_2 is the permittivity for air, and f_1, f_2 are the corresponding fill fraction for the composite and air. f_1 and f_2 were estimated to be 19.03% and 43.4%. The resulting permittivity was calculated as 2.9 for the expanded state, again corresponded well with the estimated value of 2.8 from Figure 6.6.

6.4 Conclusions

Two dielectric origami structures were fabricated by FFF/hand assembly and FAST/SLA. Transformation of the origami was realized through manual placement or mechanical actuation. A tuning range of up to 0.1 GHz was demonstrated for a 1 GHz resonating patch antenna that was in good agreement with simulation results. Further to this early demonstration, avenues for achieving broader range of tunablity using dielectric origami structures can be readily explored using numerical simulations and the various manufacturing approaches explored here.

Bibliography

[1] N. Cohen, Fractal antenna applications in wireless communications, Electronic Industries Forum of New England, pp.43-49, 1997.

[2] C. Pan, T. Horng, W. Chen and C. Huang, Dual wideband printed monopole antenna for WLAN/WiMAX applications, IEEE Antennas and Wireless Propagations Letters, vol.6, pp.149-151, 2007.

[3] J. Liang, C. Chiau, X. Chen and C. Parini, Printed circular disc monopole antenna for ultra-wideband applications, Electronics Letters, vol.40, pp.6-7, 2004.

[4] C. Christodoulou, Y. Tawk, S. Lane and S. Erwin, Reconfigurable antennas for wireless and space applications, Proceedings of the IEEE, vol.100, pp. 2250-2261, 2012.

[5] R. Bahr, B. Tehrani, J. Hester, J. Kimionis and M. Tentzeris, Additive manufacturing techniques for origami inspired 4D printed RF components and modules, IEEE MTT-S International Microwave Workshop Series on Advanced Materials and Processes for RF and THz Applications (IMWS-AMP), 2016.

[6] A. Mansoul, F. Ghanem, M. Hamid and M. Trebelsi, A selective frequency-reconfigurable antenna for cognitive radio applications, IEEE Antennas and Wireless Propagation Letters, vol.13, pp.515-518, 2014.

[7] N. Behdad and K. Sarabandi, Dual-band reconfigurable antenna with a very wide tunability range, IEEE Transactions on Antennas and Propagation, vol.54, pp.409-416, 2006.

[8] J. Kovitz, H. Rajagopalan and Y. Rahmat-Samii, Design and implementation of broadband mems rhcp/lhcp reconfigurable arrays using rotated e-shaped patch elements, IEEE Transactions on Antennas and Propagation, vol.63, pp.2497-2507, 2015.

[9] H. Li, J. Xiong, Y. Yu and S. He, A simple compact reconfigurable slot antenna with very wide tuning range, IEEE Transactions on Antennas and Propagation, vol.58, pp.3725-3728, 2010.

[10] T. Liu, Y. Wang and K. Lee, Three-dimensional printable origami twisted tower: design, fabrication, and robot embodiment, IEEE Robotics and Automation Letters, vol.3, pp.116-123, 2018.

[11] S. Yao, X. Liu, S. Georgakopoulos and M. Tentzeris, A novel reconfigurable origami spring antenna, IEEE Antennas and Propagation Society (AP-S), pp.374-375, 2014.

[12] K. Wong and A. Hernandez, A review of additive manufacturing, ISRN Mechanical Engineering, 2012.

[13] D. Espalin, J. Ramirez, F. Medina, W. Johnson, M. Rowell, B. Deason, M. Eubanks, B. Turner, R. Strong and S. Gold, A review of melt extrusion additive manufacturing processes: I. Process design and modelling, Rapid Prototyping Journal, vol.20, pp.192-204, 2014.

[14] S. Kumar, M. Hofmann, B. Steinmann, E. Foster and C. Weder, Reinforcement of stereolithographic resins for rapid prototyping with cellulose nanocrystals, ACS Applied Materials and Interfaces, 2012.

[15] J. Lewis, Direct ink writing of 3D functional materials, Advanced Functional Materials, vol.16, pp.2193-2204, 2006.

[16] C. Yap, C. Chua, Z. Dong, Z. Liu, D. Zhang and L. Loh, Review of selective laser melting: materials and applications, Applied Physics Reviews, 2016.

[17] P. Pa, Z. Larimore, P. Parsons and M. Mirotznik, Multi-material additive manufacturing of embedded low-profile antennas, Electronics Letters, vol.51, pp.1561-1562, 2015.

[18] M. Liang, C. Shemelya, E. Macdonald, R. Wicker and H. Xin, 3-D printed microwave patch antenna via fused deposition method and ultrasonic wire mesh embedding technique, IEEE Antennas and Wireless Propagation Letters, vol.14, pp.1346-1349, 2015.

[19] J. Kimionis, A. Georgiadis, M. Isakov, H. Qi and M. Tentzeris, 3D/inkjet-printed origami antennas for multi-direction RF harvesting, IEEE International Microwave Symposium, 2015.

[20] Z. Zhao, X. Kuang, J. Wu, Q. Zhang, G. Paulino, H. Qi and D. Fang, 3D printing of complex origami assemblages for reconfigurable structures, Soft Matter, vol.14, pp.8051-8059, 2018.

[21] W. Su, R. Bahr, S. Nauroze and M. Tentzeris, Novel 3-D printed bow-tie antennas for origami/shape-changing configurations, Proceedings of IEEE Antennas and Propagation Society International Symposium, 2017.

[22] C. Balanis, Antenna theory: analysis and design, Ebook Central, fourth edition, 2016.

[23] A. Sihvola, Mixing rules with complex dielectric coefficients, Surface Sensing Technologies and Applications, vol.1, pp 393-415, 2000.

[24] M. Biswas and M. Sen, Design and development of rectangular patch antenna with superstrates for the application in portable wireless equipments and aircraft

radome, Microwave and Optical Technology Letters, vol. 56, no. 4, pp. 883–893, 2014.

[25] J. C. M. Garnett, Colours in metal glasses and in metallic films, Philosophical Transactions of the Royal Society London A, vol. 203, pp. 385–420, 1904.

Chapter 7

Conclusions

This thesis has focused on the materials optimization and manufacturing methods for fabrication and realization of manipulation of EM waves in the microwave frequency range 12 to 18 GHz for simple devices (e.g. quarter wave plate and spiral phase plate) by changing the local relative permittivity within the device.

An optimized dielectric composite filament composed of 32 vol% of $BaTiO_3$ dispersed in ABS matrix has been developed with 1 wt% of surfactant (octyl gallate) and 5 wt% of plastciser (dibutyl phthalate). The optimized filament had a dielectric permittivity of ~ 11 and a loss of 3×10^{-2} and was able to be printed successfully into a range of devices because of its relatively uniform microstructure and minimization of defects.

A quarter wave plate was manufactured by printing ABS filament with low dielectric permittivity ($\epsilon_r = 2.6$) and optimized composite filament of high dielectric permittivity ($\epsilon_r = 10.8$) in alternating stripes. The printed QWP demonstrated the ability to change the polarization of an EM wave from linear polarization to circular polarization and vice versa, consistent with simulations. In addition to the designed

frequency of 15 GHz, the printed dielectric QWP showed conversion of polarization at 13.1 GHz, 14.4 GHz, and 16.35 GHz, which indicated the potential for a broadband device.

Spiral phase plates with different mode numbers (l) were designed and printed. The phase gradient was achieved through changing either the thickness of the SPP (increase in thickness in a spiral pattern) or the refractive index of the SPP (a flat SPP with locally varying permittivity by mixing two filaments locally with sub-wavelength resolution through varying their fill fraction). The printed SPPs showed the ability to change an incoming plane EM wave into a helical wave carrying OAM. The flexibility of AM was also used to print higher mode SPPs. A proof of concept demonstration of multiplexing and demultiplexing was performed using SPPs with mode +1 and -1. The successful demonstration indicated the possibility to exploit multipath propagation using printed SPPs for multiplying the capacity of radio links.

Lastly, active device tuning was explored. Inspired by structural flexibility of origami structures, two dielectric origami structures were printed for tuning of a suspended patch antenna with a resonant frequency at 1 GHz. The printed origami structures were actuated manually or through mechanical actuation to realize different configurations. A combination of AM method (e.g. SLA) and a powder processing method (FAST) was used to fabricate a dielectric origami structure of higher dielectric permittivity up to 18. A tuning range of ~ 0.1 GHz was achieved for a origami structure that comprised ABS-60 vol% $CaTiO_3$ unit cells, manufactured from FAST, embedded in a SLA printed flexible polymer lattice. This early demonstration of using origami structures for active device tuning may open up new research directions for creating broadband devices for operation in the microwave frequency band.

Chapter 8

Future Work

AM provides a promising avenue of investigation for the printing of devices with locally varying permittivity. By changing the relative fractions of functional filler with high permittivity in a lower permittivity flexible filament, or by mixing high and low permittivities at deposition in a two filament system, a range of local permittivities can be achieved. Various applications and devices (such as antennas, waveguides, and beam splitters) operating at GHz frequencies have been printed.

Increasing the filament dielectric permittivity for FFF through new composites would facilitates device size reduction because the optical path lengths relate to the difference in refractive index between materials multiplied by the sample thickness. Using surfactant and plasticiser optimization might further enhance dielectric and mechanical properties. The same method might also be extended to the development of conductive filament or magnetic filament to explore the potential to use other functionality to realize the control of EM wave propagation. The versatility of mixing materials by multi-material AM may open up the possibility of realising devices with a wider variety of functionalities.

This thesis has shown the successful use of tuning using dielectric origami, especially by using a flexible lattice embedded with high dielectric elements. There is no reason in principle why these elements might be entirely ceramic, with a correspondingly much higher permittivity, and thus tuning capability. That said, the use of composite based in FAST processing made them easy to fabricate and very fast to machine into elements.

To further explore active device control or 4D printing. Other methods for actuation (e.g. heat, light, magnetism, etc.) can be explored as a means to actuate the device for a forth dimension of freedom. For example, printed heating elements can be integrated into a structure containing materials with a strongly varying permittivity with temperature. By actuating the heaters to phase transition temperature with external heating source applied at different locations, the local permittivity can be modified theoretically and a thermally active or tunable device can be conceived. This research area will take full advantage of AM and may spark novel applications with broadband features, compact designs, and make devices capable of multi-functionalities.

List of Publications

1. Y Wu, D Isakov and PS Grant, Fabrication of composite filament with high dielectric permittivity for fused 3D printing, Materials 10(10), 2017.

2. Y Wu, PS Grant and D Isakov, 3D-printed $\lambda/4$ phase plate for broadband microwave applications, Optics Express 26(22), 2018.

3. Y Wu, A Vallecchi, Y Yang, Z You, C Stevens, E Shamonina, PS Grant, 3D printed modular origami inspired dielectrics for frequency tunable antennas, 2019 IEEE International Symposium on Antennas and Propagation.

4. B Allen, T Pelham, Y Wu, T Drysdale, D Isakov, C Gamlath, CJ Stevens, G Hilton, MA Beach, and PS Grant, Experimental evaluation of 3D printed spiral phase plates for enabling an orbital angular momentum multiplexed radio system, Royal Society Open Science 6(12), 2019.

5. L Fieber, SS Bukhari, Y Wu and PS Grant, In-line measurement of the dielectric permittivity of materials using additive manufacturing and 3D data reconstruction, Additive Manufacturing 101010, 2019.

6. D Isakov, Y Wu, B Allen, PS Grant, CJ Stevens and GJ Gibbons, Evaluation of the Lagurrer-Gaussian mode purity produced by three-dimensional-printed

microwave spiral phase plates, Royal Society Open Science 7(7), 2020.